

Water Transport in Complex, Non-Wetting Porous Layers with
Applications to Water Management in Low Temperature Fuel Cells

By

Ezequiel F. Médici

A DISSERTATION

Submitted in partial fulfillment of the requirements for the degree of

DOCTOR OF PHILOSOPHY

(Mechanical Engineering – Engineering Mechanics)

MICHIGAN TECHNOLOGICAL UNIVERSITY

2010

Copyright © 2010 Ezequiel F. Médici

This dissertation, “Water Transport in Complex, Non-Wetting Porous Layers with Applications to Water Management in Low Temperature Fuel Cells ,” is hereby approved in partial fulfillment for the requirements for the Degree of DOCTOR OF PHILOSOPHY IN Mechanical Engineering – Engineering Mechanics.

Department of Mechanical Engineering – Engineering Mechanics

Advisor: _____
Dr. Jeffrey S. Allen

Committee Member: _____
Dr. Amitabh Narain

Committee Member: _____
Dr. Abhijit Mukherjee

Committee Member: _____
Dr. Jason M. Keith

Department Chair: _____
Professor William W. Predebon

Date: _____

To my parents, Alberto F. Médici and María Laura Lazcano de Médici.

ABSTRACT

Water Transport in Complex, Non-Wetting Porous Layers with Applications to Water Management in Low Temperature Fuel Cells

Ezequiel F. Médici

Michigan Technological University, 2010

Advisor: Dr. Jeffrey S. Allen

An experimental setup was designed to visualize water percolation inside the porous transport layer, PTL, of proton exchange membrane, PEM, fuel cells and identify the relevant characterization parameters. In parallel with the observation of the water movement, the injection pressure (pressure required to transport water through the PTL) was measured. A new scaling for the drainage in porous media has been proposed based on the ratio between the input and the dissipated energies during percolation. A proportional dependency was obtained between the energy ratio and a non-dimensional time and this relationship is not dependent on the flow regime; stable displacement or capillary fingering. Experimental results show that for different PTL samples (from different manufacturers) the proportionality is different. The identification of this proportionality allows a unique characterization of PTLs

with respect to water transport. This scaling has relevance in porous media flows ranging far beyond fuel cells.

In parallel with the experimental analysis, a two-dimensional numerical model was developed in order to simulate the phenomena observed in the experiments. The stochastic nature of the pore size distribution, the role of the PTL wettability and morphology properties on the water transport were analyzed. The effect of a second porous layer placed between the porous transport layer and the catalyst layer called microporous layer, MPL, was also studied. It was found that the presence of the MPL significantly reduced the water content on the PTL by enhancing fingering formation. Moreover, the presence of small defects (cracks) within the MPL was shown to enhance water management.

Finally, a corroboration of the numerical simulation was carried out. A three-dimensional version of the network model was developed mimicking the experimental conditions. The morphology and wettability of the PTL are tuned to the experiment data by using the new energy scaling of drainage in porous media. Once the fit between numerical and experimental data is obtained, the computational PTL structure can be used in different types of simulations where the conditions are representative of the fuel cell operating conditions.

ACKNOWLEDGMENTS

I take this opportunity to express my gratitude to Dr. Jeffrey Allen for his advice and support since my first day at Michigan Technological University and for his invaluable and inspiring technical guidance along these years.

I would like to thank the unconditional professional support of my research group partners: Alexandru Herescu, Joseph Hernandez, and Russel Stacy. I would like to give special thanks to Stephen Stacy for his assistance with the experiments.

I am grateful for all the economical support received during my Ph.D studies. This work was partially funded by DOE contract DE-EE-0000466 in collaboration with Ballard Power Systems, DOE contract DE-FG36-07GO17018 in collaboration with the Rochester Institute of Technology and General Motors, the Department of Mechanical Engineering – Engineering Mechanics, and the Michigan Technological University Graduate School for the finishing fellowship.

I am also deeply grateful of having been the first recipient of the Bhakta Rath research award at Michigan Technological University.

I would like to express my sincere thanks Kateryna Lapina, Julio Rivera, Lucas and Marisa Lago, Eino Neimi, and many others for their precious timeless friendships.

CONTENTS

<i>Abstract</i>	vii
<i>Acknowledgments</i>	ix
<i>List of Figures</i>	xvii
<i>List of Tables</i>	xix
<i>Nomenclature</i>	1
1. <i>Introduction</i>	3
1.1 Motivation	3
1.2 Outline	8
2. <i>Existence of the Phase Drainage Diagram in PEM Fuel Cell Fibrous Diffusion Media</i>	13
2.1 Introduction	14
2.2 Experimental Setup	18
2.2.1 Image Post-Processing	21
2.3 Observations	22
2.3.1 Stable displacement	22
2.3.2 Capillary Fingering	26
2.3.3 Viscous Fingering	31
2.4 Discussion	36
2.4.1 Drainage flow regimes in DMs	37
2.5 Conclusions	38
3. <i>Scaling the Water Percolation in PEM Fuel Cell Porous Transport Layers</i>	41
3.1 Introduction	42
3.2 Experimental Setup	44
3.3 Results and Discussions	49
3.3.1 The scaling	49

3.3.2	Radial Flow Between Parallel Plates	50
3.3.3	Scaling Drainage in Thin Porous Media	57
3.3.4	PTL Characterization	61
3.4	Conclusions	64
4.	<i>The effects of morphological and wetting properties of porous transport layers on water movement in PEM fuel cells</i>	65
4.1	Water Transport in PEM Fuel Cells	66
4.2	Simulation of Water Transport in the PTL	70
4.3	Modeling the Porous Transport Layer	73
4.4	Morphology Model 1 – Reference Cases	78
4.5	Effect of PTL Wettability	81
4.6	Effect of PTL Morphology	83
4.7	Effect of the MPL	86
4.8	Effect of MPL Defects on Water Transport	89
4.9	Conclusions	93
5.	<i>Comparison of numerical predictions and experimental results of water percolation in PEM fuel cell porous transport layers</i>	95
5.1	Introduction	96
5.2	Numerical Modeling	97
5.3	Numerical and Experimental Comparison	101
5.4	Conclusions	106
6.	<i>Summary and Recommendations</i>	109
6.1	Summary	109
6.2	Recommendations	112
	<i>References</i>	123
	<i>Appendices</i>	125
A.	<i>Numerical Model</i>	127
1.1	Discretization	127
1.2	Source Term	128
B.	<i>Copyright agreements</i>	131
2.1	Copyright agreements with Elsevier	132
2.2	Copyright agreements with the American Institute of Physics	136
2.3	Copyright agreements with the Electrochemical Society	142

LIST OF FIGURES

1.1	Flow chart describing the task flow developed in this work.	10
2.1	Drainage phase diagram.	15
2.2	SEM image of the Toray T060 DM layer under study, 100x magnification.	16
2.3	Experimental setup details.	19
2.4	Points in the drainage phase diagram explored experimentally. Dashed lines represent the hypothetical limits for each flow regime.	21
2.5	Three stages of the water-air percolation evolution for the two stable displacement flow regime experiments. Yellow lines identify the water-air interface. Water is inside and air is outside of region defined by the interface line. Right column images: time evolution for experiment at 0.228 ml s^{-1} ($C_a = 1.2 \times 10^{-3}$). Left column of images: time evolution for experiment at 0.059 ml s^{-1} ($C_a = 3.0 \times 10^{-4}$).	23
2.6	Nondimensional front length curves for the two stable displacement flow regime experiments. These nondimensional front lengths curves were calculated from the time evolution images of water-air interface. Experiments were performed injecting water and displacing air ($M = 64$) at different injection flow rate of 0.228 and 0.059 ml s^{-1} which correspond to $C_a = 1.2 \times 10^{-3}$ and $C_a = 3.0 \times 10^{-4}$, respectively.	24
2.7	Nondimensional wetted area curves for the two stable displacement flow regime experiments. These nondimensional wetted areas curves were calculated from the time evolution images of water-air interface. Experiments were performed injecting water and displacing air ($M = 64$) at different injection flow rate of 0.228 and 0.059 ml s^{-1} which correspond to $C_a = 1.2 \times 10^{-3}$ and $C_a = 3.0 \times 10^{-4}$, respectively.	25
2.8	Percolation pressure curves for the two stable displacement flow regime experiments. Experiments were performed by injecting water and displacing air ($M = 64$) at different injection flow rate of 0.228 and 0.059 ml s^{-1} which corresponds to $C_a = 1.2 \times 10^{-3}$ and $C_a = 3.0 \times 10^{-4}$, respectively.	26

2.15	Nondimensional wetted area curves for the two viscous fingering flow regime experiments. These nondimensional wetted areas curves were calculated from the time evolution images of air-water interface. Experiments were performed injecting air and displacing water ($M = 1.5 \times 10^{-2}$) at different injection flow rate of 0.5 and 0.228 ml s ⁻¹ which correspond to $C_a = 3.6 \times 10^{-5}$ and $C_a = 1.8 \times 10^{-5}$, respectively. . . .	34
2.16	Percolation pressure curve for the viscous fingering flow regime experiment. Experiment was performed by injecting water and displacing SAE 30 motor oil ($M = 3 \times 10^{-3}$) at flow rate of 2.5×10^{-4} which correspond to $C_a = 2.4 \times 10^{-6}$	35
3.1	Experimental setup.	46
3.2	PTL sample used in the pseudo Hele-Shaw experiment. Top corner: SEM image at 500x of the Toray T060 PTL sample.	47
3.3	Radial flow between two parallel plates.	51
3.4	C_e versus non-dimensional time for different reference capillary numbers for a radial flow between two non-wetting parallel plates	53
3.5	Slope of the C_e versus non-dimensional time for the different reference capillary numbers.	54
3.6	Effect of the viscosity ration on the C_e versus non-dimensional time for different reference capillary numbers.	55
3.7	Effect of the viscosity ration on the C_e versus non-dimensional time for different reference capillary numbers.	57
3.8	Typical water distribution for capillary fingering flow regime, $C_a = 3.1 \times 10^{-8}$. This image was taken after 7140 seconds on experiment 1. The yellow line identifies the interface between the water and air. . .	58
3.9	Typical water distribution for stable displacement flow regime, $C_a = 4.7 \times 10^{-4}$. This image was taken after 2.3 seconds on experiment 5. The yellow line identifies the interface between the water and air. . .	59
3.10	Toray T060 wetted area, A , for obtained for each experiment. Far left curve corresponds to stable displacement while the far right curve corresponds to capillary fingering.	60
3.11	Toray T060 percolation pressure, P , curves for each experiment. Top curve correspond to stable displacement while bottom curve corresponds to capillary fingering.	61
3.12	Toray T060 C_e versus non-dimensional time curves for each flow rate used and its associated reference capillary number.	62
3.13	C_e versus non-dimensional time curves for each PTL sample.	63

4.1	Schematic of computational domain and network model; blue indicates the nonwetting fluid (water), white the wetting fluid (gas) and gray the fiber structure. The computational domain encompasses the PTL and MPL if present spanning a single gas channel. Water is injected into the domain at the interface between the PTL and catalyst layer. . . .	72
4.2	Normalized PDF of each Weibull distribution used to generate the PTL pore size distributions for the network simulation plotted against the pore size (r), in μm . ψ and κ are the Weibull probability distribution shape and scale parameters, respectively.	75
4.3	Normalized PDF plot of each PTL pore size distribution generated by using the model 1 Weibull probability distribution.	79
4.4	Water distributions after the water reaches the gas flow channel for the three simulation cases generated from the baseline pore size distribution. The location of water is denoted in blue, white represents air, and black represents the fiber structure of the PTL. Simulations end times are 1192 (top), 522 (middle), and 1095 s (bottom).	80
4.5	Non-dimensional measures of saturation and pressure in the PTL for the three network simulations generated from the model 1 PDF ($\psi = 5.25$, $k = 3$). The simulation ends when the liquid water reaches the gas flow channel.	81
4.6	Effect of PTL wettability as measured by the static contact angle on the water percolation for the three cases generated using the model 1 PDF.	82
4.7	Non-dimensional front length (S^*), non-dimensional wetted area, (A^*), simulation end time (t_{max}), and average injection pressure (P_{avg}) for each pore size distribution listed in Table 4.1. The mean pore size corresponds to the PDF used to generate the PTL models. The bars indicate the maximum and minimum values obtained for the three cases in each morphology model.	85
4.8	Normalized PDF for each PTL pore size distribution generated by using the model 1 Weibull PDF with the addition of an MPL distribution. The distribution centered near $10 \mu\text{m}$ is the same as shown in Figure 4.2.	86
4.9	Water distributions when the water reaches the gas flow channel for the three cases generated from the model 1 PDF with an MPL. The area occupied by water is shown in blue, white represents air, and black represents the fiber structure of the PTL. The simulation end time are 250 (top), 120 (middle), and 100 s (bottom).	87

4.10	Non-dimensional measures of saturation and pressure in the PTL with MPL for the three network simulations generated from the model 1 PDF ($\psi = 5.25$, $k = 3$). The simulation ends when the liquid water reaches the gas flow channel.	88
4.11	Defect scenarios for morphology model 1, case 1 with $d^* \approx 0.01$. Top: Single pore of 32 μm width at the center of the MPL. Middle: Two pores of 16 μm width located side-by-side in the center of the MPL. Bottom: Two defects of 16 μm width equally spaced along the MPL. The simulation end time are 215 (top), 340 (middle), and 200 s (bottom).	90
4.12	Effect of the MPL defect on the water transport in the PTL for the three cases generated using the model 1 Weibull PDF. The MPL defect size is nondimensionalized by the width of the PTL.	91
5.1	Three dimensional network model schematic representation. E, W, N, S, T, B, and P stands for east, west, north, south, top and bottom nodes of the reference node P.	99
5.2	Weibull distribution function showing ψ and κ	100
5.3	Experimental C_e plot for Toray T060, 9% (wt) PTFE content. Solid line corresponds to the fitting curve of the experimental results while dashed lines correspond to experimental data for each capillary number tested.	103
5.4	Numerical and experimental C_e plot. Solid line corresponds to the fitting curve of the experimental results while dashed lines correspond to numerical simulation. The contact angles used in every simulation are indicated with annotations. The colors of the numerical C_e match the colors of the Weibull distribution used to generate its pore size distribution.	104
5.5	Water distribution after reaching one of the edges for the numerical simulation corresponding to $C_a = 6.0 \times 10^{-5}$, pore size distribution having $\psi = 5.25$ and $\kappa = 3$ Weibull parameters, and contact angle of 135° . The location of the water-air interface is denotes in blue.	105

LIST OF TABLES

2.1	Test conditions for each experiment. SD: Stable Displacement, CF: Capillary Fingering, VF: Viscous Fingering.	20
3.1	Experiment settings.	48
3.2	Linear regression coefficients for $\log C_e = b \log t^* + a$ fit to experimental data.	63
4.1	PTL parameters used in simulation results reported herein. The parameters varied include the Weibull distribution shape and scale factors, wettability, and presence of an MPL. The mean pore size corresponding to the Weibull distribution parameters is included for reference. The distributions are plotted in Figure 4.2. Morphology model 1 is used as the reference case and for the parametric studies on wetting and the effect of an MPL on water transport.	77

NOMENCLATURE

GDL	gas diffusion layer; referred to as PTL herein
MPL	microporous layer
PDF	probability distribution function
PEM	proton exchange membrane
PTFE	polytetrafluoroethylene
PTL	porous transport layer, also known as a gas diffusion layer
CCD	charge couple device
CMOS	complementary metal oxide semiconductor
PDMS	Polydimethylsiloxane
SEM	Scanning Electron Microscope

A	wetted area
A^*	normalized wetted area by the PTL area, $L \times H$
d	size of MPL defect
d^*	normalized MPL defect size, d/L
H	width of the PTL
l	pore length
L	length of the PTL
p_{ij}^c	capillary pressure
Δp_{ij}	pressure drop along the pore
q_{ij}	volumetric flow rate between nodes 'i' and 'j'
r_{ij}	pore radius between nodes 'i' and 'j'
\bar{r}_i	average pore radius around node 'i'
\bar{r}_j	average pore radius around node 'j'
r_m	average pore size for a given probability distribution
S	water-air interface front length
S^*	normalized front length by the PTL perimeter, $2(L + H)$
t	time
t_{\max}	simulation end time
Δt	integration time step
x_{ij}	non-wetting fluid position inside of the pore

σ	surface tension
θ	contact angle
κ	Weibull distribution scale parameter
μ_{ij}^e	effective viscosity
μ_{nw}	non-wetting fluid viscosity
μ_w	wetting fluid viscosity
ψ	Weibull distribution shape parameter
Q	flow rate, [cm^3s^{-1}]
μ_{nw}	non-wetting fluid viscosity
μ_w	wetting fluid viscosity
γ	non-wetting fluid surface tension
r_i	inlet pore radius
C_a	capillary number
M	viscosity ratio
t^*	non-dimensional time
C_e	energy ratio
h	smallest length scale
l	largest length scale
R_i	inner radius the parallel plates
R_{\max}	outer radius of the parallel plates

1. INTRODUCTION

1.1 Motivation

Proton exchange membrane (PEM) fuel cells have the potential to provide a clean energy to power a variety of application such as automotive, and domestic and industrial combined heat and power systems. In a PEM fuel cell, hydrogen and oxygen combine to generate water, heat and electricity. The hydrogen can be obtained from a variety of sources including renewable resources. While the electricity is generated for power supply, water and heat are the residuals products. This particular type of residuals products makes the PEM fuel cell an attractive clean solution to reduce contamination in places with large pollution like cities. One of the unsolved technical problems on the PEM fuel cells is water management. The generated water can be a barrier to achieve high efficiency and durability.

A typical PEM fuel cell consists of a series of porous layers on both sides of a thin polymer electrolyte membrane. Bipolar plates sandwich this assembly and distribute reactants across the cell. The proton exchange membrane conducts the positive charge, or protons, from the anode to the cathode. The proton exchange membrane must be hydrated in order to transport the protons. Negative charges, or electrons, must travel along the external electrical circuit.

The amount of water inside the fuel cell must be carefully controlled and distributed. If too much water is removed, the proton exchange membrane begins to dry out, thereby decreasing proton transport and consequently the fuel cell efficiency. If too little water is removed, water will begin to accumulate and block access of the reactants to the catalyst layer. Thus, the hydration of the PEM fuel cell is critical and it is the central concern of this research. Poor water management also accelerates degradation of the fuel cell.

The main challenge when studying the water distribution inside the fuel cell is visualization due to the opacity of its components. Visualization is crucial to determine the mechanisms controlling the water distribution. Two types of experimental setups coexist as research tools, ex-situ and in-situ experiments. In ex-situ experiments, fuel cell components are replaced with transparent materials and the water is directly observed. In in-situ experiments, the fuel cell components remain the same, and the water distribution is obtained through a post-processing of an intermediate variable. Examples of this are nuclear magnetic resonance, neutron imaging, as well as other techniques.

The small size of the PTL pores in combination with its coating (the PTLs are coated with polytetrafluoroethylene, PTFE, which makes surfaces non-wetting or hydrophobic) can trigger unstable flow patterns where water percolates through the PTL forming conduits or fingers. This flow pattern is known as capillary fingering. However unlikely to happen under the normal fuel cell operating conditions, another two flow patterns can develop on non-wetting porous media: stable displacement and viscous fingering. These three flow patterns are summarized in the drainage flow diagram [35]. If the porous media surface is wetting, scenario unlikely to be found in fuel cells, a different set of flow patterns can occur and are presented on a imbibition

flow diagram [34]. The imbibition flow patterns are not considered in this thesis.

Even though the most likely flow pattern occurring in a fuel cell is capillary fingering [43], a fundamental study of the capillary effect on water management has largely been missing from fuel cell research. During the first stage of the research, an ex-situ experimental setup was designed with the dual purpose of gaining visual access to the water distribution inside the fuel cell and quantifying the amount of water held in the porous transport layer, PTL, of a PEM fuel cell.

The most common approach to model flow in porous media is through the use of concept of porosities and permeabilities. The porosity and permeability approaches to modeling liquid water transport in the PTL using techniques such as the J-Leverett function [36] can be considered as static saturation models. That is, the models are developed based on equilibrium configurations of water volume and pressure in a porous medium. Within an operating fuel cell the balance between viscous effects, capillary pressure, and the morphology of the PTL is key to predicting water transport. In order to study the water percolation within a PTL, the pore-level capillary pressure must be included in any model. As such, the pore size distribution has a more significant meaning in describing PTL water transport than does porosity or permeability. Average properties such as porosity and permeability are insufficient to capture the two-phase capillary-driven flow behavior. When using the J-Leverett function to correlate saturation to pressure, the flow resistance will have to be handled through a Darcy-type law where effective permeability is used to modify the area available for gas transport. This approach will work if the flow rates are sufficiently large. However, for a fuel cell operating under normal conditions, the rate of water production results in small flow rates so that the movement of water in a PTL takes the form of capillary fingering [43]. Full saturation is never reached with capillary

fingering. Water will move through a subset of pores, typically the largest and/or the least wetting pores, at approximately constant capillary pressure independent of the saturation level.

As explained by Weber et al. [62] in their modeling review article, the J-Leverett function was developed for uniform wettability and pore aspect ratio which is not the scenario found in PTL water transport. The conclusion is that porosity and permeability are not suitable measures for describing liquid water transport through the PTL. In addition, the J-Leverett function and associated porosimetry methods were developed for soil percolation studies where fluid flow is driven by a constant hydraulic pressure. Fuel cells operate under a constant flow rate condition with the water production rate proportional to the current density.

A network model is often utilized when pore-level dynamics are important to liquid transport in a porous medium. The basic premise of the network model is that both fluids can be modeled as Poiseuille flow. The morphology of the porous layer is modeled as a lattice of tubes of random diameters. Two additional terms are included with the conventional Poiseuille flow relation which model the capillary pressure and the effective viscosity when both fluids are simultaneously present in a tube. The network model has been shown to accurately simulate two-phase capillary-driven flow in porous media [35]. Vogel et al. [61] compared a number of traditional methods used to simulate two-phase flow in porous media concluding that the network model is the simplest, least computationally expensive, and has an accurate representation of the phenomena; especially when the pore size distribution is important.

Changes to the wettability and morphology of the PTL are anticipated to influence the amount of liquid water present in the PTL. The wettability of the PTL is typically changed by varying the amount of PTFE present. The PTL morphology change

which has received the greatest attention has been the addition of a microporous layer (MPL).

The understanding of the effects of wetting and morphological properties of the PTL on the water percolation is crucial for developing water management strategies, especially at high current density. There are discrepancies between research results on the water percolation through the PTL with respect to the effect of the pore size distribution, contact angle, PTFE content, water state when crossing the MPL, and the role of the MPL in improved fuel cell performance. This project emphasizes the role of the capillary effect on the water management on PEM fuel cells. An optimum combination of PTL structural, morphological and wettability properties which minimizes mass transport losses is sought. To that end, a parametric investigation of PTL properties which influence the water transport is conducted.

One research question that still has to be properly addressed is how those simulation can be validated/corroborated against experimental data? Answering this question implies also answering the question on how the porous media can be characterized based on drainage flow patterns. If a method for characterization is found, then the same method can be used to validate the numerical simulations. Normally, during drainage in porous media, water dispersion or pressure gradient versus saturation are measured in the experiments and used to decide which flow pattern is occurring. The flow pattern can be cataloged using the drainage phase diagram by its visual appearance using the drainage phase diagram. The drainage phase diagram allows to identify the transition between stable displacement and capillary fingering but the transition between both flow regimes is wide and not suitable to use for validation nor characterization of the porous media. On the other hand, the characterization/validation can be done by comparing the percolation pressure versus saturation measurements

such as the J-Leverett J-function [36]. However, these comparison are not able to distinguish between capillary fingering or stable displacement. One of the objective of this project is also to develop a tool the allows characterization of the porous media and therefore validate numerical simulations using an output strongly dependent of the drainage flow patterns as well as the porous media properties. This method is based on the ratio between injected and dissipated energies, which can be derived by combining the measurements of the water dispersion and the percolation pressure.

It is expected that different porous media with different porous structure and wettability properties will dissipate the energy in different ratios allowing for distinct characterization. The numerical simulations have to developed with proper boundary condition representative of the experiments in which these variable are measured. The numerical simulation are then corroborated under those conditions by tuning the porous media wettability and structure properties. The resulting porous media structure can be later used to simulate the water percolation in a fuel cell with the appropriate boundary conditions. Using this method to validate the numerical simulation of the water percolation in porous media independently of the fuel cell operation condition has the advantage over validations based on the comparison of the polarization curve where many other effects are couple and the leading to a miss understanding of the simulation results.

1.2 Outline

This project is divided into three themes: experimental observation, numerical modeling and final recommendations. The experimental setup has multipurpose goals

of (i) identifying the possible flow regimes than can occur in a PTL, (ii) identifying the mechanism involved in each flow regime, (iii) identifying which one mechanisms are critical during a fuel cell operation, and (iv) providing a tool to characterize different PTL based on the susceptibility to these flow regimes. The method proposed to characterize PTL can also provide a tool to validate the numerical modeling.

The numerical modeling is developed with the objectives of helping explain the experimental observations and studying the effects of PTL properties on the water transport in simulated fuel cell conditions.

The final recommendations are based on the results from the numerical simulations and the experimental measurements. Characterization of the PTL will lead to the creation of a database where different PTL can be cataloged to be later used according to a desired transport behavior. The numerical simulation can be tuned based on this database and the resulting simulated PTL used to explore a fuel cell. Figure 1.1 summarize the work flow proposed in this project. These three themes are developed in a six chapters

- **Chapter 1: Introduction:** the motivation behind this project as well as the goals are presented. The task flow and the material required are presented.
- **Chapter 2: Experimental Setup:** design of an experimental setup to identify the most relevant mechanisms acting during water percolation through the PTL.
- **Chapter 3: PTL Characterization:** develop criteria to characterize different PTL based on their susceptibility to the drainage flow patterns. A new scaling for drainage in porous media based on the ratio between input and dissipated

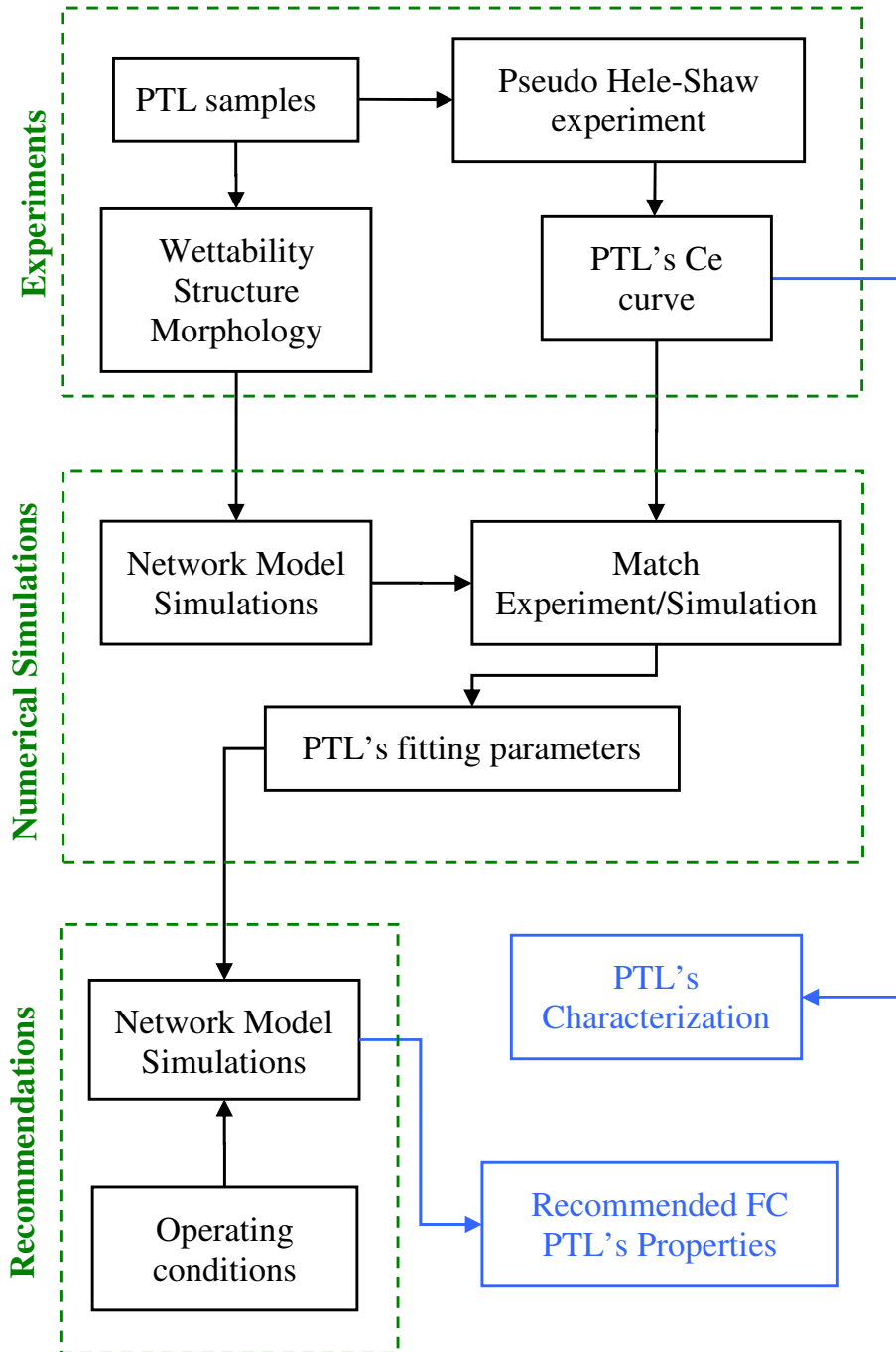


Figure 1.1. Flow chart describing the task flow developed in this work.

energies is proposed. Different PTLs, from different manufacturers, were tested and the results presented in terms of the proposed scaling.

- **Chapter 4: Numerical Model:** modeling the PTL transport properties by modifying the existing transport model successfully used in porous media [35]. The effect of the wettability properties, structural properties like pore size distribution, PTFE coating concentration, boundary conditions, among others will be taken in consideration.
- **Chapter 5: Corroboration of the Numerical Simulation:** a series of numerical simulation are carried out mimicking the experimental conditions setup described in Chapter 2 and the results compared against the experimental measurements by using the proposed scaling for drainage in porous media described in Chapter 3.
- **Chapter 6: Summary and Future Work:** final recommendations and step to develop are presented .

2. EXISTENCE OF THE PHASE DRAINAGE DIAGRAM IN PEM FUEL CELL FIBROUS DIFFUSION MEDIA

It is well established that drainage in porous media can be characterized by two nondimensional numbers: the capillary number, C_a , and the viscosity ratio, M . Both quantities are useful to distinguish which force (viscous or capillary) is governing the fluid displacement behavior. This information is summarized in the C_a - M phase diagram. The C_a - M phase diagram is strongly dependent upon fluid properties and the porous medium morphology and wettability. Experimental evidence suggests that the morphology of the porous medium has an important role in the behavior in the fluid displacement. In this work, C_a - M phase diagram of fuel cell Diffusion Media layer (DM) is explored using a pseudo-Hele-Shaw experimental setup. This phase diagram will be explored together with the characteristic pressure curves of each displacement type. This C_a - M phase diagram will provide a fundamental resource for understanding the dynamics of the diffusion process and transport characteristics taking place inside of the DM as well as a characterization method for DMs.

Note: Reprinted from Publication title, 191/2, E. F. Médici and J. S. Allen, Existence of the phase drainage diagram in proton exchange membrane fuel cell fibrous diffusion media, 417-427, Copyright 2009, with permission from Elsevier. Copyright agreement in Appendix B section 2.1.

2.1 Introduction

Drainage is the displacement of a wetting fluid by the injection of a nonwetting fluid. When drainage takes place in porous media three types of fluid flow behavior can arise. One type of flow is originated when the injected fluid has lower viscosity than the displaced fluid. The injected fluid permeates irregularly through the porous material resulting in the formation of multiple conduits or fingers. This resulting flow distribution is characterized by fingers of approximately the same size and is called viscous fingering. The other two types of flow are created when the injected fluid has higher viscosity than the displaced fluid. If the injection flow rate is relatively slow, the injected fluid again generates irregular conduits within the porous media. The resulting flow distribution is characterized by the formation of a few fingers of different sizes and is called capillary fingering. If the injection flow rate is relatively high, the injected fluid permeates evenly through the porous media without finger formations; this resulting flow distribution is called stable displacement. Lenormand et al. [34, 35] presented a phase diagram that summarizes these three types of flow distribution in porous media in a single chart, called Drainage Phase Diagram, illustrated in Figure 2.1. This phase diagram is based on two nondimensional parameters, the capillary number, C_a , and the viscosity ratio, M :

$$C_a = \frac{V\mu_{nw}}{\sigma} \quad (2.1)$$

$$M = \frac{\mu_{nw}}{\mu_w} \quad (2.2)$$

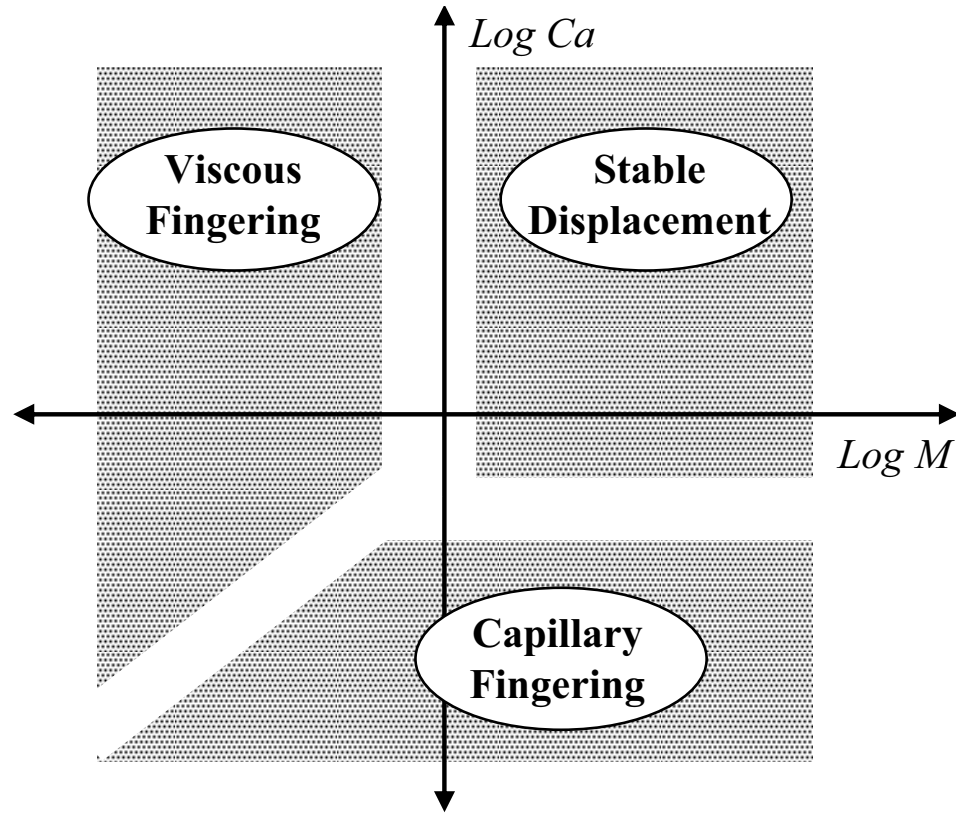


Figure 2.1. Drainage phase diagram.

where v is the fluid velocity, μ_w and μ_{nw} are the wetting and nonwetting fluids viscosities, and σ is the surface tension.

These flow instabilities in porous media, viscous and capillary fingering, have been an object of study for a long time [1, 21, 24] and in diverse applications such as oil recovery [32], drug delivery [57], water transport in soil [48], among others; but it has been largely omitted from fuel cell research.

A typical Proton Exchange Membrane (PEM) fuel cell consist of a series of porous layers compressed between bipolar plates. These layers, starting from the anode side, are the Diffusion Media layer, DM, (5-10 μm pore size and 150-400 μm thick), the Micro Porous Layer, MPL, (100-500 nm pore size and 10-20 μm thick), the catalyst

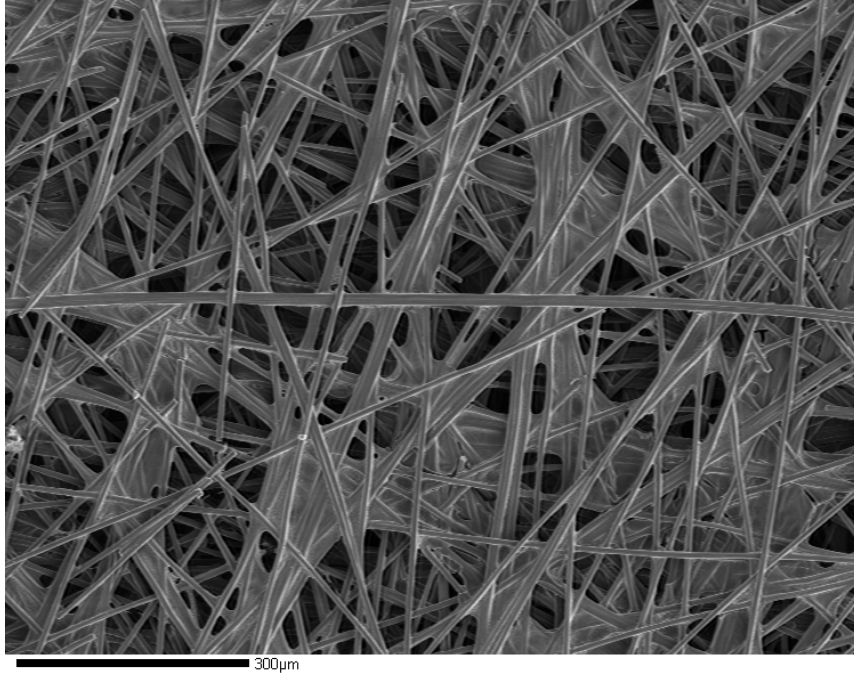


Figure 2.2. SEM image of the Toray T060 DM layer under study, 100x magnification.

layer or electrode ($0.1\text{-}1\ \mu\text{m}$ pore size and $5\text{-}30\ \mu\text{m}$ thick), the proton exchange membrane ($50\text{-}200\ \mu\text{m}$ thick). These layers repeat on reverse order in the cathode side. Figure 2.2 shows SEM images of a diffusion media layer at 100x magnification. These layers are generally treated with a polytetrafluoroethene (PTFE) coating making the pore surface hydrophobic.

The amount of water generated inside the fuel cell must be carefully controlled and distributed [37]. Remove too much water and the PEM begins to dry out, thereby decreasing proton transport. Remove too little water and it begins to accumulate, blocking the access of the reactants to the catalyst layer which stops the chemical reaction and reduces the cell efficiency. Also, water accumulation may locally prevent the flow of reactants through the bipolar plate channels, reducing the chemical reaction rate upstream and increasing the degradation of the fuel cell components.

Thus, water management is critical to reliable PEM fuel cell operation. There have been a numerous studies to improve the water management in PEM fuel cells including: external humidification [10], size and profile of the bi-polar plates channels [38], thickness and porosity of the layers [25, 50] , the addition of the MPL [52], wettability of the layers [12], among others.

Experimental evidence suggests that the water distribution inside of the DM is not uniform and water is transported in a fingering-type flow. Litster et al. [39] present evidence of the fingering type of pattern using fluorescence microscopy. In their experiment, distilled water with fluorescence dye was injected into a DM from the bottom surface, obtaining a “through plane” percolation. Also, evidence of nonuniform water distribution was found using magnetic resonance imaging by Tsushima et al. [60], as well as neutron imaging by Satija et al. [54]. Sinha et al. [55], using a simple calculations for the water generated in a fuel cell under normal operating conditions and the drainage phase diagram, suggested that the main regime expected in a fuel cell is capillary fingering. In this calculation, the effect of different pore size along the different layers was not taken into account. Kimball et al. [23] suggest that water will flow along the DM only through the largest pores, but they omit the effect of the MPL in their discussion. Despite all this evidence of capillary driven flow, there has not been a fundamental study of capillarity and drainage flow patterns on fuel cell water management.

The objective of this study is to explore the three types of drainage flow in DM separately and gain knowledge of the water behavior inside of the DM which may occur during the operation of the fuel cell. The understanding of these basic mechanisms will be useful for developing reliable robust water management strategies in low temperature fuel cells.

2.2 Experimental Setup

The diffusion media used for this study is Toray T060 with a pore size distribution in the range of 5-10 μm and a 9% by mass PTFE treatment. Figure 2.2 shows an SEM image of the sample used at 100x magnification. This $5 \times 5 \times 0.02$ cm sample is placed in a cell between two layers of polydimethylsiloxane (PDMS). PDMS is a transparent, compliant, and hydrophobic silicon material used to seal the top and bottom surfaces of the diffusion media ensuring water percolation within the diffusion media while maintaining visual access. Figure 2.3 illustrates the PDMS-DM-PDMS cross section, which is referred to as a pseudo-Hele-Shaw cell. To prevent filtration between the PDMS and the DM surfaces, the cell layers were compressed between two pieces of PlexiglasTM surrounded by a metallic frame which was held in place by four screws. The screws were adjusted to produce a 20 KPa compression pressure over the test sample, which generates a 0.05% strain deformation (0.1 μm compression). Four springs were also placed between the frames in order to obtain uniform compression along the cell.

A Kulite XCS062100 differential pressure transducer located in the inlet tubing was used to measure the percolation pressure. The pressure was recorded using a Keithley 2700 digital multimeter at intervals of 0.1 seconds. A camera located at 0.5 m from the cell was used to collect images of the drainage during the experiment. Due to the different time scales of the experiments, two types of camera were used. A Panasonic GP-KS125 CCD camera was used for the capillary fingering set of experiments, while a high speed Photron Fastcam-Ultima APX-RS CMOS camera was used for the stable displacement and viscous fingering set of experiments. In order to have enough contrast between the injected and the displaced fluid in the DM and

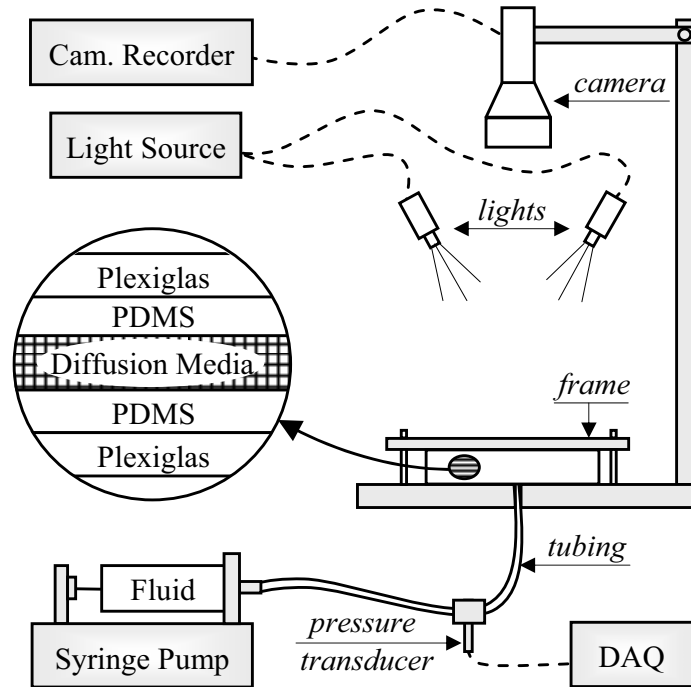


Figure 2.3. Experimental setup details.

to avoid camera self-reflection from the cell, a diffusive illumination system was used. The working fluid was injected through a 2 mm diameter hole located in the middle of the bottom PDMS layer using a syringe pump at a constant flow rate. Two different syringe pumps were used. An ultra-low flow rate syringe pump, Harvard Apparatus model 2274, was used for the capillary fingering set of experiments, while a Harvard Apparatus model 938 syringe pump was used for the stable displacement and viscous fingering set of experiments. The flow rate and the working fluid could be varied in order to explore different points in the drainage phase diagram. The flow rate was changed to set different capillary numbers and the working fluid was changed to set different viscosity ratios. A reference capillary number, C_a , for each experiment was calculated at the inlet using equation (2.1), where the inlet velocity v was calculated as $v = q/\pi r^2$, where q is the volumetric flow rate and r is the radius of the inlet

tube. The reference viscosity ratio, M , for each experiment was calculated using equation (2.2), where the terms wetting and nonwetting fluid refer to the displaced and injected fluids respectively. Table 2.1 summarizes the flow rates, working fluids, capillary number, among other technical data used during each experiment. The test sample was placed in a desiccator for approximately 24 hours prior to each experiment run.

Table 2.1. Test conditions for each experiment. SD: Stable Displacement, CF: Capillary Fingering, VF: Viscous Fingering.

Regime	Fluids	M	q (ml s ⁻¹)	C_a	Frame Rate (fps)
SD	Water/air	64	0.228	1.2×10^{-3}	60
SD	Water/Air	64	0.059	3.0×10^{-4}	250
CF	Water/Air	64	2.1×10^{-5}	1.1×10^{-7}	0.06
CF	Water/Air	64	5.6×10^{-6}	3.0×10^{-8}	0.05
VF	Air/Water	1.5×10^{-2}	0.5	3.6×10^{-5}	500
VF	Air/Water	1.5×10^{-2}	0.228	1.8×10^{-5}	500
VF	Water/Oil	3×10^{-3}	2.5×10^{-4}	2.4×10^{-6}	-

Three different sets of experiments, designed to explore each of the three possible fluid behaviors shown on the drainage phase diagram, were performed. In the stable displacement experiments, air was displaced from the DM by injecting water at a high flow rate. During the capillary fingering experiments, air was displaced from the DM by injecting water at a low flow rate. In the viscous fingering experiments, water was displaced from the DM by injecting air or oil was at a high flow rate. Figure 2.4 shows the capillary number, C_a , and viscosity ratio, M , of each experiment in the drainage phase diagram.

From the experiments, the top view images of the percolation evolution and the percolation pressure curve were recorded in parallel. The images from the CCD camera were collected using EPIX PIXCI imaging board and XCAP frame grabber, while

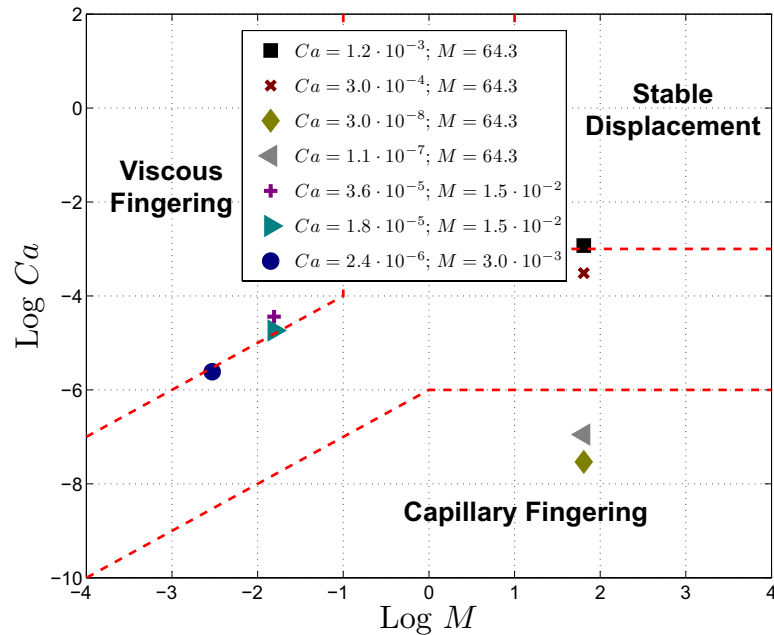


Figure 2.4. Points in the drainage phase diagram explored experimentally. Dashed lines represent the hypothetical limits for each flow regime.

the images from the CMOS camera were collected using Fastcam Viewer software. From these images, the percentage of the total area occupied by the injected fluid and the interface of injected-displaced fluids were calculated for each test. The time evolution of the occupied area is referred to as a saturation curve, while the time evolution of the fluid-fluid interface is referred to as a front length curve. To obtain these saturation and front length curves, an image post-processing analysis was performed.

2.2.1 Image Post-Processing

The procedure to obtain the fluid-fluid interface began by transforming the collected images to gray scale. A background reference image of the DM before the percolation started was subtracted from each image. By applying a threshold value to the dif-

ference between actual and reference pictures, the location of injected and displaced fluids can be easily identified. The interface between the injected and displaced fluids was captured using an edge detection algorithm written in Matlab. The interface was reconstructed by plotting the border points, indicated by the line superimposed on Figure 2.5 for stable displacement, Figure 2.9 for capillary fingering, and Figure 2.13 for viscous fingering.

The area saturated with injected fluid from the top view is referred as the wetted area, and is denoted as A . The interface line between the injected and displaced fluid is referred to hereafter as the front length, S . Using the described technique, the wetted area, A , and the front length, S , were calculated at each time interval. The front length and the wetted area were nondimensionalized using the length and width of the test sample, L and H , respectively. The front length is nondimensionalized by the perimeter of the test sample $2(L + H)$ and the wetted area is nondimensionalized by the projected area of the test sample $L \times H$.

2.3 Observations

2.3.1 Stable displacement

When the injection flow rate is high enough to have a C_a number greater than 10^{-3} and the viscosity ratio between the injected and displaced fluids is greater than one, the drainage flow regime is stable displacement. The stable displacement flow regime is characterized by a flow pattern where all pores sizes are filled. Starting from the center injection hole, the injected fluid will fill all the pores until it reaches the edge of the test sample and the experiment ends. The interface between injected and

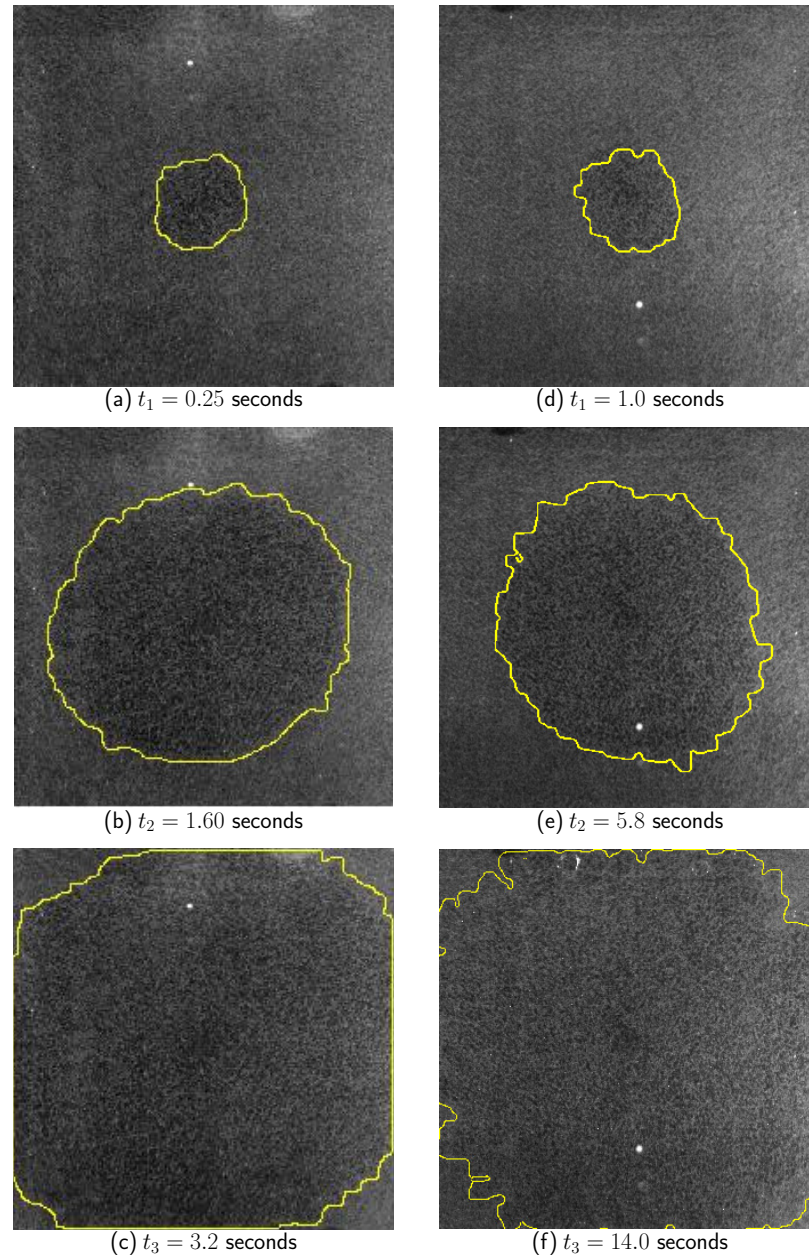


Figure 2.5. Three stages of the water-air percolation evolution for the two stable displacement flow regime experiments. Yellow lines identify the water-air interface. Water is inside and air is outside of region defined by the interface line. Right column images: time evolution for experiment at 0.228 ml s^{-1} ($C_a = 1.2 \times 10^{-3}$). Left column of images: time evolution for experiment at 0.059 ml s^{-1} ($C_a = 3.0 \times 10^{-4}$).

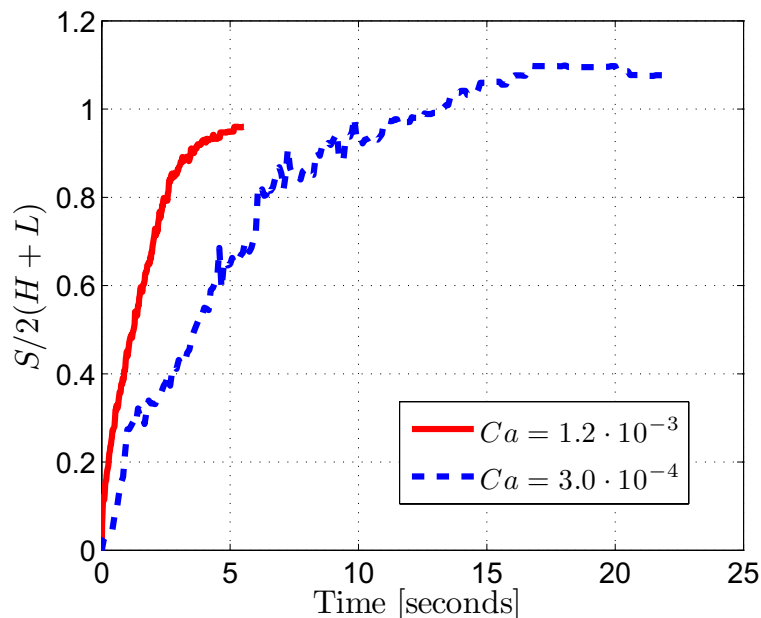


Figure 2.6. Nondimensional front length curves for the two stable displacement flow regime experiments. These nondimensional front lengths curves were calculated from the time evolution images of water-air interface. Experiments were performed injecting water and displacing air ($M = 64$) at different injection flow rate of 0.228 and 0.059 ml s⁻¹ which correspond to $C_a = 1.2 \times 10^{-3}$ and $C_a = 3.0 \times 10^{-4}$, respectively.

displaced fluids can be assumed as a circular line shape (from a top view) concentric to the injection hole. In this stable displacement set of experiments, air was displaced by injecting water (viscosity ratio of $M = 64$). The flow rates used were 0.228 and 0.059 ml s⁻¹ which results in a C_a of 1.2×10^{-3} and 3.0×10^{-4} , respectively. Images were collected using the CMOS camera at 60 and 250 fps respectively. Three stages of the water percolation evolution for the two injection flow rates are shown in Figure 2.5. These figures include the interface line between the injected and displaced fluids.

From the experiment images, the front length S and wetted area A curves were calculated for each image. The nondimensional front length curves, Figure 2.6, and the nondimensional wetted area curves, Figure 2.7, reach a peak value and then

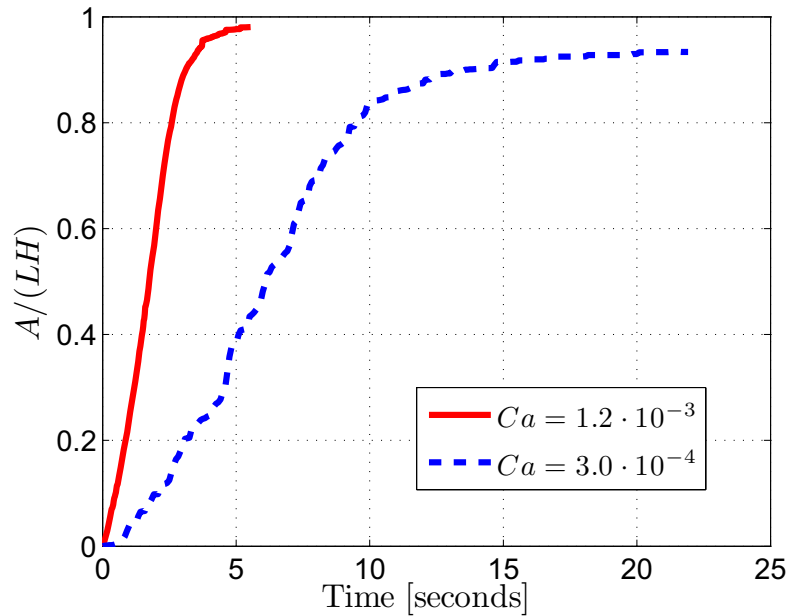


Figure 2.7. Nondimensional wetted area curves for the two stable displacement flow regime experiments. These nondimensional wetted areas curves were calculated from the time evolution images of water-air interface. Experiments were performed injecting water and displacing air ($M = 64$) at different injection flow rate of 0.228 and 0.059 ml s⁻¹ which correspond to $C_a = 1.2 \times 10^{-3}$ and $C_a = 3.0 \times 10^{-4}$, respectively.

plateau after an initial transient period. The lower C_a experiment has the lower steady wetted area (lower saturation level) and the higher steady front length. The steady front length is greater than one which can be explained using the phase diagram. Due to the proximity to the transition region between the stable displacement and capillary fingering, the uniform shape of stable displacement begins to develop small capillary fingers. This effect can be seen in Figure 2.5(f). The presence of these fingers reduces the level of saturation, increases the interface front length, and increases the time to reach saturation.

The corners of the cell will never be wetted and saturation level will be always lower than one because the injected fluid spreads circular until it reaches the edges

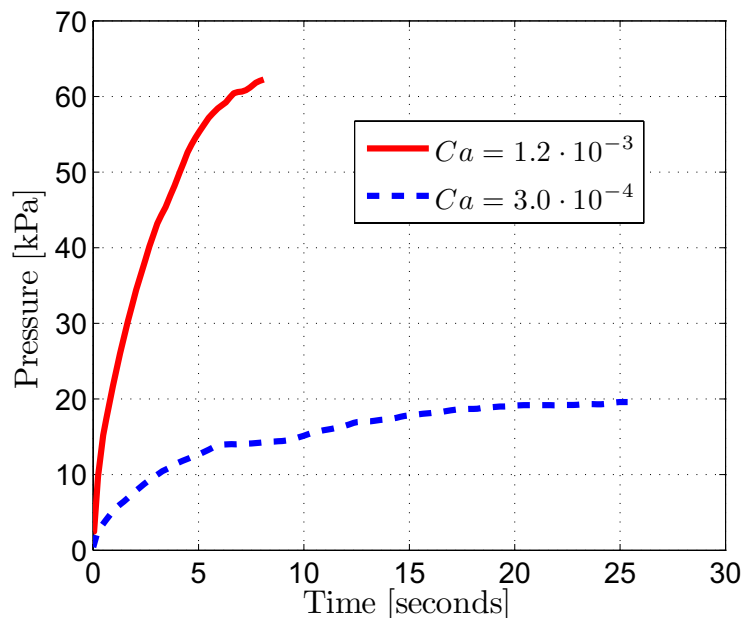


Figure 2.8. Percolation pressure curves for the two stable displacement flow regime experiments. Experiments were performed by injecting water and displacing air ($M = 64$) at different injection flow rate of 0.228 and 0.059 ml s⁻¹ which corresponds to $Ca = 1.2 \times 10^{-3}$ and $Ca = 3.0 \times 10^{-4}$, respectively.

of the test sample (it will reach the middle of all the side edges at approximately the time) and the experiments ends.

The pressure drop during percolation exhibits an gradual growth as water is injected, shown in Figure 2.8. Additional pressure is required to inject more water in order to displace the previously injected water. Also, the greater the capillary number the higher the fluid velocity and the larger the required pressure drop.

2.3.2 Capillary Fingering

The capillary fingering drainage flow regime is characterized by a very slow injection flow rate and therefore a very small Ca . This slow flow rate allows the injected fluid

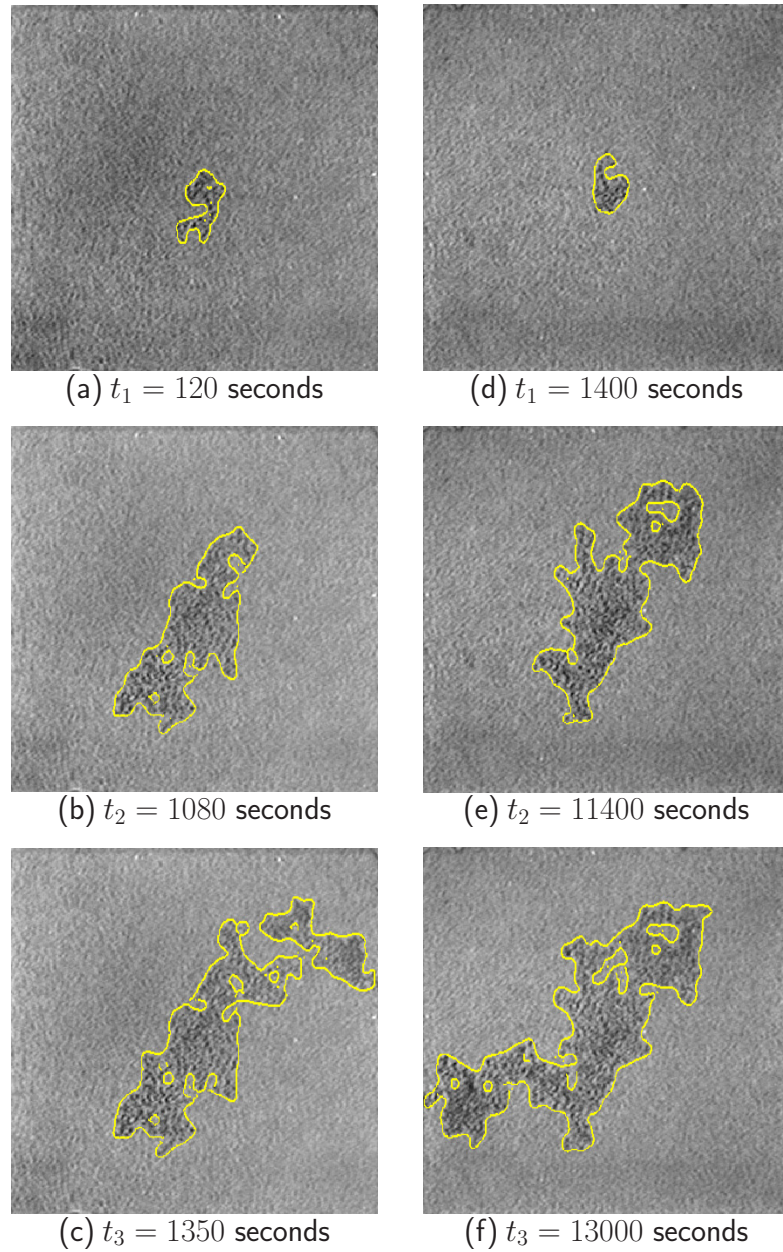


Figure 2.9. Three stages of the water-air percolation evolution for the two capillary fingering flow regime experiments. Yellow lines identify the water-air interface. Water is inside and air is outside of region defined by the interface line. Right column images: time evolution for experiment at 2.1×10^{-5} ml s $^{-1}$ ($C_a = 1.1 \times 10^{-7}$). Left column of images: time evolution for experiment at 5.6×10^{-6} ml s $^{-1}$ ($C_a = 3.0 \times 10^{-8}$).

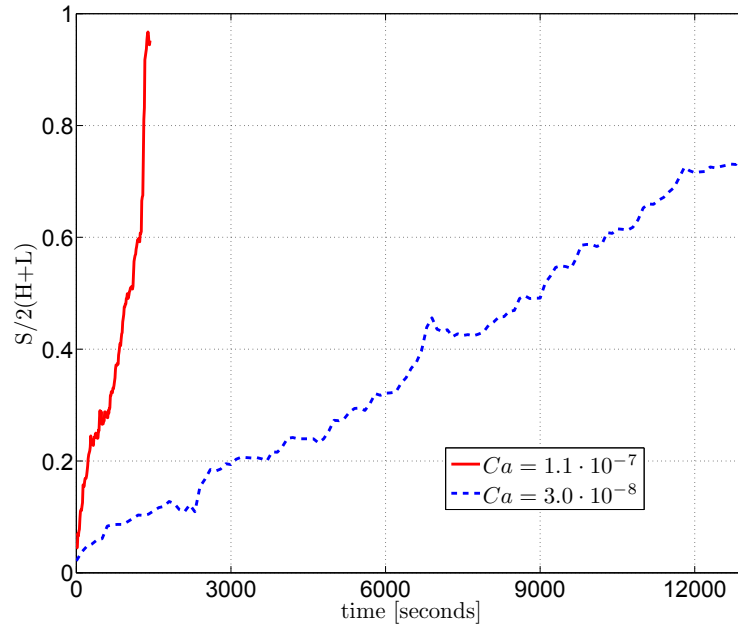


Figure 2.10. Nondimensional front length curves for the two capillary fingering flow regime experiments. These nondimensional front lengths curves were calculated from the time evolution images of water-air interface. Experiments were performed injecting water and displacing air ($M = 64$) at different injection flow rate of 2.1×10^{-5} and 5.6×10^{-6} ml s^{-1} which correspond to $Ca = 1.1 \times 10^{-7}$ and $Ca = 3.0 \times 10^{-8}$, respectively.

to reach a quasi-steady capillary equilibrium. Starting from the injection hole, the injected fluid will percolate only through the pores that offer the smallest capillary resistance. These low capillary resistant pores are the largest pores or the pores with small internal contact angle [19]. This type of fluid flow no longer has the uniform circular shape obtained in stable displacement flow regime. On the contrary, this flow pattern is characterized by the formation few irregular conduits or fingers through the porous media. The experiment ends when the injected fluid reaches one of the edges of the test sample.

During this capillary fingering set of experiments, air was displaced by injecting

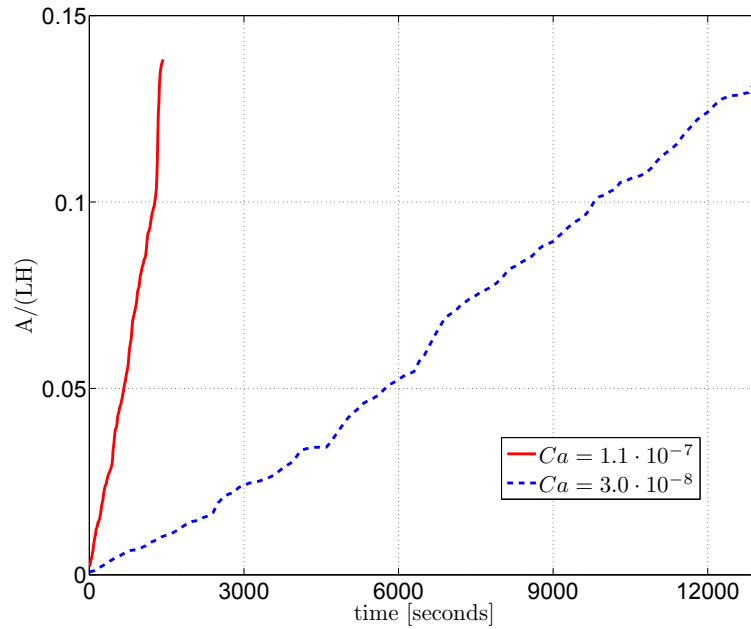
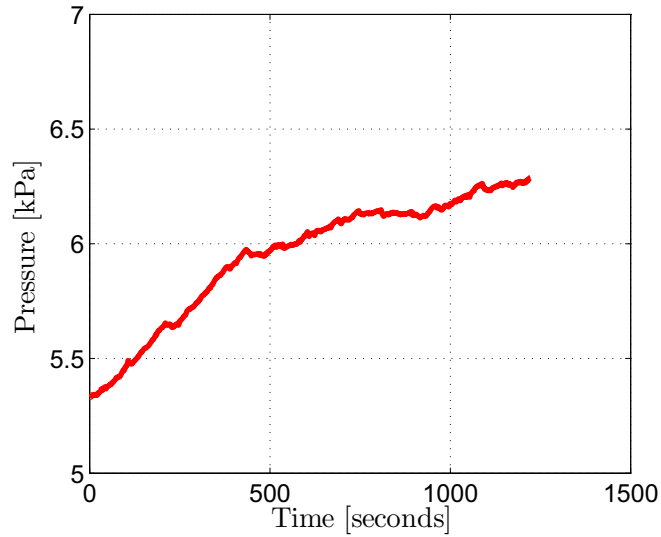


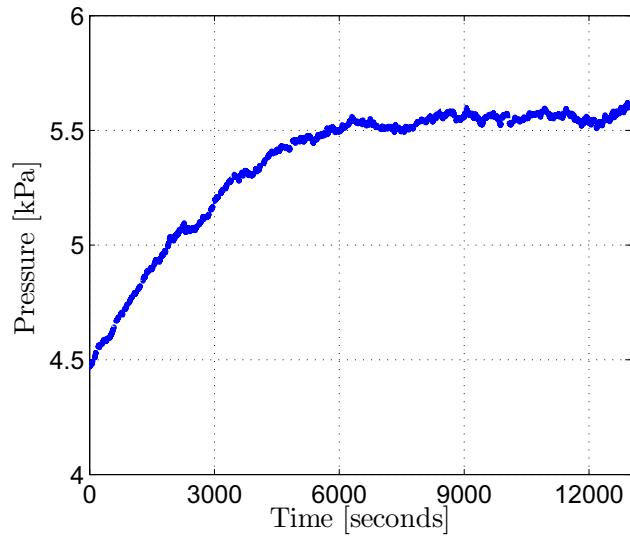
Figure 2.11. Nondimensional wetted area curves for the two capillary fingering flow regime experiments. These nondimensional wetted areas curves were calculated from the time evolution images of water-air interface. Experiments were performed injecting water and displacing air ($M = 64$) at different injection flow rate of 2.1×10^{-5} and 5.6×10^{-6} ml s^{-1} which correspond to $Ca = 1.1 \times 10^{-7}$ and $Ca = 3.0 \times 10^{-8}$, respectively.

water (viscosity ratio of $M = 64$). The flow rates used were 2.1×10^{-5} and 5.6×10^{-6} ml s^{-1} which results in a Ca of 1.1×10^{-7} and 3.0×10^{-8} , respectively. In order to achieve these flow rates, an ultra-low flow rate syringe pump, Harvard Apparatus model 2274, was used. Images were collected using the CCD camera at 0.06 and 0.05 fps, respectively. Three stages of the water percolation evolution for the two different injection flow rates are shown in Figure 2.9. These figures include the interface line between the injected and displaced fluids.

From the experiment images, front length S and the wetted area A curves were calculated. The capillary fingering regime is characterized by incomplete saturation



(a) $C_a = 1.1 \times 10^{-7}$.



(b) $C_a = 3.0 \times 10^{-8}$.

Figure 2.12. Percolation pressure curves for the two capillary fingering flow regime experiments. Experiments were performed by injecting water and displacing air ($M = 64$) at different injection flow rate of 2.1×10^{-5} and $5.6 \times 10^{-6} \text{ ml s}^{-1}$ which correspond to $C_a = 1.1 \times 10^{-7}$, Figure (a), and $C_a = 3.0 \times 10^{-8}$, Figure (b), respectively.

of the media. Therefore, the nondimensional front length curves, Figure 2.10, and the nondimensional wetted area curves, Figure 2.11, show a lower saturation level when compared to the stable displacement saturation level.

In the capillary fingering regime, the percolation pressure has an initial gradual growth which levels off to a constant pressure as water is injected. When the pressure in the syringe is higher than the capillary pressure in the DM, the water-air interface moves (meniscus displacement). However, due to the low flow rate, there is not enough volume of water to keep the meniscus moving continuously and the interface motion stops. Percolation subsides until the system reaches a quasi-steady equilibrium and the pressure in the syringe pump exceeds the capillary pressure. Thus, the pressure curve oscillates around the capillary pressure, as seen in Figure 2.12 (b).

As the C_a increases, less time is required for the water to reach one of the edges. At the higher C_a , the flow regime approaches the intermediate region between stable displacement and capillary fingering, the quasi-steady capillary equilibrium displacement is no longer achieved and the pressure continuously increases during the percolation as shown in Figure 2.12(a). The increased fluid velocity results in an increased initial pressure at which the percolation begins. The initial pressure was 5.3 ± 0.35 kPa for $C_a = 1.1 \times 10^{-7}$ while for $C_a = 3.0 \times 10^{-8}$ and the initial pressure was 4.5 ± 0.35 kPa.

2.3.3 Viscous Fingering

When the injected fluid has lower viscosity than the displaced fluid, the drainage flow regime is viscous fingering. Due to the low viscosity of the injected fluid the percolation pressure continuously decreases until the injected fluid reaches the edge of the test sample. The pressure levels off to a minimum value and the experiment

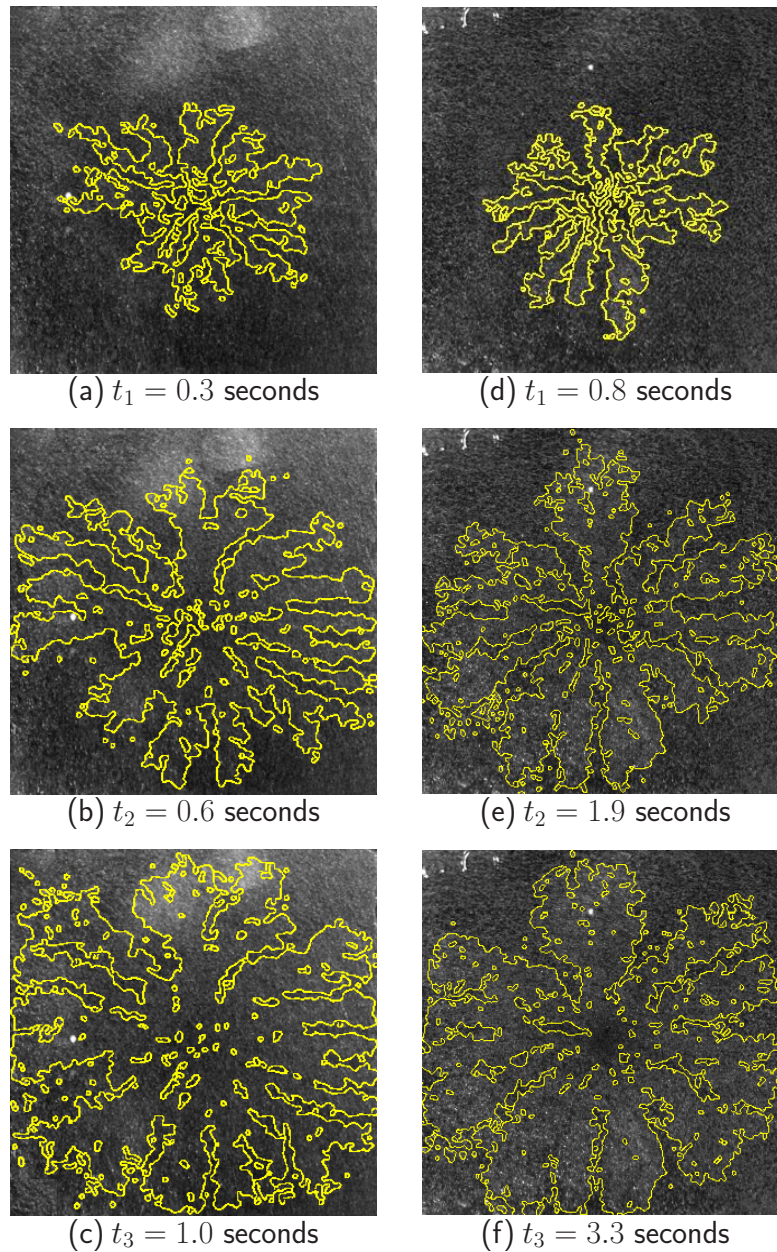


Figure 2.13. Three stages of the air-water percolation evolution for the two viscous fingering flow regime experiments. Yellow lines identify the air-water interface ($M = 1.5 \times 10^{-2}$). Air is inside and water is outside of region defined by the interface line. Right column images: time evolution for experiment at 0.5 ml s^{-1} ($C_a = 3.6 \times 10^{-5}$). Left column of images: time evolution for experiment at 0.228 ml s^{-1} ($C_a = 1.8 \times 10^{-5}$).

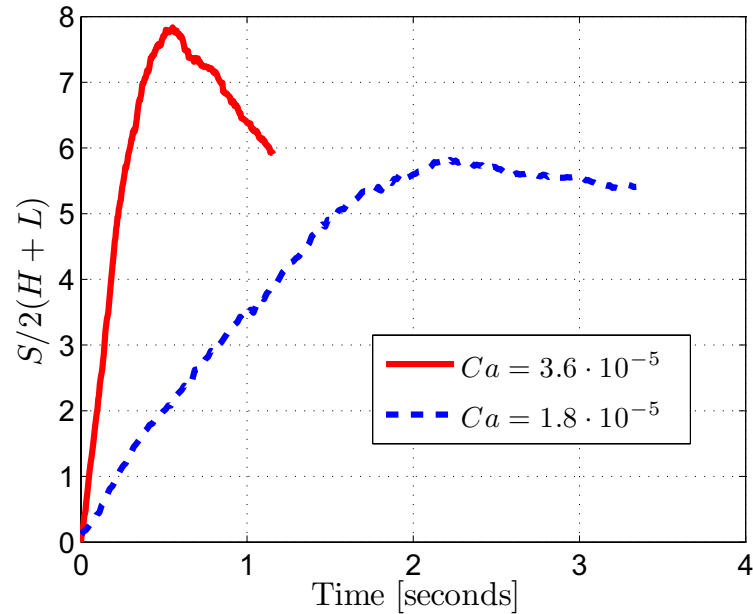


Figure 2.14. Nondimensional front length curves for the two viscous fingering flow regime experiments. These nondimensional front lengths curves were calculated from the time evolution images of air-water interface. Experiments were performed injecting air and displacing water ($M = 1.5 \times 10^{-2}$) at different injection flow rate of 0.5 and 0.228 ml s^{-1} which correspond to $Ca = 3.6 \times 10^{-5}$ and $Ca = 1.8 \times 10^{-5}$, respectively.

stops. The resulting flow patterns is characterized by the formation of multiple fingers of approximately the same size. In this set of experiments, the DM was originally saturated with water and air was injected to displace the water ($M = 1.5 \times 10^{-2}$). The flow rates used were 0.5 and 0.228 ml s^{-1} which results in a Ca of 3.6×10^{-5} and 1.8×10^{-5} , respectively. Images were collected using the CMOS camera at 500 fps for both flow rates. Three stages of the air percolation evolution for the two different injection flow rates are shown in Figure 2.13. These figures include the interface line between the injected and displaced fluids.

From the experiment images, the front length S and the wetted area A curves were calculated. The nondimensional front lengths curves, shown in Figure 2.14,

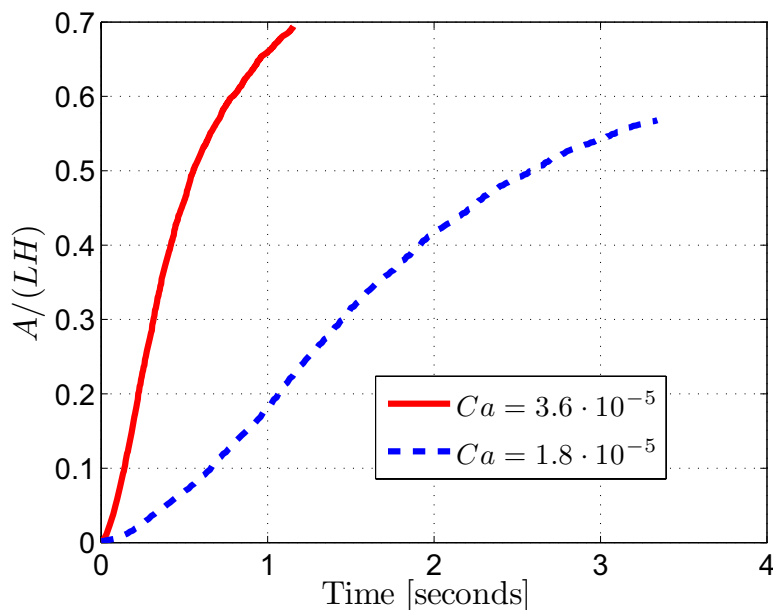


Figure 2.15. Nondimensional wetted area curves for the two viscous fingering flow regime experiments. These nondimensional wetted areas curves were calculated from the time evolution images of air-water interface. Experiments were performed injecting air and displacing water ($M = 1.5 \times 10^{-2}$) at different injection flow rate of 0.5 and 0.228 ml s^{-1} which correspond to $C_a = 3.6 \times 10^{-5}$ and $C_a = 1.8 \times 10^{-5}$, respectively.

have a maximum larger than one due to the presence of many fingers when compared with stable displacement and capillary fingering. For C_a of 3.6×10^{-5} the maximum S was 5.8 and for $C_a = 1.8 \times 10^{-5}$ the maximum S was 7.8. As the DM is filled, these fingers coalesce into wider conduits and the front lengths slowly decay over a period of time. However, the nondimensional wetted area curves are characterized by incomplete saturation of the media as shown in Figure 2.15.

During viscous fingering regime, the combination of the small pore size of the DM and the relative high viscosity of the water, as compared with air, displacement of the water requires high pressures which compresses the air inside the injection tubing. At the onset of percolation, the compressed air expands rapidly through the

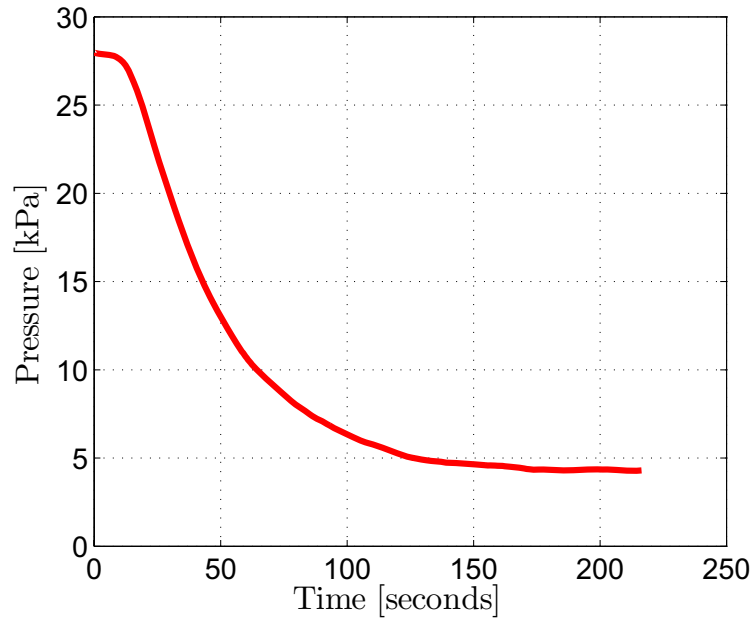


Figure 2.16. Percolation pressure curve for the viscous fingering flow regime experiment. Experiment was performed by injecting water and displacing SAE 30 motor oil ($M = 3 \times 10^{-3}$) at flow rate of 2.5×10^{-4} which correspond to $C_a = 2.4 \times 10^{-6}$.

DM originating a fast growth of the fingers. Subsequently, the growth speed of the fingers does not correspond to the injection flow rate. The percolation pressure curves include the rapid release of stored energy in the compressed air and this behavior does not correspond to drainage viscous fingering flow regime. Therefore, the air-water percolation pressure curves are not presented.

In order to avoid this problem and to keep a small viscosity ratio, an experiment using incompressible fluids was performed. In this experiment the DM was originally saturated with SAE 30 motor oil and it was displaced by injecting water (viscosity ratio of $M = 3 \times 10^{-3}$). The flow rate used in this experiment was $2.5 \times 10^{-4} \text{ ml s}^{-1}$ which results in a C_a of 2.4×10^{-6} . Due to the low contrast between the water and the oil in the DM, it was not possible to identify the fluid-fluid interface. Only the

pressure drop is presented, see Figure 2.16. When the water is injected and the oil displaced the overall viscous forces are reduced and therefore the pressure drop shows a gradual decay as the water is injected. When the fingers reach the edges the pressure levels off to the minimum value as was expected and the experiment ends.

2.4 Discussion

Previous publications on the study of the transport mechanisms of the water through the DM were focused on ex-situ experiments where the injected fluid is forced to cross the thickness of the DM for “through-plane” percolation. These ex-situ experiments are mimicking the operating conditions of a real fuel cell. In this work the fluid is injected on a small area on one side of the DM, forcing it to percolate along the DM for “in-plane” percolation.

The advantages of “in-plane” over “through-plane” is that the percolation occurs over a longer time which increases the experiment precision, especially in the measurement of the percolation pressure. While “in-plane” experiments tend to be more realistic to the fuel cell operating conditions, the “through-plane” has the advantages of higher visual area and longer experimental time which are essential for a more fundamental understanding of transport mechanisms.

Benzinger et al. [4] measured the pressure required for the water to cross along the DM. Based on their experiment, water will cross along the DM at approximately 5.3 kPa. This pressure value can be compared to the initial value in the pressure curves for capillary fingering regime (4.5 and 5.3 kPa) shown in Figure 2.12 (a) and (b). The data from Benzinger et al. [4] represents only one point of the characteristic

pressure for the capillary fingering flow region of the drainage phase diagram and cannot provide visual access to identify the fingering pattern.

Litster et al. [39] used an experimental setup where water with fluorescence dye was injected along the bottom surface generating a “through-plane” percolation. Under this arrangement, their experimental setup is a realistic approximation of the operating conditions of a fuel cell. However, the time and the space where the fingers take place are small and hard to characterize. In this setup it would be difficult to distinguish between the different drainage flow regimes.

2.4.1 Drainage flow regimes in DMs

All three flows patterns can occur during PEM fuel cell operation. Each flow pattern has its own characteristic. The most immediate and easy to discern characteristic is the pattern shape: uniform, a few narrow fingers, or multiple fingers. Associated with these shapes are the wetted area curves and the front length curves. Also, each flow pattern will have a unique percolation pressure and time scale which can vary from seconds for viscous fingering and stable displacement to hours for capillary fingering. All these characteristics combined together can be used to classify different diffusion media according to their susceptibility to each drainage flow pattern.

It is also important to identify which conditions will trigger each flow regime, especially capillary fingering and stable displacement. When the a particular flow regime in a porous media changes from capillary fingering to stable displacement the media will start to flood. The transition between stable displacement and viscous fingering will rarely occur in a fuel cell. Nevertheless, when there is pressure difference between the air channels (e.g. a water plug blocking the channel) and if this pressure

is higher than the capillary pressure then the reactants will displace the water in a viscous fingering mode. To understand when this condition can be triggered, a closer look of the morphology of each porous layer in a PEM fuel cell is required.

Assuming a typical fuel cell of 1 kW and 1 m² active area operating for one hour, 0.5 l of water will theoretically be produced [22]. The capillary number for this flow rate $q = 1.4 \times 10^{-7}$ ml s⁻¹ is approximately $C_a = 5 \times 10^{-9}$ which corresponds to the capillary fingering flow regime. However, in a typical fuel cell assembly, a microporous layer (MPL) is located between the catalyst layer and the gas diffusion media. The cathode and anode MPLs, with a typical pore size in the order of 100-500 nm, increase the capillary force up to approximately 100-1000 times when compared with the capillary force on DM. As a consequence of this high capillary pressure in the MPL, the catalyst layers and the PEM are forced to operate under complete saturation conditions, keeping them hydrated [52]. In contrast, the capillary number for anode and cathode DMs (with pore size in the order of 5-10 μ m) is lower resulting in a capillary fingering mode. This could be a desirable effect in the DM because during capillary fingering regime the fingers will allow the water reach the channel without flooding the DM.

2.5 Conclusions

An experimental setup was developed to have visual access of fuel cell Diffusion Media layer (DM) during percolation. The characteristic nondimensional numbers were varied in order to obtain the three different types of fluid flow behaviors specified in the drainage phase diagram. The nondimensional numbers were set by ad-

justing the injection flow rate as well as changing the working fluids. During the experiment, injection pressure was measured and the time-dependent water distribution was recorded. From the time dependent wetted area and front length as well as from the injection pressure it can be concluded that a change in the injection condition can completely change the water transport mechanism occurring in the DM. These changes can be associated with three different types of fluid flow behaviors, the stable displacement, the viscous fingering, and the capillary fingering. These three flow regimes summarize the expected transport mechanisms taking place in the DM during operation of fuel cells.

The results obtained in this work not only support but also bring together the transport mechanism based on the capillary phenomena described by Litster et al. [39] and the pressure readings obtained by Benzinger et al. [4]. This experimental setup can be further developed to be used as a standard for characterizing DM as well as studying degradation mechanisms, compression effect on the percolation, durability, etc.

This work shows the importance of drainage transport mechanisms which are crucial for developing a consistent model of the PEM fuel cell. These transport mechanisms are not accounted for in current transport models of PEM fuel cell, but they can result in considerable differences in estimated amounts and distributions of water in fuel cells. These transport mechanisms should be incorporated into models capable of capturing two phase flow and capillarity. Finally, the C_a -M phase diagram provides a fundamental resource for characterization of fuel cell diffusion media.

3. SCALING THE WATER PERCOLATION IN PEM FUEL CELL POROUS TRANSPORT LAYERS

A typical polymer electrolyte membrane (PEM) fuel cell consist of a series of non-wetting porous layers comprised between the bipolar plates: the anode and cathode porous transport layers (PTL), also known as gas diffusion layer, with their catalyst layer and the proton exchange membrane. The cathode PTL has the dual role of facilitating the access of the reactants to the catalyst layer while removing the generated water. In a PEM fuel cell under normal operating conditions, water percolates through the porous layers forming conduits or fingers which are influenced by the capillary pressure.

In this work, using a specially designed ex-situ experimental setup, images of the water percolation and the pressure required to inject the water in a PTL are simultaneously recorded. From the image post-processing analysis, the area covered by the water referred to as wetted area, is calculated. The time evolution of wetted

Note: This chapter is reprinted with permission from E. Médici and J. S. Allen, Scaling the Water Percolation in PEM Fuel Cell Porous Transport Layers, Proceedings of the Third International Conference on Porous Media and its Applications in Science, Engineering and Industry, June 2010, Montecatini, Italy. Copyright 2010, American Institute of Physics. Copyright agreement in Appendix B section 2.2.

area and the percolation pressure are indicative of the drainage flow pattern taking place.

Through a proper scaling of the problem, in addition of the capillary number and the viscosity ratio, a non-dimensional number was defined correlating the pressure-area data; two variables which are usually analyzed separately. Using this non-dimensional number a simple logarithmic dependence for all injection flow rates was obtained for a given PTL sample. When a PTL sample with different morphological and wetting properties was used, a new curve was obtained for all injection flow rates. Each curve has a unique slope and, based on preliminary results, that slope can be used to uniquely characterize a PTL. This non-dimensionalization can also be used as a validation method for numerical simulation of drainage in porous media.

3.1 Introduction

The process occurring when a non-wetting fluid is forced to displace a wetting fluid inside a porous media is called drainage. Depending on the fluid properties and flow rate three types of drainage flow patterns can occur: viscous fingering, capillary fingering, or stable displacement [35]. Viscous fingering occurs when the injected fluid has lower viscosity than the displaced fluid. This overall reduction in the viscous stress induces the pressure required to inject the non-wetting fluid, referred to as percolation pressure, gradually decays during the injection. This unstable situation originates the formation of multiple narrow conducts or finger that characterizes viscous fingering. In contrast, capillary fingering and stable displacement occurs when the injected fluid has higher viscosity than the displaced fluid. During capillary fingering, non-wetting

fluid percolates through the largest pores or the pore with lower wettability which results in a constant percolation pressure. The non-wetting fluid moves through these pores originating few fingers which are characteristic of capillary fingering. During stable displacement the percolation pressure is higher than the capillary pressure required to saturate the largest pores or the pore with higher wettability, consequently filling the surrounding smaller pores or the pores with lower wettability. As the non-wetting fluid is injected the overall viscous stress increases and the percolation pressure continuously increases as well. The resulting flow pattern is characterized by a regular shape that continuously grows as the non-wetting fluid is injected.

Two non-dimensional numbers have been used to scale drainage and identify which mechanisms are controlling the fluid flow and its corresponding flow pattern [35]. These non-dimensional numbers are the viscosity ratio (ratio between injected and displaced fluid viscosities) and the capillary number (ratio between viscous and capillary actions). Lenormand et al. [35] proposed a drainage phase diagram based on these two non-dimensional numbers summarizing the three drainage flow patterns. However, in this scaling analysis the effect of the porous media properties are not part of the formulation, therefore it can be used to characterize porous media. The two main porous media properties concerning drainage are the morphology and the wettability.

A PEM fuel cell consists of a series of non-wetting porous layers comprised between the bipolar plates: the anode and cathode porous transport layers with their catalyst layer and the proton exchange membrane. The cathode porous transport layer has the dual role of facilitating the access of the reactants to the catalyst layer while removing the generated water. Water percolation through the PTL will evolve on one of the drainage flow patterns, (either capillary fingering or stable displacement),

depending on the injection flow rate, which ultimately depends on the fuel cell current intensity. Problems arise at extreme operating conditions. At high current density, water generated begins to accumulate in the PTL blocking the access of the reactants, increasing the mass transport losses, and decreasing the fuel cell efficiency. At low current density demand, water generated is not enough to support the proton transport at the proton exchange membrane, decreasing the fuel cell efficiency as well. Therefore, water management in fuel cell is a critical issue, especially at high current density.

There has been an increasing effort to characterize the water percolation through the PTL. Capillary pressure [7, 8, 13, 14, 17, 18], contact angle, and the Leverett function [26–29] have been measured for a variety of PTLs and conditions. Even though these tests provide insight and a resource for modeling, the data is not able to fully characterize a PTL with respect to drainage.

In this work a new scaling for drainage in porous media is proposed where porous media morphology and wettability effects are implicitly included. This new scaling allows for characterization of PTLs from a drainage perspective but also as a validation technique for numerical simulations.

3.2 Experimental Setup

The experimental setup used is the same described by Medici and Allen [43]. In that work, results from a series of drainage test performed on a Toray T060 PTL using a pseudo Hele-Shaw experiment were reported, see Figure 3.1. The existence of the three flow patterns in PTLs was demonstrated. However, due to the qualitative nature

of the phase drainage diagram, it is not suitable for PTL characterization. Different PTL samples from different manufactures will have similar drainage phase diagram regardless that the capillary pressure and the saturation curves may vary significantly. This is because the porous media properties are not part of the formulation, only the fluid flow properties are considered. The scaling presented herein enables the drainage phase diagram to be collapsed into a single curve which incorporates the capillary pressure, referred to hereafter as percolation pressure, and the saturation curves, referred to hereafter as wetted area. The PTL samples are fibrous porous material made out of carbon fibers and coated with polytetrafluoroethylene (PTFE) which makes the material non-wetting for water (hydrophobic), see Figure 3.2. The bottom side has been coated with a fine layer of carbon particles coated with PTFE (not shown in the figure) usually called microporous layer (MPL). A small perforation (1mm in radius) is made in the middle of the sample to avoid the excess pressure drop associated with the microporous layer [15]. Four PTL samples of 5 cm diameter and 250 μm thick were tested in the pseudo Hele-Shaw experimental setup. Two of the samples are Toray T060 with only one having an MPL. The other two PTL samples are from different manufacturers having completely different pore size structure and include an MPL.

The PTL samples were compressed between two layers of PDMS. The PDMS layers seal the top and bottom faces of the PTL while providing visual access. The compression pressure was 24 kPa which produces a negligible strain on the PTL [31]. The lateral sides are open to the atmosphere allowing the wetting fluid, in this case air, to be drained. The non-wetting fluid, in this case water, is injected at the center of the sample using a syringe pump. The experiment ends when the water reaches the edge of the PTL sample. A pressure transducer located in the injection tubing

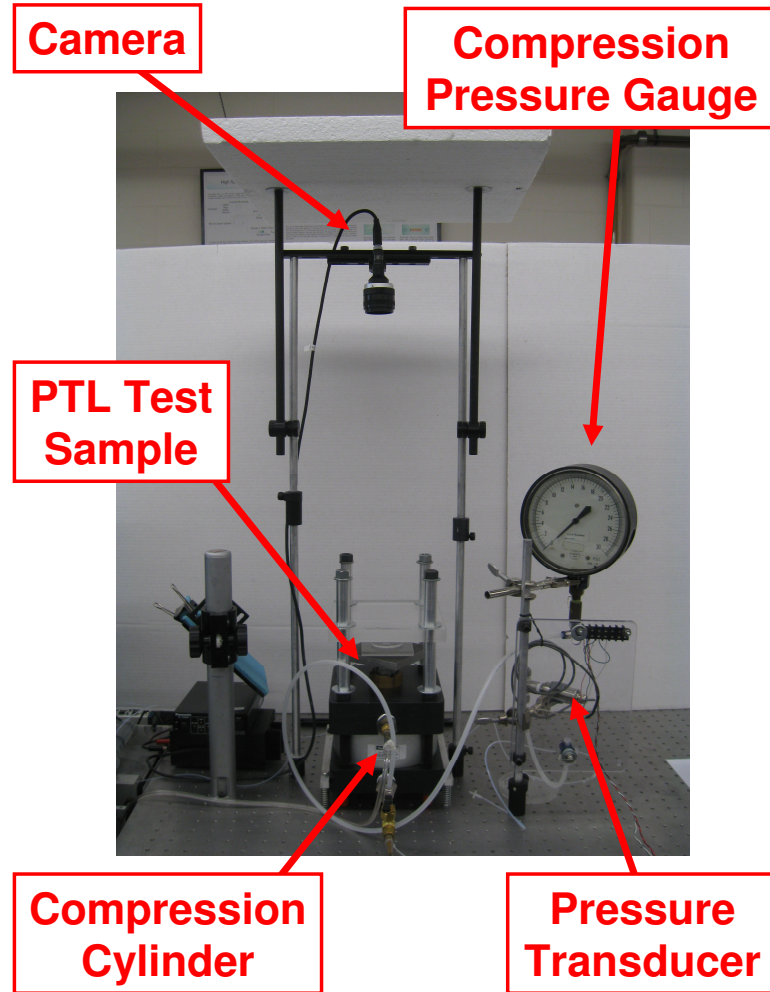


Figure 3.1. Experimental setup.

measures the percolation pressure. The pressure transducer data was recorded at different sampling rates depending on the injection flow rate.

Water visualization in PTLs has been always an issue. Many techniques have been developed for that purpose [2]. For the results presented herein, optical videography was used to visualize the water percolation. Two types of cameras were used depending on the experimental conditions. A CCD camera was used for the capillary fingering experiment where the experiment duration can be on the order of hours. A

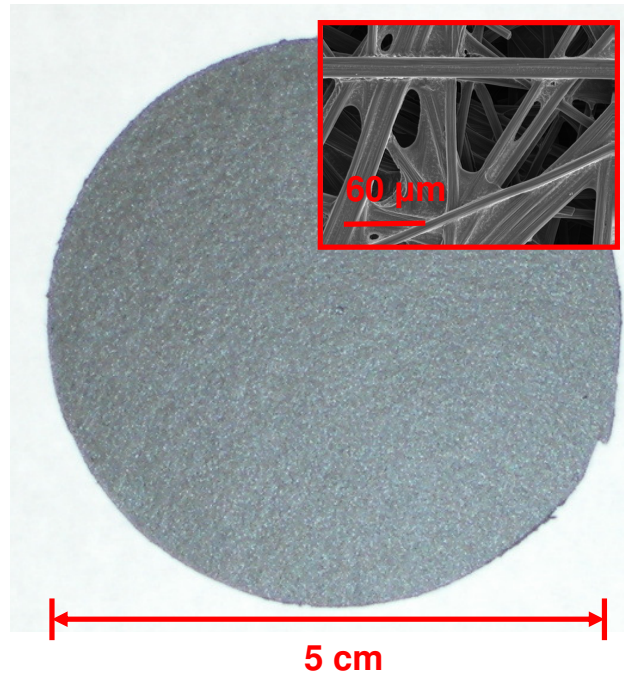


Figure 3.2. PTL sample used in the pseudo Hele-Shaw experiment. Top corner: SEM image at 500x of the Toray T060 PTL sample.

CMOS camera was used for the stable displacement where the experiment duration can be on the order of seconds.

Five different flow rates were used for each PTL sample as summarized in Table 3.1. The injection flow rate was varied to obtain the stable displacement and capillary fingering flow patterns. Viscous fingering is not included in the analysis of this work. The PTL samples were placed for 48 hours in a desiccator prior to any experiment to remove any residual water content. The presence of water in the porous structure can facilitate the water percolation by reducing the percolation resistance which translates in a lower percolation pressure.

A reference capillary number, C_a , was calculated based on the inlet condition and

Table 3.1. Experiment settings.

	Flow Rate [cm ³ s ⁻¹]	Ca [†]	Imaging Camera	Pressure [fps]	Sampling [Hz]
1	6.0×10^{-6}	3.1×10^{-8}	CCD	0.016	0.1
2	2.15×10^{-5}	1.2×10^{-7}	CCD	0.333	5
3	3.2×10^{-4}	1.6×10^{-6}	CCD	2.4	100
4	4.9×10^{-3}	2.5×10^{-5}	CCD	9	200
5	9.15×10^{-2}	4.7×10^{-4}	CMOS	125	2000

[†] Calculated at in the inlet.

it is defined by:

$$C_a = \frac{Q\mu_{nw}}{\sigma\pi r_i^2} \quad (3.1)$$

where Q is the flow rate, μ_{nw} is the non-wetting fluid (water) viscosity, σ is the surface tension and r_i is the inlet tube radius. Because the experiments are performed at a constant flow rate, the reference capillary number is a constant value that depend only in the injection flow rate. The viscosity ratio, M , is defined as the ratio between the non-wetting and wetting fluid viscosities:

$$M = \frac{\mu_{nw}}{\mu_w} \quad (3.2)$$

For water and air as working fluids the viscosity ratio is approximately 64.

Percolation pressure and images were recorded simultaneously. The water distribution was extracted from each image/frame for every experiment. The projected area covered by the water from a top view was calculated and will be referred to as wetted area, A . The procedure to calculate the wetted area is the same as described by Medici and Allen [43].

The flow regime, stable displacement and capillary fingering, are identified by analyzing the percolation pressure and the wetted area. During capillary fingering water

spread unevenly forming few fingers along the PTL at an approximately constant percolation pressure. In stable displacement, however, water spreads evenly around the injection point. As the water is injected, the percolation pressure gradually grows to compensate for the viscous losses that are proportional to the perimeter of the advancing front. Normally, only one of these measurements, pressure or area, is used to recognize the fluid pattern. In this work, both measurements are combined into one parameter through scaling of energies.

3.3 Results and Discussions

3.3.1 The scaling

The scaling proposed in this work is based on the ratio between the input energy and the dissipated energy. The input energy is proportional to PQ where P is the pressure gradient along the domain and Q is the injection flow rate. The dissipated energy is proportional to $Q^2\mu l/h^4$ where l is the largest length scale, μ is the viscosity, and h is the smallest length scale. A dimensionless energy ratio is defined as C_e :

$$C_e = \frac{Ph^4}{Q\mu l} \quad (3.3)$$

When two fluids are present, for example in the flow between two parallel plates, while one fluid is injected and the other displaced, the large length scale l has to be modified according as the non-wetting fluid is injected. This type of arrangement is usually refer to as a Hele-Shaw cell. If the plates are non-wetting to the injected fluid the resulting flow pattern is drainage. However, if the plates are wetting to the

injected fluid the resulting flow pattern is imbibition.

The correction for the increase in length and width is based on temporal evolution of the wetted area A :

$$C_e = \frac{Ph^3 A}{Q\mu l^2} \quad (3.4)$$

The advantage of this new scaling, as presented in equation (3.4) is that it combines two variables, percolation pressure P , and wetted area, A , that usually are treated separately. For example, the drainage phase diagram is based only on observations of the wetted area. C_e defined by equation (3.4) is a measure of the input energy dissipated due to viscous stresses and energy used to generate interfacial area.

The time is non-dimensionalized by the flow rate over the large length scale cubed and by the inverse of the capillary number:

$$t^* = t \frac{\sigma h^2}{l^3 \mu} \quad (3.5)$$

The transition between stable displacement and capillary fingering occurs at $t^* \sim 1$ when the capillary effect is in the same order of magnitude as the viscous effect.

3.3.2 Radial Flow Between Parallel Plates

A relationship for the variation of pressure versus time and wetted area versus time can be found analytically for a radial flow between two parallel plates, as shown in Figure 3.3. For a constant injection flow rate, the variation in radial growth in time can be expressed as:

$$R = \sqrt{\frac{Qt}{2\pi h} + R_i^2} \quad (3.6)$$

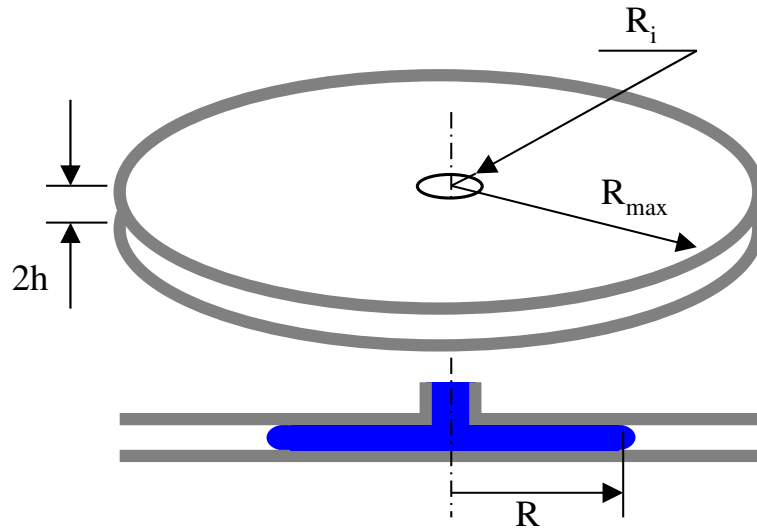


Figure 3.3. Radial flow between two parallel plates.

where Q is the injection flow rate, R_i is the radius of the injection hole or inner radius, and h is half of the gap between the plates. The wetted area can be written in terms of the radial growth as:

$$A = \pi R^2 \quad (3.7)$$

The pressure gradient in the injected fluid, ΔP , can be expressed as the difference between injection pressure and the capillary pressure:

$$\Delta P = P - \sigma \left(\frac{1}{R} - \frac{\cos \theta}{h} \right) \quad (3.8)$$

During drainage, the contact angle θ is assumed to be higher than 90° . Solving the Navier-Stoke equation for radial flow between two parallel plates [45], the pressure gradient is:

$$\Delta P = -\frac{3\mu Q}{4\pi h^3} \ln \frac{R_i}{R} \quad (3.9)$$

where μ is the viscosity of the injected fluid. Substituting the pressure gradient of equation (3.8) into equation (3.9) and solving for P neglecting the radial curvature on the capillary pressure:

$$P = -\sigma \frac{\cos \theta}{h} - \frac{3 \mu Q}{4 \pi h^3} \ln \frac{R_i}{R} \quad (3.10)$$

Substituting wetted area and the injection pressure from equation (3.10) into equation (3.4), the C_e for radial flow became:

$$C_e = -2\pi \frac{\sigma h^3}{\mu Q} \frac{R^2}{R_{\max}^2} \frac{\cos \theta}{h} - \frac{3}{2} \frac{R^2}{R_{\max}^2} \ln \frac{R_i}{R} \quad (3.11)$$

and the non-dimensional time became:

$$t^* = t \frac{\sigma h^2}{2\mu R_{\max}^3} \quad (3.12)$$

where R_{\max} is the outer radius of the parallel plates. Based on the assumption presented in this formulation, the fluids front interface will grow radially in time like in stable displacement flow regime independently of the injection flow rate. It is known that for low flow rates, small imperfection in the plates alignment or roughness can trigger asymmetric fluids front interface corresponding to capillary fingering. However, this instability is not accounted for in the axisymmetric formulation. The pressure gradient and the wetted area presented here are still valid under that condition. The length of the interface between both fluids won't be $2\pi R$ anymore, as in pure radial growth, but this quantity is never used in the scaling.

Consider the case of study of water displacing air. Let's assume two parallel plates separated 0.025 cm, inner radius of 0.1 cm, external radius of 5 cm, and contact

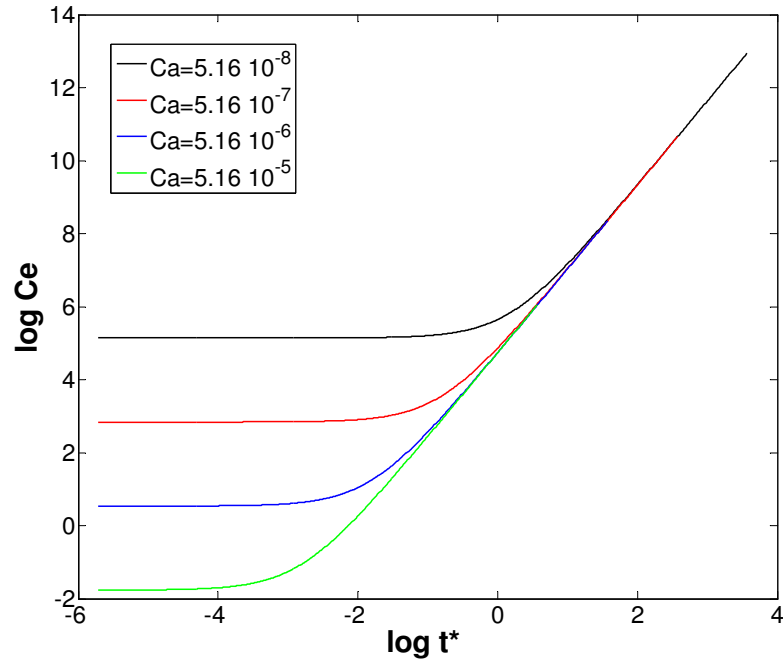


Figure 3.4. C_e versus non-dimensional time for different reference capillary numbers for a radial flow between two non-wetting parallel plates .

angle of 135 degrees. The water surface tension is 0.069 N/m and the water and air viscosities are 1.0×10^{-3} and 1.5×10^{-5} Ns/m² respectively. Injection flow rates of 1.0×10^{-5} , 1.0×10^{-4} , 1.010^{-3} , and 1.0×10^{-2} cm³/s are used. This flow rates correspond to reference capillary numbers of 5.16×10^{-5} , 5.16×10^{-4} , 5.16×10^{-3} , and 5.16×10^{-2} respectively, calculated based on the inlet condition using equation (3.1).

The C_e versus the non-dimensional time for the different reference capillary numbers, is plotted in a logarithmic scale in Figure 3.4. All these curves can analyzed in two parts, an initial transient time followed by a steady gradual growth. The initial transient time, it is very small in time when compared with the total time required for the injected liquid to reach the edge of the plates at R_{\max} for all the flow rates analyzed. This initial time is less than 1% of the total time. At the steady grad-

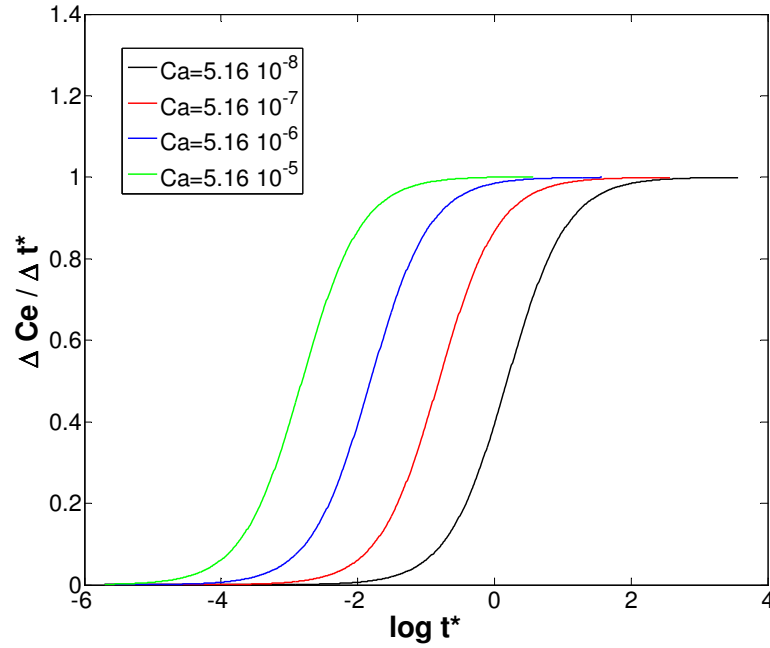


Figure 3.5. Slope of the C_e versus non-dimensional time for the different reference capillary numbers.

ual growth all the curves for different flow rates collapse into a single curve. This is indicative that the same level of dissipation can be obtained with two different flow rates but with different level saturation. The reduction in the flow velocity, and therefore in the dissipation due to the viscous stresses, can be compensated with a large wetted area.

The slope in the C_e versus t^* is calculated by $\Delta C_e / \Delta t^*$ and plotted in Figure 3.5. The slope of the C_e versus t^* curves change from 0 to 1 during the transition period for every curve until it reaches a plateau equal to 1 for the gradual growth period. This fact confirms that the solution for every flow rate is the same after the transition period. A slope of 1 on the logarithmic scale implies a linear relationship between the C_e and t^* as well.

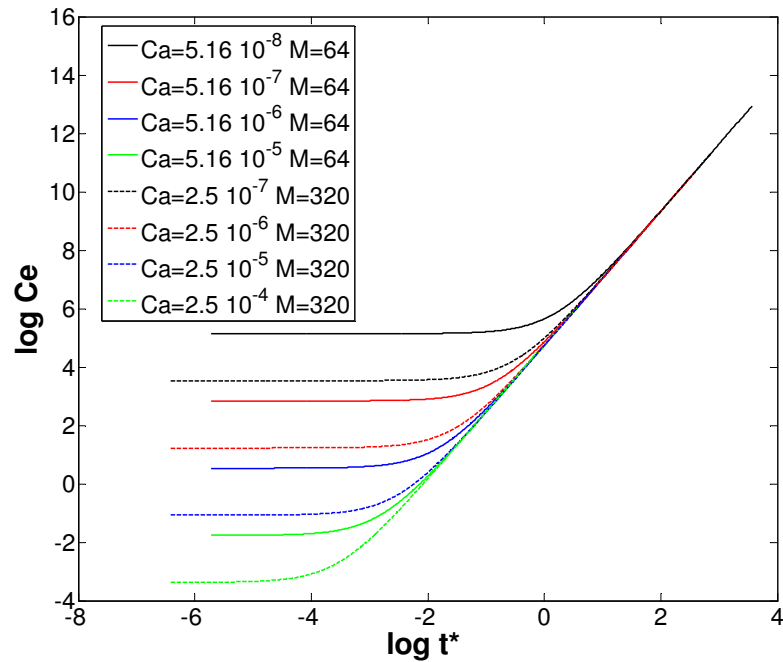


Figure 3.6. Effect of the viscosity ratio on the C_e versus non-dimensional time for different reference capillary numbers.

The effect of the a different working fluids is analyzed by changing the fluid viscosity. Normally, changing the working fluid will change the surface tension as well. However, the surface tension and the contact angle acts together and a change in one can be compensated with a change in the other one. Therefore, only the effect of the viscosity is analyzed. The viscosity of the injected fluid was changed from 1.0×10^{-3} to 5.0×10^{-3} Ns/m². giving viscosity ratio of 64 to 320, respectively, for the same injection flow rates used previously. No change is observed on gradual growth region of the C_e versus t^* curves as shown in Figure 3.6. The effect of an increase in the viscosity ratio is a reduction on the initial values of the C_e (increase of the dissipated energy).

In the case of the wetting plates to the injected fluid, or imbibition, the injected

fluid penetrates freely through the gap between the plates driven by the capillary pressure. During imbibition, the contact angle θ is assumed to be lower than 90° . The pressure gradient is now:

$$\Delta P = -\sigma \left(\frac{1}{R} - \frac{\cos \theta}{h} \right) \quad (3.13)$$

Following a similar procedure for non-wetting plates to the injected fluid, as described by Middleman [45], and solving for the radial growth in time instead of the pressure gradient and neglecting the radial curvature on the capillary pressure:

$$t \frac{4\sigma \cos \theta}{3\mu h} \left(\frac{h}{R_i} \right)^2 = \left[\left(\frac{R}{R_i} \right)^2 \ln \left(\frac{R}{R_i} \right)^2 - \left(\frac{R}{R_i} \right)^2 + 1 \right] \quad (3.14)$$

the C_e becomes:

$$C_e = 2\pi \frac{\sigma h^3}{\mu Q} \frac{R^2}{R_{\max}^2} \frac{\cos \theta}{h} \quad (3.15)$$

and the non-dimensional time becomes:

$$t^* = \frac{3}{8} \frac{h}{\cos \theta} \frac{R_i^2}{R_{\max}^3} \left[\left(\frac{R}{R_i} \right)^2 \ln \left(\frac{R}{R_i} \right)^2 - \left(\frac{R}{R_i} \right)^2 + 1 \right] \quad (3.16)$$

Consider again the case of water displacing air as a case of study with the same plates sizes and working fluid properties as in the non-wetting case. The new contact angle used is 45 degrees which gives the same capillary pressure as in the non-wetting case but acting in the opposite direction.

Plotting the C_e versus t^* for the wetting case together with the non-wetting case, after an initial transient time, a gradual growth period with the same slope than in the non-wetting case was found, see Figure 3.7.

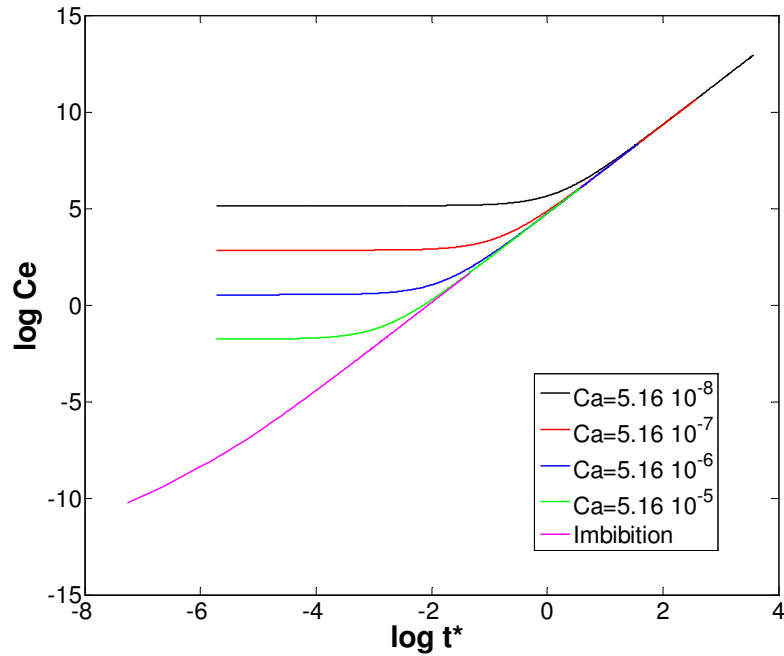


Figure 3.7. Effect of the viscosity ratio on the C_e versus non-dimensional time for different reference capillary numbers.

3.3.3 Scaling Drainage in Thin Porous Media

When the empty space between the two parallel plates is filled with a porous material, C_e will vary depending on the pore size distribution. This type of arrangement is referred to as a pseudo Hele-Shaw cell.

The typical capillary fingering and stable displacement pattern from a PTL can be seen in Figure 3.8 and 3.9, respectively for a Toray T060 PTL. The wetted area for each experiment is plotted in Figure 3.10. There is a large variation in experiment duration, from seconds for the stable displacement to hours for capillary fingering. For this reason time is plotted on a logarithm scale. The amount of water at the end of the experiment was also different between capillary fingering and stable displacement

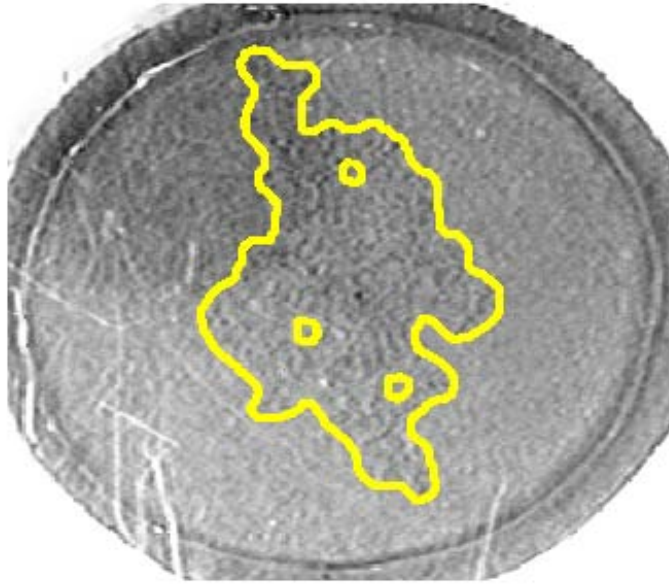


Figure 3.8. Typical water distribution for capillary fingering flow regime, $C_a = 3.1 \times 10^{-8}$. This image was taken after 7140 seconds on experiment 1. The yellow line identifies the interface between the water and air.

varying from a minimum of 1 cm^2 up to 13 cm^2 , respectively as measured through the wetted area.

The percolation pressure for each flow rate is plotted in Figure 3.11 with its associated reference capillary number. The percolation pressure remains the same at approximately 10 kPa , independent of the flow rate while in capillary fingering regime ($C_a = 3.1 \times 10^{-8}$ and $C_a = 1.2 \times 10^{-7}$). The percolation pressure has a short transient increase that levels off to a constant pressure. The leveling is the result of the water percolation through a low pressure path (pores with larger size and/or lower wettability). Under stable displacement conditions, however the percolation pressure increases gradually in time, reaching a maximum of 40 kPa . The percolation pressure increases proportional to the flow rate.

The C_e , as defined by equation (3.4), is plotted in Figure 3.12 against the non-

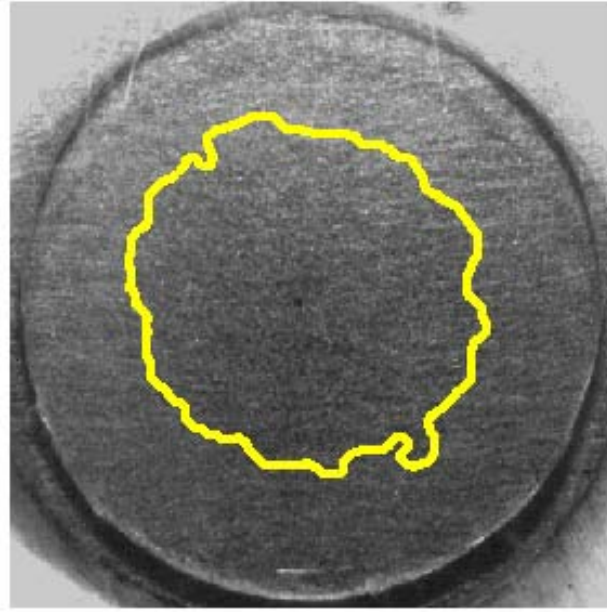


Figure 3.9. Typical water distribution for stable displacement flow regime, $C_a = 4.7 \times 10^{-4}$. This image was taken after 2.3 seconds on experiment 5. The yellow line identifies the interface between the water and air.

dimensional time, as defined by equation (3.5) for the PTL sample corresponding to Toray T060 with MPL. In this case l is the PTL radius, 2.5 cm; h is the PTL thickness, 250 μm , μ is the water viscosity, 0.001 Nm^{-2}s ; and σ is the water surface tension, 0.069 Nm^{-1} .

In the case of the smallest length scale h , the average pore size could be used as another reference scale. However, for the PTL samples analyzed in this work the average pore size is similar consequently using the thickness or the average pores size will have a similar effect on the scaling. An important parameter to determine with precision is the onset of percolation. In this case it was considered that $t = 0$ happened when a small quantity of water was noticed around the injection hole. To focus only on the drainage behavior, the first and last stages of the water percolation are truncated from the C_e versus t^* plot to eliminate the transition time described

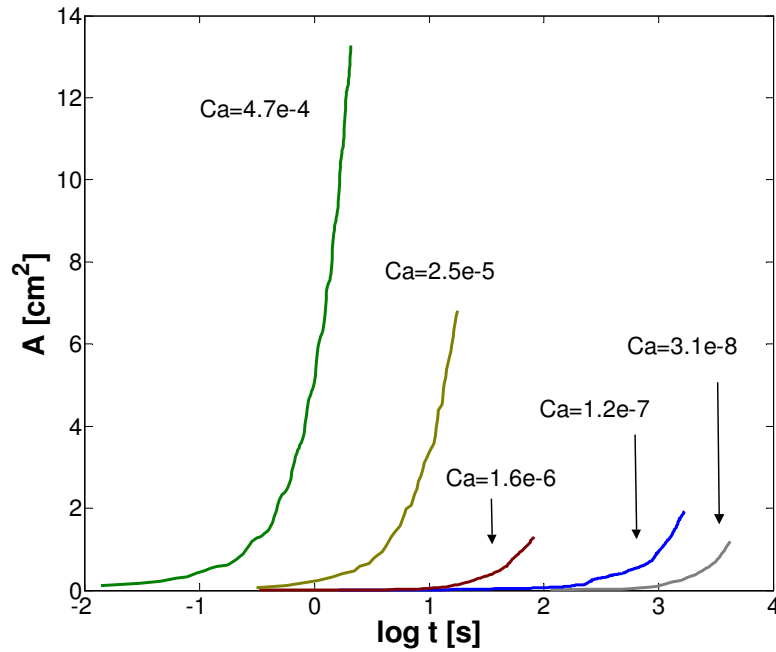


Figure 3.10. Toray T060 wetted area, A , for obtained for each experiment. Far left curve corresponds to stable displacement while the far right curve corresponds to capillary fingering.

in the analytical solution for radial flow between two parallel plates and boundary effects once the water reaches the edge of the sample.

C_e decreases as the flow rate increases and the pattern changes from capillary fingering to stable displacement indicating that more energy is dissipated in stable displacement than in capillary fingering. There are two dissipation mechanism involved in drainage in porous media, the viscous stress and the moving contact line. For stable displacement at a very high flow rates, a great portion of the input energy is dissipated due the effect of the viscous stresses. For capillary fingering, as the flow rate is reduced the input energy remains the same (proportional to the percolation pressure which is constant) while the dissipated energy is reduced (proportional to the flow rate). Consequently, the C_e curve gradually grows as a function of the

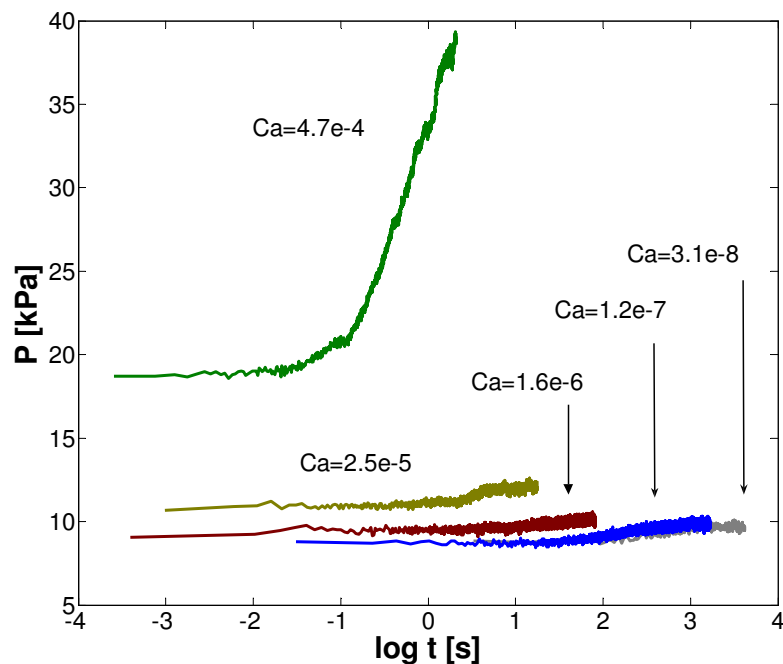


Figure 3.11. Toray T060 percolation pressure, P , curves for each experiment. Top curve correspond to stable displacement while bottom curve corresponds to capillary fingering.

non-dimensional time.

3.3.4 PTL Characterization

Except for one of the Toray PTL sample, every PTL sample has an MPL. As it was mentioned before, a hole was punched in the middle to avoid any over pressure due to the microporous layer. The C_e corresponding to both Toray PTLs are plotted in Figure 3.13. Good alignment was obtained when comparing both PTL samples indicating that the hole was sufficient to avoid any effect from the MPL as well as good repeatability among experiments with the same reference capillary number.

A linear regression approximation was calculated for both the series of experiments

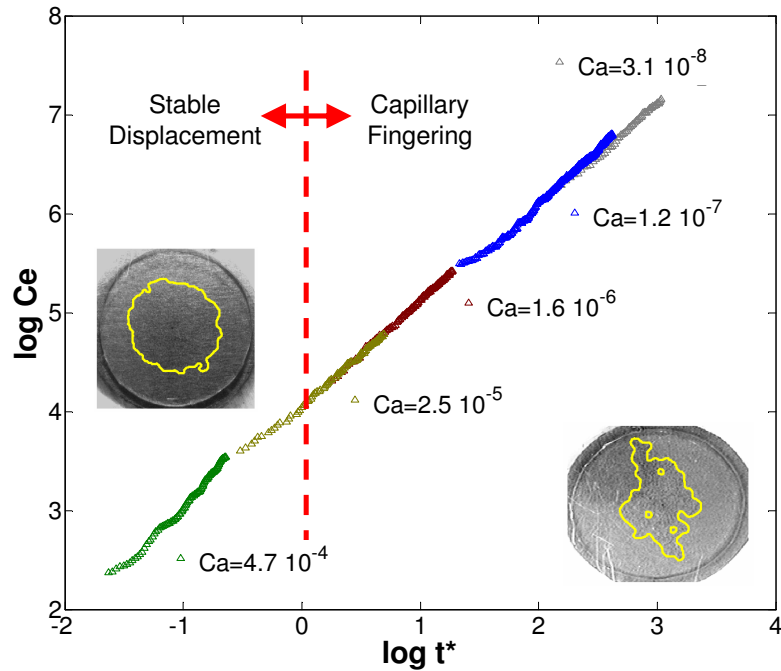


Figure 3.12. Toray T060 C_e versus non-dimensional time curves for each flow rate used and its associated reference capillary number.

corresponding to both Toray PTLs on the logarithmic scale. The linear regression has the form of $\log C_e = b \log t^* + a$. In both cases the coefficient a of approximately 4.08 and a coefficient b of approximately 1 were obtained. A coefficient b equal to 1 is in good agreement with the analytical solution for a radial flow between two parallel plates. The value of a around 4.08 is the C_e value at which the transition between capillary and stable displacement occur at $t^* = 1$. The difference between the coefficients a for both Toray PTL is less than 0.1%.

The C_e versus t^* for the other two PTL samples are also plotted in Figure 3.13. A linear regression was also calculated for every PTL sample tested and coefficients of the linear regression are summarized in Table 3.2. Again the b obtained is approximately one for every case confirming the that C_e versus t^* is linear in both log-log

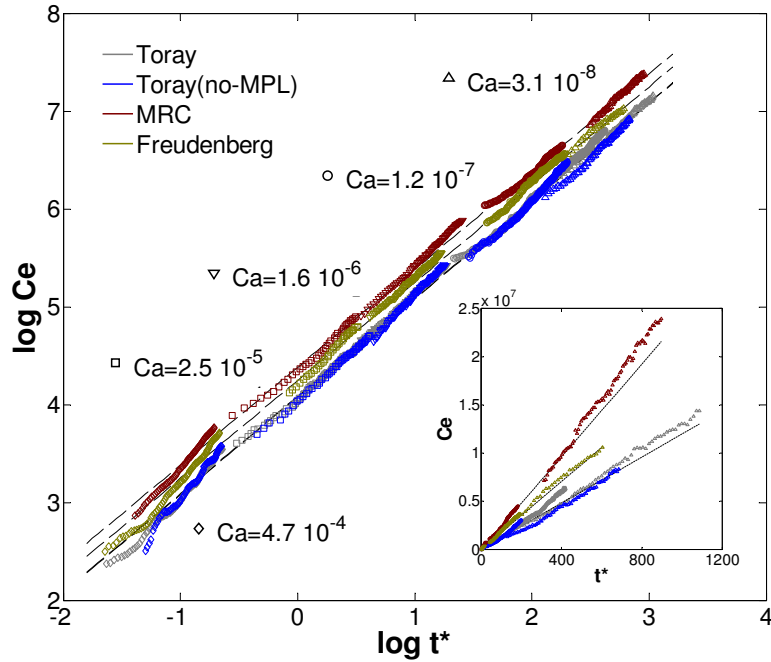


Figure 3.13. C_e versus non-dimensional time curves for each PTL sample.

and linear scales, at least for the conditions and porous media presented in this work. In contrast, the difference in the coefficient a is significantly large between the PTLs, from 4.08 to 4.38 suggesting that transition between stable displacement and capillary fingering will occur at different condition in each PTL. The coefficient represents also the offset between the linear regression curves in the logarithmic scale plot while the 10^a represents the slope of the linear regression in the linear scale as shown in the

Table 3.2. Linear regression coefficients for $\log C_e = b \log t^* + a$ fit to experimental data.

PTL sample	a	b	10^a	R^2
Toray with MPL	4.078	1.022	11980	0.9989
Toray with no MPL	4.081	1.003	12073	0.995
MRC	4.381	1.008	24047	0.9988
Freudenberg	4.247	1.017	17667	0.9986

plot inset in Figure 3.13. This change in slope can be potentially used to characterize PTL base on its drainage behavior.

3.4 Conclusions

A series of experiments on water percolation on fuel cell porous transport layers were conducted in which, the wetted area and the percolation pressure were measured. These two measurements were combined in to a single variable by defining a new scaling for drainage in porous media based on the ratio of injected and dissipated energies called C_e . This new variable, when plotted against the non-dimensional time provides a tool to identify the transition between stable displacement and capillary fingering. Different PTL samples has been tested and a significant change in the slope of the fitting curve of the C_e versus t^* were obtained for every sample, which makes this scaling susceptible for PTL characterization, Moreover, this criterion can be extended to characterize porous materials other than PTLs.

4. THE EFFECTS OF MORPHOLOGICAL AND WETTING PROPERTIES OF POROUS TRANSPORT LAYERS ON WATER MOVEMENT IN PEM FUEL CELLS

A parametric study of the effect of wetting and morphological properties of the cathode porous transport layer (PTL), also known as the gas diffusion layer (GDL), on water transport in proton exchange membrane (PEM) has been conducted using a two-dimensional network model that captures the two-phase capillary flow behavior. The effect of PTL wetting properties is explored by considering four contact angle values. The effect of the morphology is analyzed using six pore size distributions. These six pore size distributions are generated by varying the scale and shape parameters in Weibull probability distribution functions. Also, the effect of a microporous layer (MPL) on water transport in the PTL is considered. Inclusion of the MPL resulted in a significant increase in the percolation pressure and a reduction in the PTL water content due to the formation of a few localized fingers which serve as water conduits.

Note: Reproduced by permission of ECS – Electrochemical Society. Article: E. Medici and J. S. Allen, The effects of morphological and wetting properties of porous transport layers on water movement in PEM fuel cells, *Journal of Electrochemical Society*, 157/10, Copyright 2010. Copyright agreement in Appendix B section 2.3.

When defects in the MPL were considered, the PTL water content remained low with percolation pressures reduced to values similar to a PTL without an MPL.

4.1 Water Transport in PEM Fuel Cells

Effective water management is critical to the performance and durability of a proton exchange membrane (PEM) fuel cell. Operation at conditions too dry or too wet can result in poor performance and significantly reduced operational life. A more thorough understanding of liquid water transport within the porous transport layer (PTL), also known as the gas diffusion layer, is necessary to develop components and operational strategies that result in improved fuel cell durability.

Modeling two-phase flow in the PTL is typically accomplished using effective permeabilities, effective diffusivities, and capillary pressure-saturation relationships. Although the effective permeability and diffusivity can be easily approximated using empirical correlations, the capillary vs saturation relationship is difficult to approximate [46]. A relationship between capillary pressure and PTL saturation can be obtained using various porosimetry techniques [6–8, 13, 15, 17]. Another method of modeling the effects of capillary pressure on water transport in the PTL is through the implementation of the J-Leverett function [36], which is an experimental correlation of injection pressure and saturation using concepts of porosity and permeability [26–29].

When using the J-Leverett function to correlate saturation to pressure, the flow resistance is handled through a Darcy-type relationship, where effective permeability is used to modify the area available for gas transport. Recent research has shown that

the distribution of liquid water within the PTL is not uniform [39, 43]. The primary cause of this uneven distribution is the capillary force that destabilizes the liquid-gas interface resulting in a flow pattern called capillary fingering [35, 43].

Full saturation is never obtained when capillary fingering is occurring. Water moves through a subset of pores, typically the largest and/or the most wetting pores, at approximately constant capillary pressure independent of the saturation level. As such, the pore size distribution has a more significant meaning in describing the PTL water transport than does the porosity or permeability. Because the liquid water distribution is uneven, the traditional continuum Darcy flow commonly used in porous media flows is not appropriate. To study the water percolation within a PTL, the pore-level capillary pressure must be included.

A network model is often utilized when pore-level dynamics are important to liquid transport in a porous medium. The network model has been proven to accurately simulate two-phase capillary flow in porous media [35, 61]. Weber et al. [62] suggested that the network model could account for the pore-level dynamics in a PTL. Simulations using the network model have demonstrated two-phase capillary flow through a PTL [55, 56]. The network model has also been used to calculate the effective permeability, diffusivity and capillary pressure curves of a PTL [14, 33, 41] which could then be incorporated into a system-level fuel cell model. These effective PTL properties are difficult to determine experimentally due to the nonuniform flow distribution resulting from capillary fingering. Network models have been experimentally validated using carefully designed water drainage experiments on porous layers similar to PTLs [3, 5].

The liquid pressure which results in capillary fingering is referred to as the capillary pressure and is affected by two properties of the PTL; the morphology (pore size

distribution) and the wettability (static contact angle). Changes to the wettability and morphology of the PTL affect the performance of PEM fuel cells [40, 64], though no consistent correlation between fuel cell performance and PTL morphology has been found.

The PTL morphology change which has received the greatest attention has been the addition of a microporous layer (MPL). The addition of an MPL, a fine porous layer made of poly(tetrafluoroethylene) (PTFE)-coated carbon particles, between the PTL and the catalyst layer has been shown to significantly improve fuel cell performance, though the actual function of the MPL has not been definitively established. Several modeling attempts have been proposed to explain the reason for fuel cell performance improvement due to the addition of the MPL and nearly all have concluded that the presence of an MPL reduces the liquid water content of the PTL. Nam and Kaviani [46] presented a model of water percolation through the PTL with an MPL. According to their one-dimensional model, the addition of an MPL increases the fuel cell performance due to better water management through a reduced PTL saturation. Later, Weber and Newman [63] presented a more sophisticated one-dimensional model of a fuel cell having MPLs on the cathode and anode sides. Their premise is that the MPL blocks water percolating from the catalyst layer to the PTL thereby decreasing reactant transport resistance and maintaining a more uniform hydration in the membrane. In addition, the MPL provides better catalyst support, reducing contact resistance and increasing the catalyst layer active area. The combination of these factors is thought to attenuate the degradation mechanisms, as observed by Kundu et al. [30]. The presence of an MPL was also found to mitigate performance loss due to changes in PTL wettability [53]. Qi and Kaufman [52] found that, having an MPL, increasing the PTFE content on the PTL had a negligible effect on fuel cell

performance.

Gostick et al. [16] measured the capillary pressure as a function of saturation in a PTL with an MPL. The capillary pressure in the MPL was found to be much higher than in the PTL. The high capillary pressure significantly reduced the PTL water saturation when the MPL was located between the PTL and the catalyst layer. Full PTL saturation could not be obtained due to the high capillary pressure which precludes the water entering the smallest pores of the MPL. Water crossed the MPL through its largest pores, generating localized fingering instabilities in the PTL. The suggestion is that a reduced PTL water content facilitates water removal from the catalysts layer and increases the gas permeability.

Extrapolating from these observations, Gostick et al. [16] suggested that properly located cracks or perforations in the MPL may improve the fuel cell performance at high current density. Improved fuel cell operation, as measured by polarization curves, has been reported for perforated PTLs [11, 65]. Owejan et al.[49] reported that the presence of cracks in the MPL reduces the pressure required to transport liquid water across the MPL, which may improve fuel cell performance. They suggested that water moved through the MPL in a vapor state. Hartnig et al. [20] using high resolution synchrotron X-ray radiography studied the water transport in a PEM fuel cell with an MPL. According to their observations, they also suggested that the liquid water from the catalyst layer crosses the MPL in a vapor state to later condense in the PTL. This interpretation is based on the combination of temperature and high capillary pressure. However, the premise that high capillary pressure requires water to move through the MPL in a vapor state may not be entirely valid.

In this work, the results of a parametric study using a network model to explore liquid water transport in the PTL are reported. The model is based on local pore

dynamics and, as such, does not require any external measurement of the capillary pressure as a function of saturation. The pore size distribution used as a reference model was obtained from the mercury intrusion porosimetry data [14], but the distribution could be obtained from other techniques [59]. The stochastic nature of the pore size distribution is taken into consideration by generating multiple PTL structures using the same pore size distribution with randomized pore arrangements. The objective of this parametric study was to investigate the role of PTL wettability and morphology on water transport. The effect on transport due to the addition of an MPL was also studied. The MPL was modeled both as having a unimodal fine pore size distribution and as having defects, or cracks.

4.2 Simulation of Water Transport in the PTL

Water transport in the PTL is simulated using a network model that consists of a regular lattice of cylindrical tubes of constant length (l) which represent the pores as illustrated in Figure 4.1. The tubes connect at nodes in groups of four. The nodes are considered without volume; all volume in the network model is contained in the tubes. The random sizes of the pores are modeled assuming tube radii following a Weibull probability distribution function (PDF). The fluid flow behavior inside the network of tubes is modeled as a modified Poiseuille flow. The traditional formulation of the Poiseuille flow is modified to include two-phase flow and capillary pressure effects [35]. The volumetric flow rate at a tube placed between the nodes ‘i’ and ‘j’, is defined as

$$q_{ij} = \frac{\pi r_{ij}^4}{8\mu_{ij}^c l} (\Delta p_{ij} - p_{ij}^c) \quad (4.1)$$

where r_{ij} is the tube radius, Δp_{ij} is the pressure acting across the tube, and p_{ij}^c is the capillary pressure in the tube when both phases are present. The volumetric flow rate definition is only valid when $\Delta p_{ij} > p_{ij}^c$; otherwise, $q_{ij} = 0$. Reverse flow is not considered and it is not likely to occur in a fuel cell, because water is continuously generated. If reverse flow is considered, then other effects such as fluid redistribution and fingering oscillations and breakup will have to be considered. The effective viscosity within a pore, (μ_{ij}^e) , is a function of the fluid position inside the tube (x_{ij}), the non-wetting (injected) fluid viscosity, (μ_{nw}) , and the wetting (displaced) fluid viscosity, (μ_w) . The effective viscosity is modeled to provide a smooth transition between the wetting and non-wetting viscosities while a pore is unsaturated:

$$\mu_{ij}^e = (\mu_{nw} - \mu_w) \frac{1 - \cos(\pi x_{ij}/l)}{2} + \mu_w \quad (4.2)$$

When a tube is filled with only one fluid, μ_{ij}^e is equal to the viscosity of that fluid.

The capillary pressure (p_{ij}^c) is also modeled as a function of the fluid position inside of the tube. At each node where four pores intersect, the capillary pressure is calculated using the average radius of the four tubes intersecting at that node. As the meniscus moves toward the middle of a tube, the capillary pressure is calculated using the tube radius. At the end of the tube, the capillary pressure is again calculated using the average radius of the four tubes at that node. The capillary pressure variation between these values is approximated using cosine functions to smoothly mimic the throat effect at the ends of the pores.

$$p_{ij}^c = \sigma \cos(\theta) \left[\left(1 - \frac{r_{ij}}{2\bar{r}_i} - \frac{r_{ij}}{2\bar{r}_j} \right) \frac{1 - \cos(2\pi x_{ij}/l)}{r_{ij}} + \frac{1 + \cos(\pi x_{ij}/l)}{\bar{r}_i} + \frac{1 - \cos(\pi x_{ij}/l)}{\bar{r}_j} \right] \quad (4.3)$$

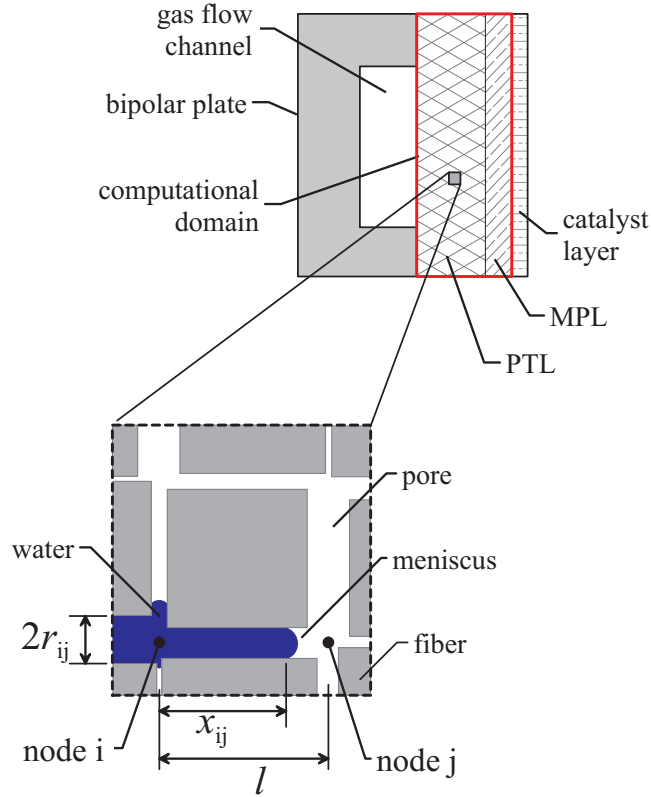


Figure 4.1. Schematic of computational domain and network model; blue indicates the nonwetting fluid (water), white the wetting fluid (gas) and gray the fiber structure. The computational domain encompasses the PTL and MPL if present spanning a single gas channel. Water is injected into the domain at the interface between the PTL and catalyst layer.

where \bar{r}_i and \bar{r}_j are the average tube radii around nodes ‘i’ and ‘j’, respectively, σ is the surface tension, and θ is the contact angle. The capillary pressure (p_{ij}^c) is zero when the tube is filled with only one fluid.

This model of the capillary pressure captures the effect of contact line pinning as a meniscus moves through the PTL. When a meniscus contact line pins, liquid pressure can deform the meniscus thereby changing the mean curvature and, subsequently, the capillary pressure while the meniscus remains stationary. The maximum pressure need not be restricted to the center of a pore and may occur at either node

depending on the pore distribution in the network model. The advantage of using this approximation for the capillary pressure at a pore level is that it eliminates any need of any capillary pressure-saturation relationship or measurement such as the J-Leverett function.

Conservation of mass requires that the flow rate balances at each node for every time step in the simulation. The four flow rates at each node ‘i’ must sum to zero.

$$\sum_{j=1}^4 q_{ij} = 0 \quad (4.4)$$

Substituting the relation for the flow in a single tube into equation (4.4) results in the pressure balance at each node.

$$\frac{\pi}{8l} \sum_{j=1}^4 \frac{r_{ij}^4}{\mu_{ij}^c} (\Delta p_{ij} - p_{ij}^c) = 0 \quad (4.5)$$

The unknown pressure gradient, (Δp_{ij}) , can be solved by rearranging equation 4.5. The resulting linear system of equations is solved using the conjugated gradient method. After calculating the pressure gradient, the new fluid position inside each tube is calculated proportional to the pressure gradient in that tube satisfying mass conservation, see Appendix A. A numerical code was developed in Fortran 95 to solve the linear system of equations and follow the time evolution of the fluid percolation.

4.3 Modeling the Porous Transport Layer

Due to the symmetry between the cathode and anode side, only one half of the fuel cell is simulated. This assumption reduces the computational time, but restricts

the ability to simulate effects such as back-diffusion to the anode. The portion of the PTL under a single channel is considered, as shown in Figure 4.1. Wall boundary conditions are used on the top side of the PTL in the contact region with the bipolar plate as well as on the lateral and bottom sides. The boundary condition along the channel side of the diffusion media layer is set to zero gauge pressure and all the water that reaches the gas channel is removed to avoid constraint/blockage of downstream water. Thus, when the water reaches the gas channel the percolation stops, thereby ending the simulation.

The zero gauge pressure at the gas channel, though not entirely accurate, is sufficient for this study. For most typical reactant flow field designs, the pressure in the cathode gas channel is approximately the same as in the anode side, resulting in a negligible back pressure on the water transport through the PTL. This premise may not be appropriate in an interdigitated flow field design [47]. Pressure variations within the reactant flow field could easily be incorporated into this network simulation if deemed necessary.

The water generated at the catalyst layer is modeled as a source term proportional to the cell current density. The injection flow rate is calculated based on a 1 kW fuel cell operating for 1 h at 0.1 A/cm^{-2} , which theoretically produces 0.4 L of water. This represents an overall flow rate of $1.2 \times 10^{-1} \text{ mL/s}$ for the fuel cell stack and is equivalent to $4 \times 10^{-11} \text{ mL/s}$ over each bottom node in the numerical simulations. The low current density was selected to ensure undisturbed capillary fingering without any water management issues to isolate the effect of morphology and wetting properties on liquid water transport.

The length of the tubes, or pores, is fixed to $25.2 \text{ }\mu\text{m}$ for all PTL simulations [14]. The constant length of the pore which at a first appears to be a limitation of

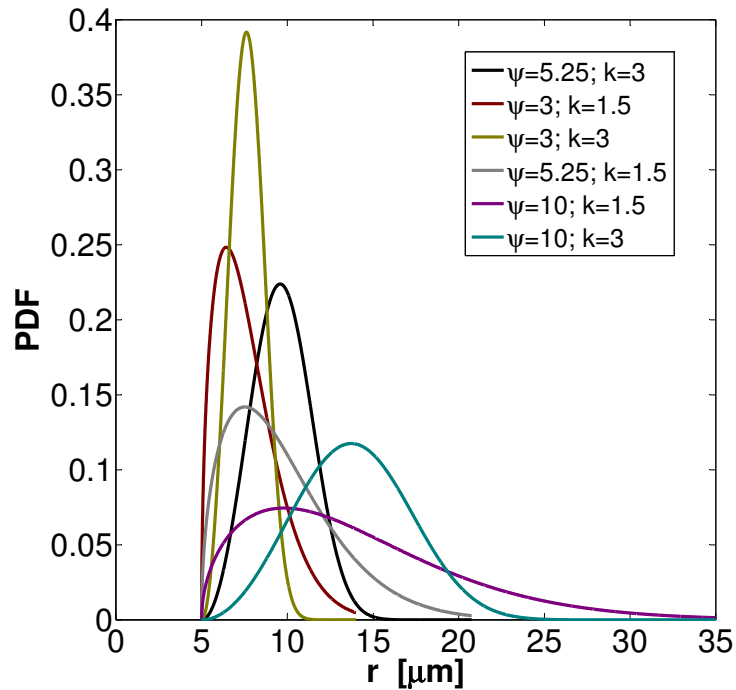


Figure 4.2. Normalized PDF of each Weibull distribution used to generate the PTL pore size distributions for the network simulation plotted against the pore size (r), in μm . ψ and κ are the Weibull probability distribution shape and scale parameters, respectively.

the network model is in fact compensated with an increase or decrease in the pore volume. The only effect of changing the pore length is on the time required to saturate a given pore. The numerical simulations consists of a regular lattice of 120×12 tubes or pores which gives a domain size of $3000 \times 300 \mu\text{m}$. A distribution of pore sizes, or tube radii, is generated using Weibull PDFs. Six Weibull PDFs were used. The shape (ψ) and scale (κ) parameters used for each Weibull distribution are given in Table 4.1 and the PDFs are plotted in Figure 4.2. These six distributions cover the pore size range of the most typical commercial PTLs. The reference model (model 1) probability distribution was taken from the method of standard porosimetry with

Toray T090 PTL [14]. Standard atmospheric values of water and air viscosities and surface tension are used. The fluid properties change slightly at fuel cell operating temperatures, but these changes do not affect the flow behavior as long as the PTL remains nonwetting.

Observations based upon a single, randomized pore network might be misleading, for example, the unlikely scenario where the generated network has a series of large pores that are connected to one another spanning the PTL thickness. The stochastic nature of the pore arrangement in a PTL was considered by generating three unique, random pore arrangements (called cases) generated for each morphology model analyzed, resulting in 18 PTL simulations. The results from the three simulations corresponding to model 1 are later used as reference for comparison with the other five models. In addition to pore size distributions, the effect of an MPL on water transport was investigated. This layer of fine pores is included in the three PTL structures generated from the model 1 Weibull PDF. The possibility of defects in the MPL was considered in the MPL pore size distribution. The baseline contact angle value used in the simulations was $\theta = 110$ degrees. The effect of PTL wettability was investigated using three additional contact angles of $\theta = 120^\circ$, 135° , and 150° . The simulation parameters used for each study are listed in Table 4.1.

Table 4.1. PTL parameters used in simulation results reported herein. The parameters varied include the Weibull distribution shape and scale factors, wettability, and presence of an MPL. The mean pore size corresponding to the Weibull distribution parameters is included for reference. The distributions are plotted in Figure 4.2. Morphology model 1 is used as the reference case and for the parametric studies on wetting and the effect of an MPL on water transport.

morphology model	Weibull distribution shape, ψ	Weibull distribution scale, κ	mean pore size, r_m [μm]	wetting θ	MPL
<i>reference model</i>					
1	5.25	3	9.6	110	no MPL
<i>wettability study</i>					
1	5.25	3	9.6	110, 120, 135, 150	no MPL
<i>morphology study</i>					
1	5.25	3	9.6	110	no MPL
2	3	1.5	6.4	110	
3	3	3	7.6	110	
4	5.25	1.5	7.4	110	
5	10	1.5	9.7	110	
6	10	3	13.7	110	
<i>MPL study</i>					
1	5.25	3	9.6	110	MPL, no defects
1	5.25	3	9.6	110	MPL with defects

4.4 Morphology Model 1 – Reference Cases

The scale and shape parameters of the Weibull probability distribution for model 1 are based on mercury standard porosimetry data for Toray T090 [14]. Three different PTL structures were generated from the model 1 PDF. In the simulations, the pore size distributions are different for each of the three cases, but the three PTL cases have the same pore size histogram corresponding to $\psi=5.25$ and $k=3$, as shown in Figure 4.3. The water distribution is different in each of the three simulations, because the arrangement of pores has been randomized within the constraints of the distribution parameters. The water distribution at the time when the water reaches the gas flow channel for each PTL structure is shown in Figure 4.4. This time is also the time at which the simulation ends. Due to the stochastic nature of the problem, the area covered by the water is slightly different for every case. The time for the water to reach the gas channel is also slightly different for every case, varying from 522 to 1192 s.

Two quantities are calculated during the percolation of water toward the gas flow channel. The first is the pore area occupied by the water from a cross-sectional view, referred to as the wetted area (A), and the second is the length of the interface between water and air from a cross-sectional view, referred to as the front length (S). These two time-dependent measures are used to quantify the water distribution inside the simulated PTL. Both are measures of saturation. The front length, (S), and the wetted area, (A), are normalized by the cell perimeter $2(L + H)$ and area $L \times H$, respectively, where L (3000 μm) and H (300 μm) are the length and width of the simulated PTL, respectively.

Figure 4.5a shows the non-dimensional front length (S^*) and wetted area (A^*)

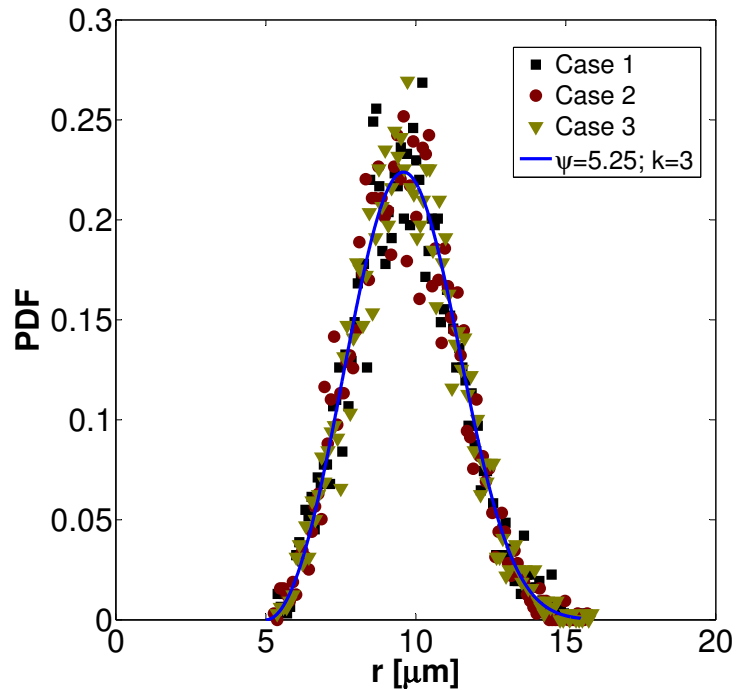


Figure 4.3. Normalized PDF plot of each PTL pore size distribution generated by using the model 1 Weibull probability distribution.

for the three cases corresponding to the reference model (PDF model 1). The non-dimensional wetted area can be understood as the beginning of a saturation curve. The average injection pressure (P_{avg}) at the bottom of the PTL, which is effectively the catalyst layer, for each of the three reference simulation cases is plotted in Figure 4.5b. This average pressure can be understood as the pressure at which the water is injected into the PTL. From the simulations, the average pressure curve is found to be similar to the pressure curve corresponding to a capillary fingering flow regime [43]. An average injection pressure of 4.5-5 kPa, the maximum non-dimensional front length being approximately twice the domain perimeter, and the maximum wetted area being a quarter of the total area are agree with the published data on capillary fingering percolation in PTLs [4, 43].

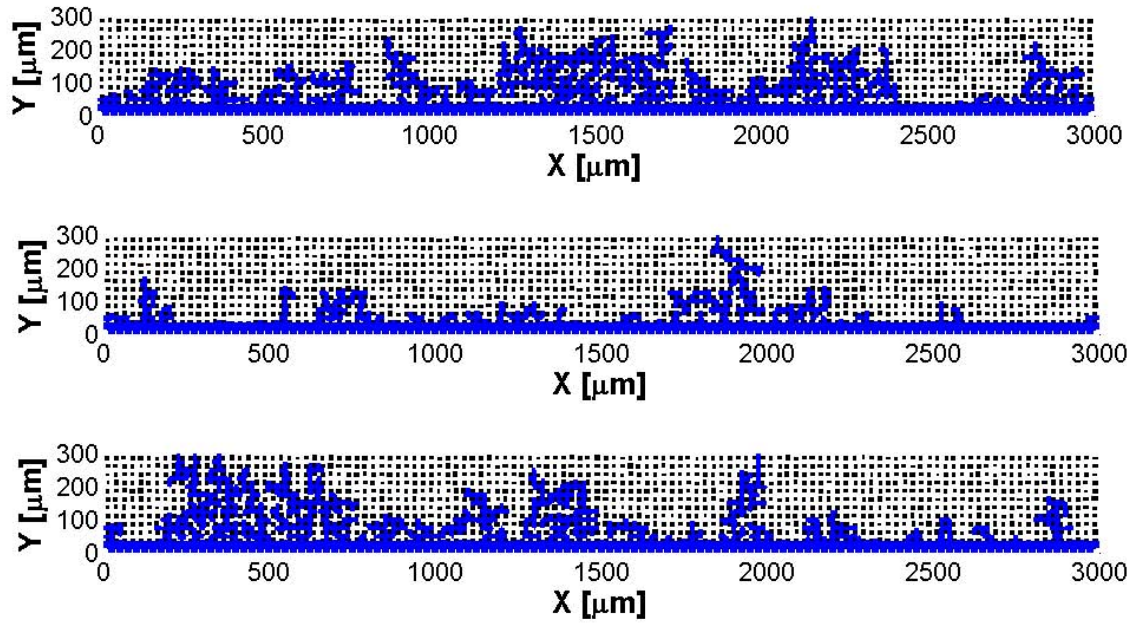
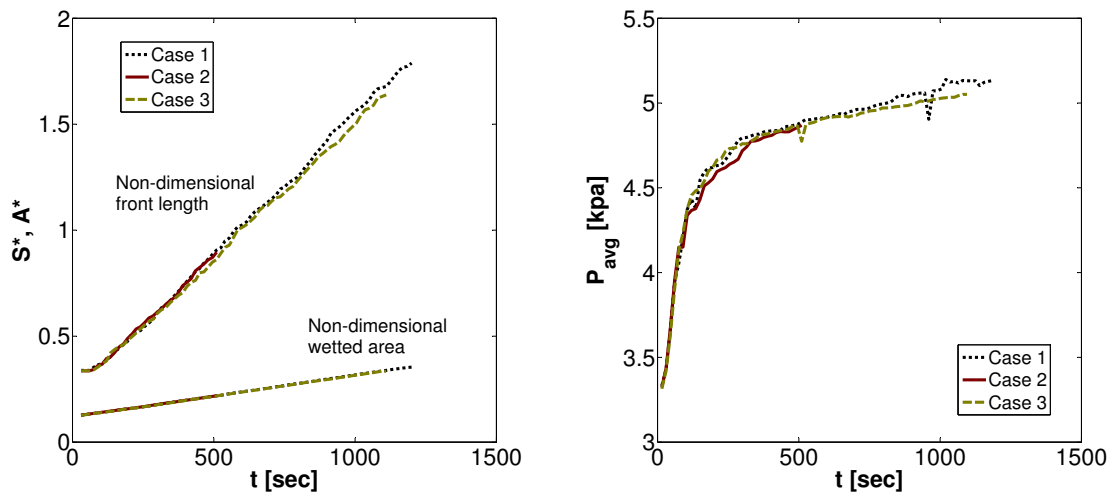


Figure 4.4. Water distributions after the water reaches the gas flow channel for the three simulation cases generated from the baseline pore size distribution. The location of water is denoted in blue, white represents air, and black represents the fiber structure of the PTL. Simulations end times are 1192 (top), 522 (middle), and 1095 s (bottom).

The non-dimensional front length, (S^*), and wetted area, (A^*), as well as the average injection pressure, (P_{avg}), collapse onto a single curve (Figure 4.5) despite a significant difference in PTL water content at the end of each simulation (Figure 4.4). The implication is that the transport of water is identical for each of the three cases. The stochastic nature of the pore arrangement within a distribution results in different times for water to reach the gas channel, as indicated by the maximum values obtained for S^* and A^* at the end of the simulation for each case in the plots shown in Figure 4.5.



(a) Non-dimensional front length S^* and wetted area A^* . (b) Average pressure driving water transport.

Figure 4.5. Non-dimensional measures of saturation and pressure in the PTL for the three network simulations generated from the model 1 PDF ($\psi = 5.25$, $k = 3$). The simulation ends when the liquid water reaches the gas flow channel.

4.5 Effect of PTL Wettability

The effect of PTL wettability on water transport was investigated using four different contact angles, $\theta = 110^\circ$, 120° , 135° and 150° . These four contact angles were applied to the same three reference network simulation cases generated from the morphology model 1 PDF for a total of 12 simulations. The three simulations corresponding to $\theta = 110^\circ$ are the same simulations discussed previously and shown in Figure 4.5. The non-dimensional front length (S^*), wetted area (A^*), simulation end time (t_{max}), and average injection pressure (P_{avg}), were calculated for each simulation. The results, shown in Figure 4.6, demonstrate a lack of sensitivity in the saturation measures (S^* and A^*) and simulation end time to variations in the PTL wettability as measured when the water reached the gas channel. The stochastic variation in the

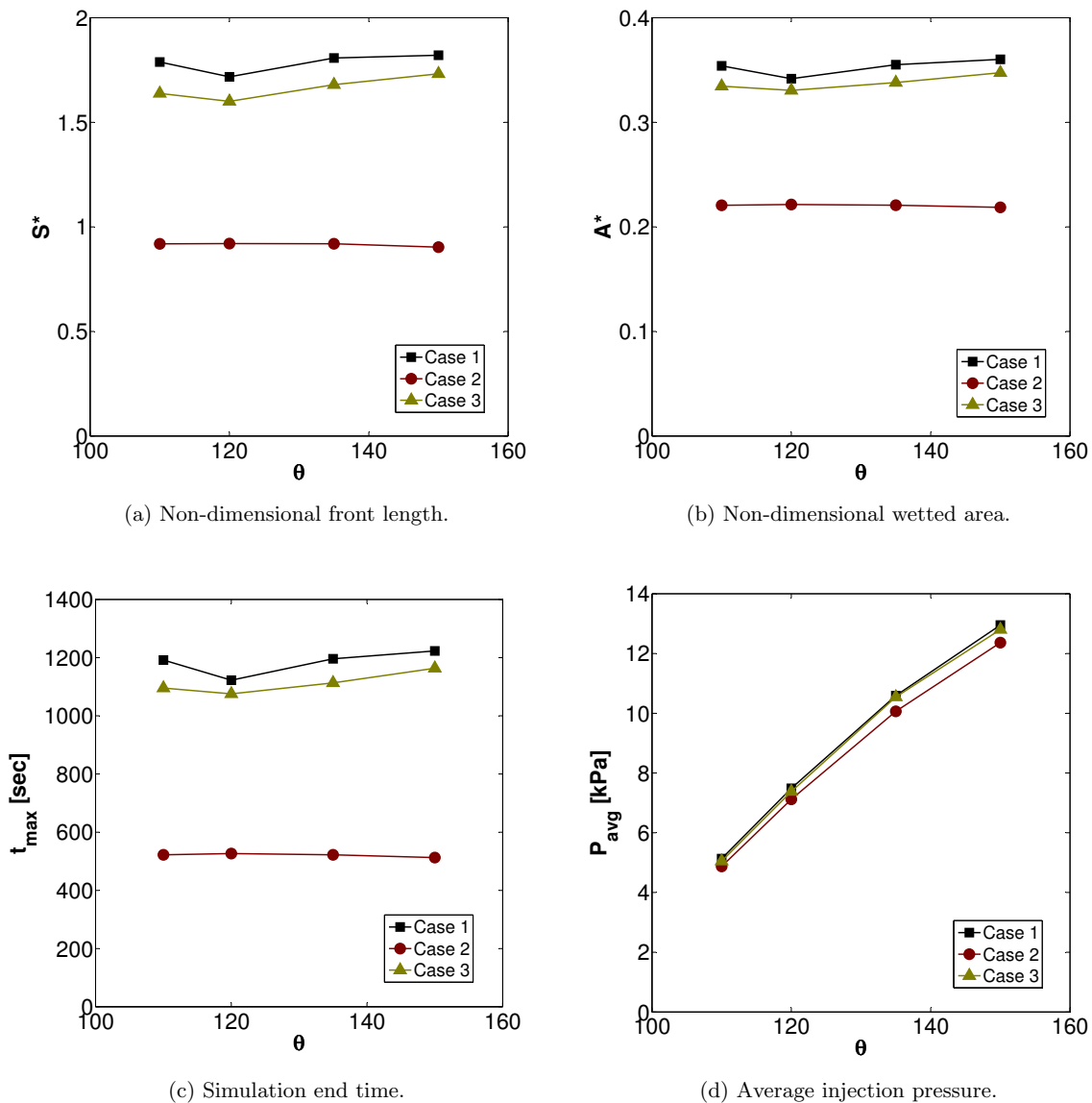


Figure 4.6. Effect of PTL wettability as measured by the static contact angle on the water percolation for the three cases generated using the model 1 PDF.

pore arrangement has a greater effect than does a 40° difference in wettability. This is because the pore arrangements of the three cases are the same for each contact angle studied so the water percolates through the same path as long as the contact angle remains greater than 90° . The average injection pressure does shows a strong

dependence on the contact angle as expected. The higher the contact angle, the higher the capillary pressure and the higher the average injection pressure required for the water to percolate through the PTL.

Care should be taken when interpreting these results with respect to experimental studies where the wetting properties are modified by increasing the PTFE content of a PTL. An increase in the PTFE content increases the capillary pressure irregularly and typically modifies the morphology of the PTL by completely blocking pores or reducing pore sizes. The capillary pressure is proportional to the wettability (contact angle) and inversely proportional to the morphology (pore size distribution). Therefore, the uncertainty in the wettability can be assigned to the uncertainty of the morphology in a similar manner to porosimetry where the contact angle is assumed constant along the PTL and all material variability is assigned to the pore size distribution. The presence of mixed wettability or a wettability distribution within the PTL has a similar effect to the changes in the morphology.

4.6 Effect of PTL Morphology

Six Weibull PDFs, shown in Figure 4.2, were used to study the effect of the PTL morphology on the water percolation. The corresponding shape (ψ) and scale (κ) parameters are listed in Table 4.1. For each PDF, three network pore distributions, called cases, were generated for a total of 18 PTL structures. The contact angle used for these simulations was $\theta = 110^\circ$. The simulation end time, (t_{\max}), and the values of S^* , A^* , and P_{avg} at the time that water reached the gas flow channel were calculated for each simulation and were plotted against the mean pore size of the distribution

in Figure 4.7. The times indicated in Figure 4.7c correspond to the time at which the value of S^* , A^* , and P_{avg} are plotted in Figure 4.7a, b, and d. As a general rule, longer simulation end times result in larger injected water volumes and larger PTL saturation level as measured by A^* and S^* .

The non-dimensional front length (S^*), shown in Figure 4.7a, increases from 1.2 up to 2.75 as the mean pore size increases from 7.5 to 14 μm . This behavior can be attributed to two causes. First, for a given volume of injected water, increasing the mean pore size increases the probability of existence of larger pores. When these larger pores are partially saturated, the water-air interface generated is larger as well. The second cause is that a broader pore size distribution, as measured by the Weibull's shape parameter (ψ) (from 3 to 10), implies a more spread arrangement of pore sizes which increases the chance of small pores to block the water percolation. This increases the tendency of finger formation and, consequently, increases the front length. Additionally, this increase in the randomness, or broader pore size distribution, of the PTL structure from $\psi = 3$ to 10 increases the ranges of S^* (from 0.05 to 1), A^* (from 0.01 to 0.15), and t_{max} (from 50 s to 2000 s). As the mean pore size is increased, the non-dimensional wetted area, shown in Figure 4.7b, increases in range but the average remains roughly the same. For example, the non-dimensional wetted area (A^*) is ~ 0.3 for the simulations corresponding to $\psi = 3$, whereas A^* is in the range of 0.2-0.5 for $\psi = 10$.

A larger average pore size requires on average a greater volume of water as the capillary finger moves towards the gas flow channel. Because the water injection rate is constant, more time is required as the mean pore size of the distribution is increased, as seen in Figure 4.7c. In contrast, the average injection pressure, shown in Figure 4.7d, decreases as the mean pore size is increased, because the capillary

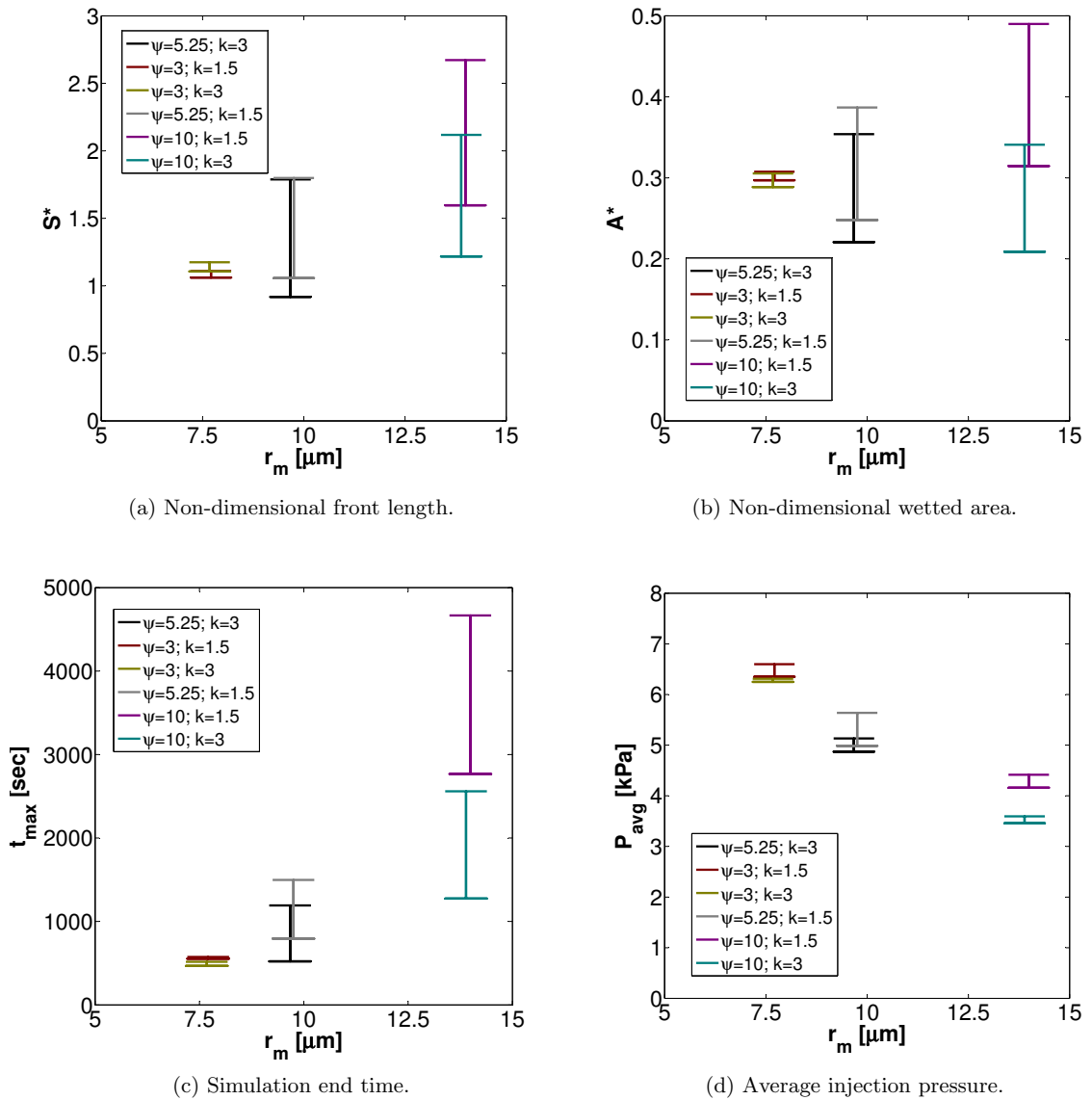


Figure 4.7. Non-dimensional front length (S^*), non-dimensional wetted area, (A^*), simulation end time (t_{max}), and average injection pressure (P_{avg}) for each pore size distribution listed in Table 4.1. The mean pore size corresponds to the PDF used to generate the PTL models. The bars indicate the maximum and minimum values obtained for the three cases in each morphology model.

pressure is inversely proportional to the pore radius, as described in equation (4.3).

The range in the average injection pressure for each morphology is similar, because

the water is percolating in capillary fingers at constant pressure [43] similar to the data shown in Figure 4.5b.

4.7 Effect of the MPL

The addition of a teflonated carbon layer with very small pores, known as an MPL, on the catalyst layer side of the PTL is simulated with a bimodal pore size distribution, as shown in Figure 4.8. The MPL was included on the three PTL cases generated from the morphology model 1 distribution with a contact angle of 110° . The range of the pore size within the MPL is arbitrarily set between 0.5 and $1.5 \mu\text{m}$.

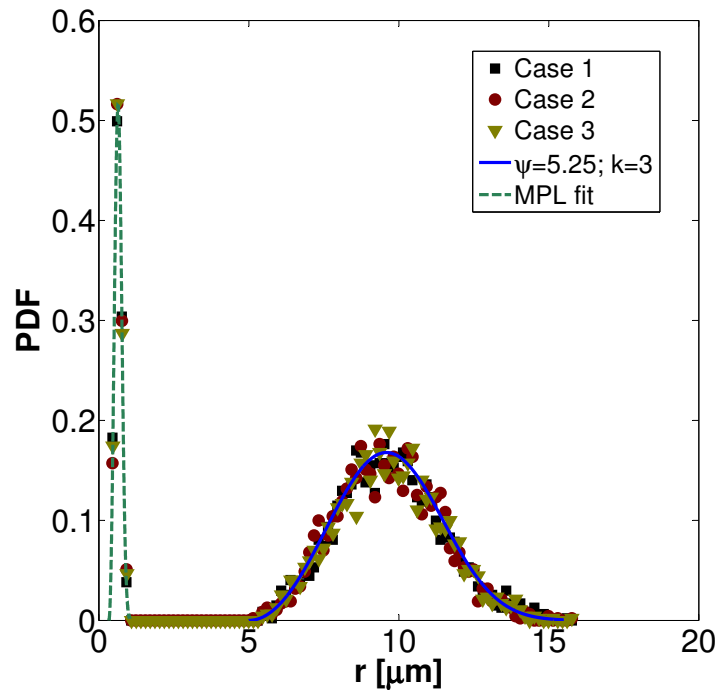


Figure 4.8. Normalized PDF for each PTL pore size distribution generated by using the model 1 Weibull PDF with the addition of an MPL distribution. The distribution centered near $10 \mu\text{m}$ is the same as shown in Figure 4.2.

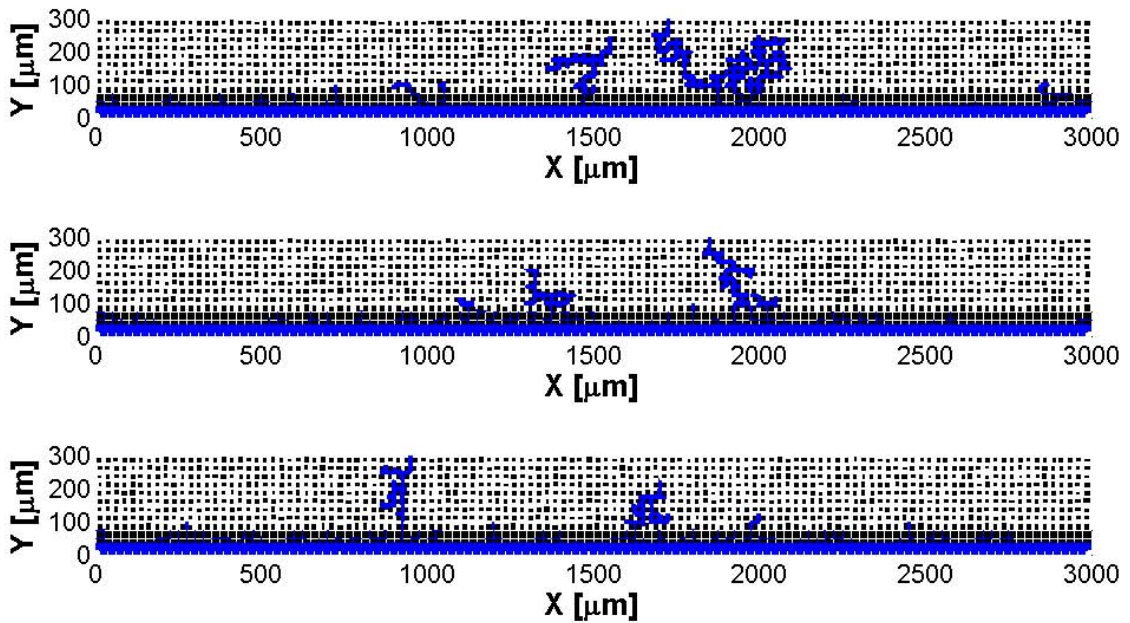


Figure 4.9. Water distributions when the water reaches the gas flow channel for the three cases generated from the model 1 PDF with an MPL. The area occupied by water is shown in blue, white represents air, and black represents the fiber structure of the PTL. The simulation end time are 250 (top), 120 (middle), and 100 s (bottom).

The PTL water distribution for the three cases after one finger reached the gas channel is shown in Figure 4.9. From this figure, a drastic reduction in the amount of water in the PTL is observed when compared to the simulation without an MPL shown in Figure 4.4. The simulation condition with and without the MPL are the same. The difference between both cases is that only a few small fingers are formed when the MPL is present. The reduction in the path size in which water percolates through the PTL reduces the time for the water to reach the gas channel by approximately an order of magnitude.

The time history of the non-dimensional front length, (S^*), non-dimensional wetted area, (A^*), and average injection pressure, (P_{avg}), are plotted in Figure 4.10. S^*

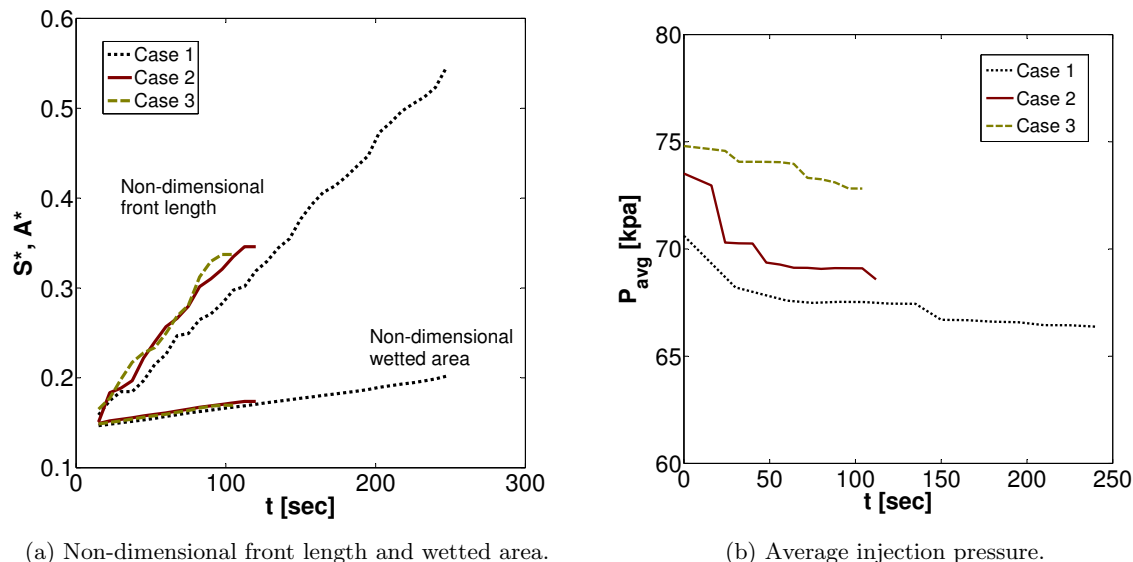


Figure 4.10. Non-dimensional measures of saturation and pressure in the PTL with MPL for the three network simulations generated from the model 1 PDF ($\psi = 5.25$, $k = 3$). The simulation ends when the liquid water reaches the gas flow channel.

and A^* indicate approximately 3 times less water within the PTL (Figure 4.10a) at the end of the simulation as compared to the cases without an MPL (Figure 4.5a). The water, when forced through the MPL, occupies only a few of the largest MPL pores. Thus, the presence of the MPL may serve to reduce the quantity of liquid water within the PTL through enhanced fingering instabilities, thereby facilitating the reactant access to the catalyst layer.

The incorporation of the MPL increases the average injection pressure by nearly an order of magnitude when compared to the case without an MPL. There is a very large capillary pressure associated with even the widest pore in the MPL ($\sim 1.5 \mu\text{m}$). Even after the water crosses the MPL, water below the MPL remains at an elevated pressure due to the flow resistance through the MPL pores. As the water flows through the PTL, the average injection pressure decays towards a constant value.

However, only the first case ran long enough to realize the leveling of the pressure (see Figure 4.10b). In cases 2 and 3, water reached the gas channel before the average injection pressure reached a steady value. Although there is a significant difference in the average injection pressures with and without the MPL, the liquid pressures within the PTL are nominally the same at 4.5-5 kPa with and without the MPL.

4.8 Effect of MPL Defects on Water Transport

Under normal conditions, even in a brand new sample, the MPL always contains some imperfections such as cracks. The influence of such defects was included in the morphology studies on water transport by singular large pores which spanned the thickness of the MPL. The same three reference cases from morphology model 1 with an MPL, shown in Figure 4.8, were used in the simulations. The conditions for the water transport simulations with MPL defects are identical to the simulations with an MPL having no defects. The simulations for the three cases were conducted with several defect scenarios. The location and size of the defects for the simulations were as follows. A single defect was simulated with one pore centered in the MPL of 4, 8, 16 and 32 μm . Two defects were simulated with two pores of 16 μm equally spaced along the MPL as well as placed side-by-side in the center of the MPL. Finally, three defects were simulated with three pores of 16 μm equally spaced along the MPL. The addition of MPL defects results in the capillary finger formation near the defect, as shown in Figure 4.11.

The non-dimensional front length (S^*), non-dimensional wetted area (A^*), and the average injection pressure (P_{avg}) were calculated for each of the three cases and

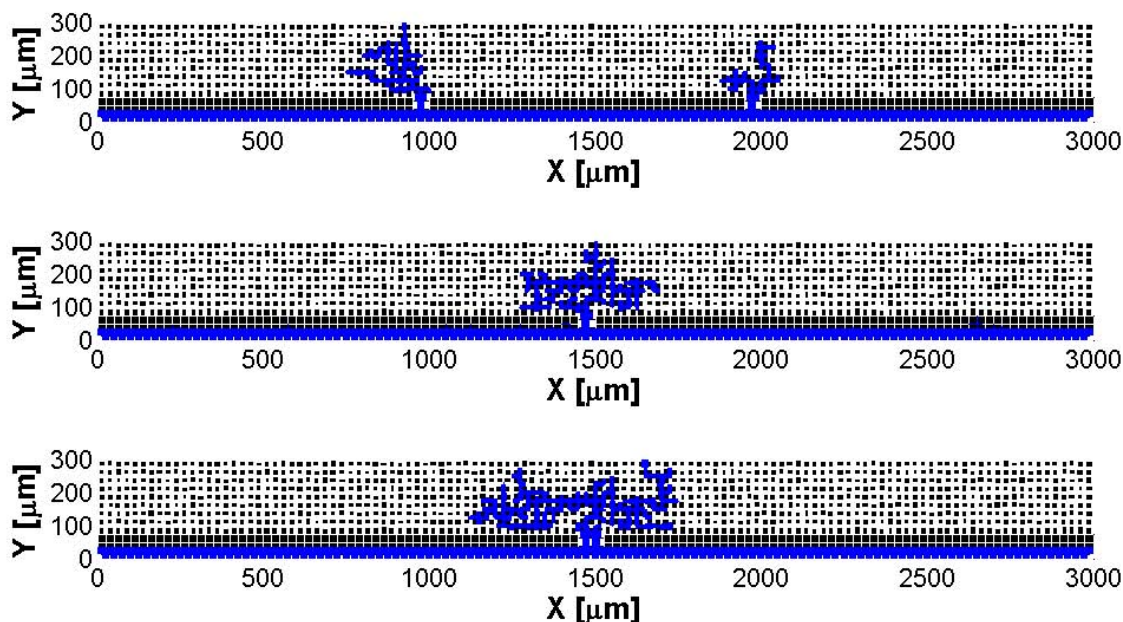


Figure 4.11. Defect scenarios for morphology model 1, case 1 with $d^* \approx 0.01$. Top: Single pore of $32 \mu\text{m}$ width at the center of the MPL. Middle: Two pores of $16 \mu\text{m}$ width located side-by-side in the center of the MPL. Bottom: Two defects of $16 \mu\text{m}$ width equally spaced along the MPL. The simulation end time are 215 (top), 340 (middle), and 200 s (bottom).

the values of each at t_{\max} are plotted in Figure 4.12 against the non-dimensional defect size, (d^*). The non-dimensional MPL defect size, (d^*), is defined as the width of the MPL defect divided by the width of the PTL. Thus, d^* represents an effective percentage opening through the MPL. The defect sizes range from 0.1 to 1.6%.

The addition of a defect, or crack, in the MPL results in a similar reduction in PTL water content as in the cases with an MPL having no defect (see Figure 4.12a and 4.12b) when compared to the PTL without an MPL. This effect persists with increasing d^* until a defect size of $\sim 0.5\%$ of the MPL width. Above this value of d^* , the saturation measures begin to increase and the effect of the MPL is diminished. For example, the three cases corresponding to an MPL with three defects having a

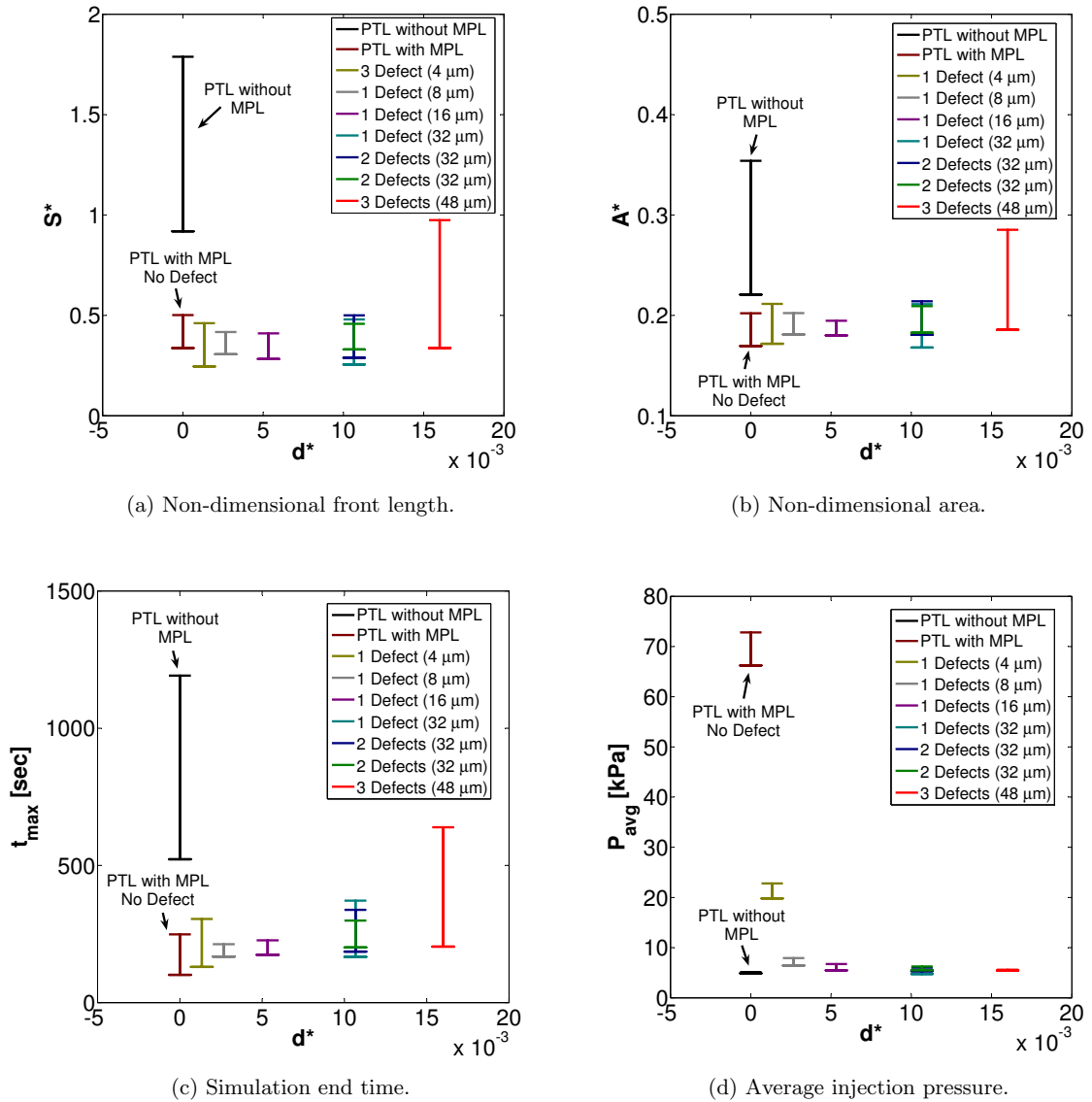


Figure 4.12. Effect of the MPL defect on the water transport in the PTL for the three cases generated using the model 1 Weibull PDF. The MPL defect size is nondimensionalized by the width of the PTL.

total opening of 48 μm ($d^* = 1.6\%$) have an upper range of A^* , which is slightly less than 0.3 and is comparable to the model 1 cases simulating a PTL without an MPL.

When an MPL without defects is included in the morphology, the injection pres-

sure is significantly increased as compared to the PTL without an MPL, 70 and 5 kPa, respectively. The presence of an MPL defect drastically reduces the injection pressure to a value comparable to a PTL with no MPL. For $d^* > 0.3$, the effect of the MPL on injection pressure is negligible. Thus, the presence of small defects in an MPL has the combined effect of reducing the saturation level of the PTL and retaining a low injection pressure for the water transport toward the gas flow channel.

These results mirror those of a recent experimental study in which small perforations made in a PTL resulted in improved fuel cell performance [11]. The optimum performance improvement occurred for a PTL with thirty-nine, 80 μm diameter holes in a 1×1 cm PTL. The ratio of the perforated area (0.0019 cm^2) to the total PTL area (1 cm^2) is equivalent to $d^* \approx 0.20\%$. This value of d^* lies in the range where the simulations indicate the lowest saturation and injection pressure conditions.

Generally, the water transport through the MPL has been thought to be in a vapor state due to the high temperature and capillary pressure associated with the small pore size [20, 49]. The presence of liquid water in the PTL is thought to be the result of condensation. The assumption that water crosses the MPL in a vapor state due to the high capillary pressure may not be appropriate when defects or cracks in the MPL are taken into consideration. The capillary pressure required to percolate through the MPL with cracks is approximately the same as in the case without an MPL. Thus, water could cross through the MPL in the liquid state and could induce a localized fingering in the PTL with low saturation and an imperceptible change in membrane pressure.

4.9 Conclusions

A two-dimensional network model was implemented to simulate a capillary two-phase flow (water and air) occurring in the PTL of a low-temperature fuel cell. This model was developed for a half fuel cell domain, yet the model can easily be extended to larger domains without a significant increase in computational expense. The capillary pressure was modeled considering the meniscus pinning within pores and the pore size distributions were generated using Weibull PDFs. Six different PTL models were analyzed by varying the scale and shape parameters of the Weibull distribution function. Three cases were generated for each distribution and a unique flow pattern was obtained for each of the simulations due to the stochastic nature of the network. A parametric study of the wetting properties of the PTL was also conducted considering four different contact angle values. For each numerical simulation, the non-dimensional pore area occupied by water from a cross-sectional view, the non-dimensional length of the interface between water and air from a cross-sectional view, and the average injection pressure of water were calculated. The simulations ended when water reached the gas flow channel.

The injection pressure would increase at the beginning of the simulation and reach a plateau consistent with capillary fingering in porous layers. The variation in pore arrangement for the three cases generated from each morphology was found to generate significant differences in the flow pattern at the time when water reaches the gas flow channel, though the three cases for each morphology model collapsed to a single curve when nondimensionalized. The effect of variation in contact angle was found to have minimal effect on saturation levels, S^* and A^* , due in part to the nature of the simulation. A 40° change in the contact angle had less effect on

saturation measures than did the stochastic generation of the networks. However, there was a significant effect on injection pressure as to be expected. When comparing the results of the six Weibull probability distribution models, an increased mean pore size generally resulted in a larger surface area of the water within the PTL as measured by S^* . The relationship between the mean pore size and water volume in the PTL as measured by A^* was less distinct. A wider pore size distribution resulted in a greater volume available for the water in the PTL and the time for the water to reach the gas flow channel increased. The average injection pressure decreased as the average pore size is increased.

The effect of an MPL on the PTL was explored by considering a bimodal pore size distribution in the network simulation. The presence of the MPL significantly reduced the saturation of the PTL through enhanced fingering formation. Due to the very small pore sizes in the MPL, the injection pressure was significantly increased. The increased pressure may be advantageous in maintaining a uniform membrane hydration in PEM fuel cells, yet the value of the average injection pressures are too large to be considered realistic for actual membrane pressures. However, defects (cracks) within the MPL were shown to reduce the average injection pressure to levels comparable to a PTL without an MPL while maintaining a reduced saturation level.

5. COMPARISON OF NUMERICAL PREDICTIONS AND EXPERIMENTAL RESULTS OF WATER PERCOLATION IN PEM FUEL CELL POROUS TRANSPORT LAYERS

A series of numerical simulations using a three dimensional network model are presented. These numerical simulations are carried on in similar conditions occurring during a pseudo Hele-Shaw experimental setup. The numerical simulations using the network model are compared with experimental data through a new scaling of the water percolation in porous media which is based on the ratio dissipated energy. The morphology and wettability of the PTL are tuned to fitting the experiment by using the proposed scaling. Once the fitting between numerical and experimentally is obtained, such PTL structure information can be used in different types of simulations where the conditions are representative of the fuel cell operating conditions.

5.1 Introduction

Lately, there has been considerable effort in modeling water percolation in the gas diffusion layer or porous transport layer (PTL) of PEM fuel cell. Modeling approaches such as network simulation or Lattice-Boltzmann methods have been implemented with varying degrees of success [14, 33, 41, 42, 55, 56, 58]. Numerical simulations help to understand the effect of the most significant variables on water percolation in PTLs such as the morphology (pore size distribution), wettability (contact angle) and defects such as cracks [42]. Normally, water percolates through the PTL pores offering the lowest capillary resistance; the flow results in formation of capillary fingers [39, 43]. At high current density water is produced faster than it can be removed, flooding pores with higher capillary resistance thereby reducing the reactant gas permeability and the fuel cell efficiency. Simulations using the network model have been shown to accurately capture water percolation and specifically capillary fingering in PTLs [42].

Experimental validation of these numerical simulations has been limited. Most of the experiments used as validation were based on model porous media [3, 5]. In many cases the validation is a simple qualitative comparison between the percolation pressures, the saturation curves, or Leverett functions. The comparison of one of these parameters alone usually is not enough to validate the numerical simulations. In-situ validation is difficult due to the opacity of the PTL and its surrounding fuel cell components like the bipolar plate [2]. Exceptions are the very sophisticated techniques such as neutron and x-ray imaging where the main limitation is temporal resolution. To overcome these limitations, an ex-situ experiment has been developed using transparent materials with purpose of gaining visual access and extending the experiment time to achieve sufficient spatial and temporal resolution for comparison

to numerical simulations.

In this work, results using a three dimensional network model simulating the experimental conditions are presented. The numerical model includes a PTL where the boundary and initial conditions are set to represent the conditions occurring in a pseudo-Hele-Shaw experiment as described in Medici and Allen [43]. The PTL structures used in the simulations are generated using a range of pore size distributions. From the numerical simulations, the amount of water held in the PTL and the percolation pressure are obtained for different PTL structures and flow rates.

The numerical simulations are compared with existing experimental data using a new scaling analysis of drainage in porous media. This new scaling is based on the ratio between the input and dissipated energies associated with the water percolation. The percolation pressure and the amount of water held in the PTL are combined to calculate the input and dissipated energy. When this energy ratio is plotted against a non-dimensional time, a linear relationship is obtained with a unique slope for each type of PTL. This result provides a convenient characterization for water percolation in a PTL.

5.2 Numerical Modeling

The three-dimensional network model assumptions are the same as in the two-dimensional approaches [35]. The difference between the three and two dimensional network models is that six pores are connected to every node instead of four pores. Figure 5.1 shows a schematic representation of the pore arrangement. E, W, N, S, T, B, and P stands for the east, west, north, south, top and bottom nodes of the reference

node P. The fluids are considered incompressible and modeled as Poiseuille flow. A source term is added to the pressure to include the effect of the capillary pressure and an effective viscosity is used to include the two-phase flow. The volumetric flow rate at a generic tube placed between two nodes is:

$$q_{ij} = \frac{\pi r_{ij}^4}{8\mu_{ij}^e l} (\Delta p_{ij} - p_{ij}^c) \quad (5.1)$$

This relationship is only valid when $\Delta p_{ij} > p_{ij}^c$, otherwise q_{ij} is set to zero. The effective viscosity, μ_{ij}^e , is a function of the non-wetting fluid position inside the tube x_{ij} varying from the non-wetting (injected) fluid viscosity to the wetting (displaced) fluid viscosity as the fluid is percolating through the channel. The capillary pressure is also a function of the non-wetting fluid position inside of the pore and the same model presented by Medici and Allen[42] is used:

$$p_{ij}^c = \sigma \cos(\theta) \left[\left(1 - \frac{r_{ij}}{2\bar{r}_{ij}} - \frac{r_{ij}}{2\bar{r}_j} \right) \frac{1 - \cos(2\pi x_{ij}/l)}{r_{ij}} + \frac{1 + \cos(\pi x_{ij}/l)}{\bar{r}_i} + \frac{1 - \cos(\pi x_{ij}/l)}{\bar{r}_j} \right] \quad (5.2)$$

where \bar{r}_i and \bar{r}_j are the average pore size around the ends nodes corresponding to that pore. The capillary pressure p_{ij}^c is zero when the tube is filled with only one fluid.

The sum of all the flow rates at a particular node must be zero. The resulting linear system of equations is solved using the conjugated gradient method to obtain the unknown pressure gradient, Δp_{ij} , at each node. After calculating the pressure gradient, the new fluid position, inside each pore is calculated and the process repeats for each time step, see Appendix A.

The PTL pore structure is generated by randomly assigning pore radii while con-

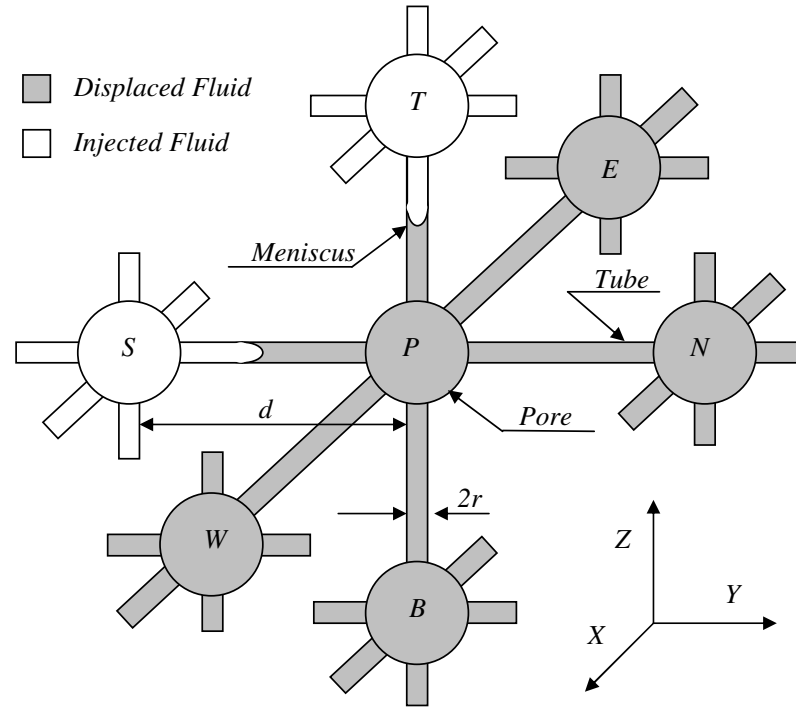


Figure 5.1. Three dimensional network model schematic representation. E, W, N, S, T, B, and P stands for east, west, north, south, top and bottom nodes of the reference node P.

straining the network to a pore size distribution. The distribution of pore size is generated following a Weibull probability distribution. Different PTL structures were generated by varying the shape, ψ , and scale, κ , parameters in a Weibull probability distribution function.

The parameters corresponding to $\psi = 5.25$ and $\kappa = 3$ were obtained by using the mercury intrusion porosimetry on a Toray T060 PTL [14]. The rest of the PTL pore size distributions are the same used in the article by Medici and Allen [42] where the shape parameter varies from $\psi = 5.25, 3$ and 10 ; and the scale parameter from $\kappa = 3$ and 1.5 . The length of the pores is fixed to $25.2 \mu\text{m}$ for all the PTL models. The numerical model consists of a regular lattice of $100 \times 100 \times 10$ pores which results in a

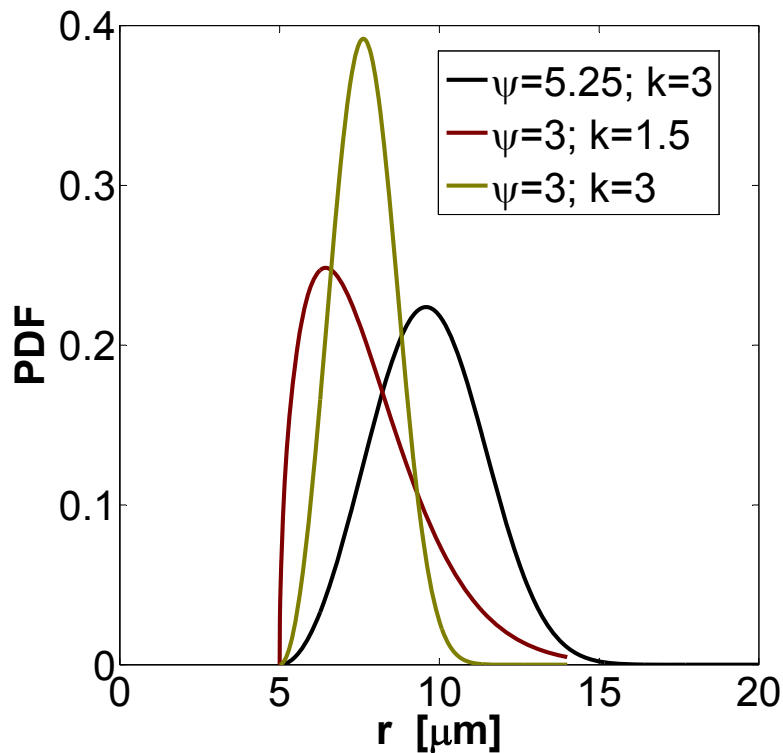


Figure 5.2. Weibull distribution function showing ψ and κ .

domain size of $1250 \times 1250 \times 125 \mu\text{m}$. A standard value of 110 degree contact angle is used in most of the simulation. However, for the case presented herein the contact angle is varied up to 135 degrees to obtain a good fit between the numerical and experimental data.

The boundary conditions are set to represent the conditions in the pseudo Hele-Shaw experimental setup. Wall boundary conditions on the top and bottom were used. The lateral sides open to the atmosphere are modeled as a fixed value zero gauge pressure. Water injected in the middle of the bottom side is modeled as a source term along the PTL central nodes. When a water finger reaches the one of the lateral sides the simulation is ended. The injection flow rates are the same as in the experiment.

5.3 Numerical and Experimental Comparison

A pseudo-Hele-shaw experiment was designed in which a porous transport layer (PTL) is compressed between two pieces of transparent polydimethylsiloxane (PDMS) and PMMA plates. The PDMS layers provide a compliant surface so as to avoid large gaps between the PTL surface and the PMMA compression plates. Water is injected at six different flow rates into the center of the fifty millimeter diameter PTL sample from the bottom side and a camera located above the sample records the water percolation. A pressure transducer is located at the injection point measures the percolation pressure. The pressure and the images are correlated as the water is injected in the PTL. The wetted area is extracted via image processing for each video frame. Complete details of the experimental apparatus are provided in [43].

Typically, the percolation pressure (also referred to as the capillary pressure), the saturation, or a combination of both is used to characterize water transport in a PTL. This approach does not account for capillary dynamics. In particular, the balance between viscous and capillary effects that may result in capillary fingering are not considered.

In this work, the comparison between the numerical simulations and the experimental results is accomplished by using a new scaling of drainage in porous media [43]. In this new scaling, the percolation pressure, the wetted area, and the injection rate are combined into a ratio of injection and dissipated energies. The injection energy is proportional to PQ , while the dissipated energy is proportional to $Q^2\mu l/h^4$. The ratio of these energies is defined as C_e :

$$C_e = \frac{Ph^3 A}{\mu Q l^2} \quad (5.3)$$

the term A/l^2 is a correction factor to compensate for the area cover by the water. In this scaling, Q is the injection rate at the center of the sample. The injection pressure, P , is equivalent to the percolation pressure and is a measure of the capillary pressure. The wetted area, A , is a measure of the time-dependent saturation. Two length scales are used. The small length scale, h , is the sample thickness and the large length scale, l , is the sample size, which for this study is the diameter of the PTL sample. The energy ratio, C_e , is time-dependent through the wetted area and the percolation pressure. A non-dimensional time t^* is defined as:

$$t^* = t \frac{\sigma h^2}{\mu l^3} \quad (5.4)$$

where μ is the injected fluid viscosity and σ is the injected fluid surface tension.

The experimental value of P and A are the one presented by Medici and Allen [44]. Figure 5.3 shows the experimental energy ratio versus the non-dimensional for different flow rates for the Toray T060 PTL with 9% PTFE content by weight. The flow rate for each test run is presented in the form of capillary number, C_a , which is defined as $C_a = \mu Q / \sigma h^2$. The capillary number is based on the injection rate and is therefore only a reference condition. The local capillary number at each moving menisci will not be the same as the reference C_a . Determination of the onset of percolation, which defines $t = 0$, requires careful consideration. An incorrect time for $t = 0$ will induce an unrealistic offset of the data.

As the reference capillary number is increased, the flow regime change from stable displacement at small t^* to capillary fingering at large t^* . As the transition between stable displacement and capillary fingering occurs the dissipated energy is reduced and the C_e increases. An advantage of this scaling is the possibility to distinguish between

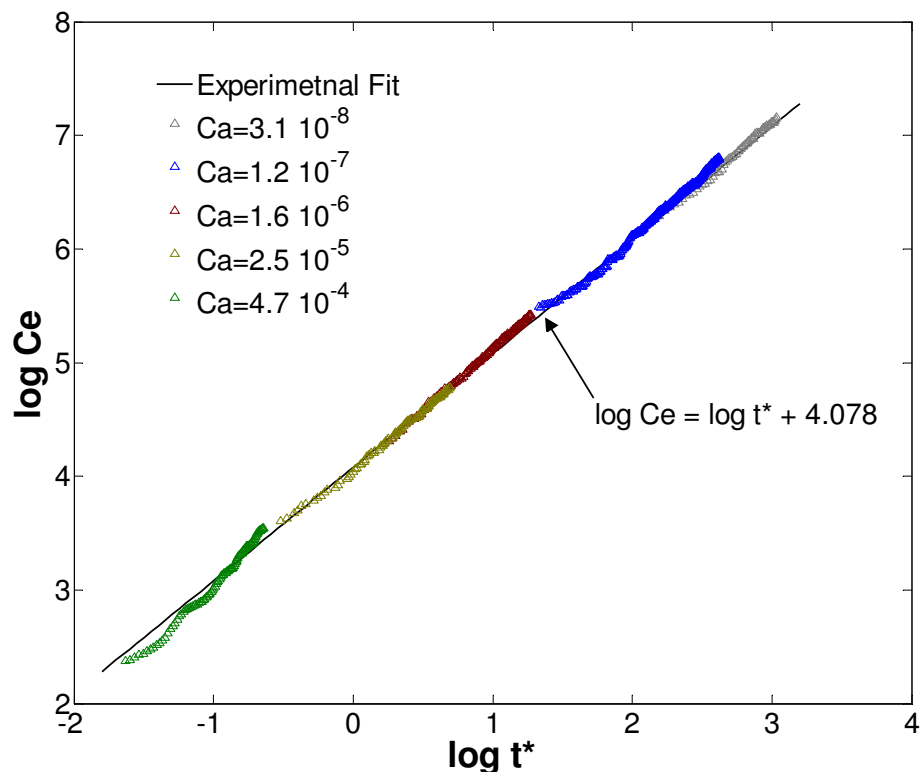


Figure 5.3. Experimental C_e plot for Toray T060, 9% (wt) PTFE content. Solid line corresponds to the fitting curve of the experimental results while dashed lines correspond to experimental data for each capillary number tested.

the capillary fingering and stable displacement by examining non-dimensional time t^* . Transition between capillary fingering and stable displacement occurs at $t^* = 1$.

When the C_e for each reference C_a is plotted on a log-log scale, the data aligns suggesting a proportional relationship between the energy ratio and the non-dimensional time. A linear regression fit through all of the experimental C_e is plotted in the log scale in Figure 5.3. The alignment of these curves implies the existence of a continuum process as the reference capillary number is increased but not a continuation of the experiment itself. The reference capillary number is just a non-dimensionalization of the flow rate used in that experiment. The local capillary number, measured at the

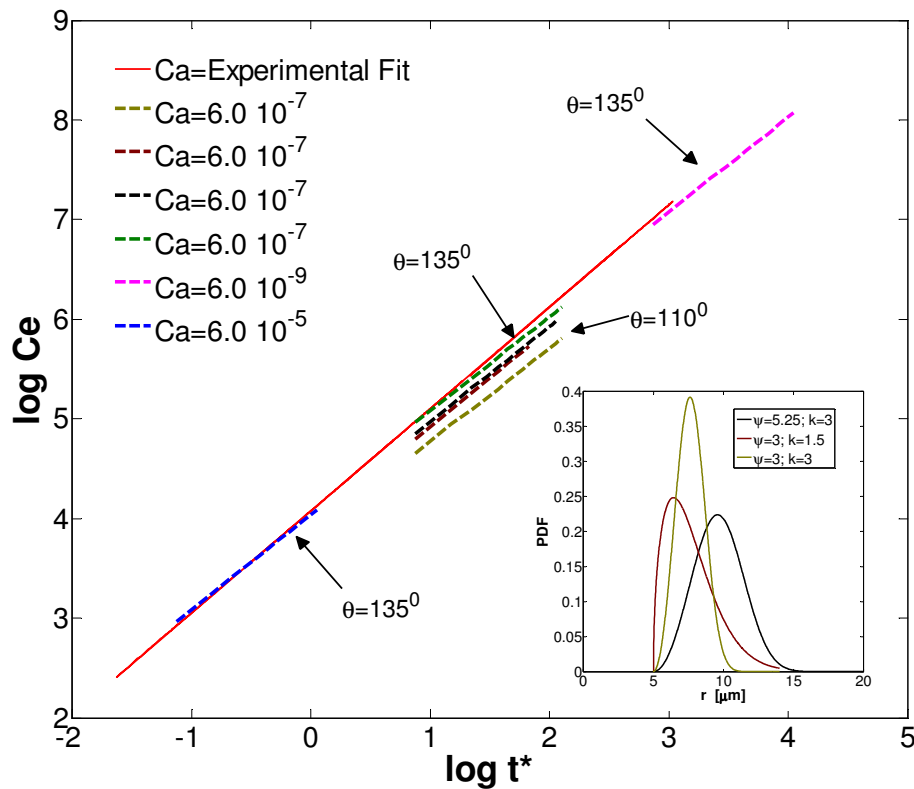


Figure 5.4. Numerical and experimental C_e plot. Solid line corresponds to the fitting curve of the experimental results while dashed lines correspond to numerical simulation. The contact angles used in every simulation are indicated with annotations. The colors of the numerical C_e match the colors of the Weibull distribution used to generate its pore size distribution.

water-air interface, continuously decreases together with the dissipated energy as the water is injected and spread in the porous media. However, in most of the experiments there is not much overlap of the data except between $C_a = 2.5 \times 10^{-5}$ and $C_a = 1.6 \times 10^{-6}$, and $C_a = 1.2 \times 10^{-7}$ and $C_a = 3.1 \times 10^{-8}$. This overlap implies that the same dissipated energy ratio can be obtained at the end of one of the experiment when the water occupied a high portion of the porous media or at the beginning of an experiment at a lower injection flow rate.

The energy ratio for each numerical simulation is plotted together with the fitting

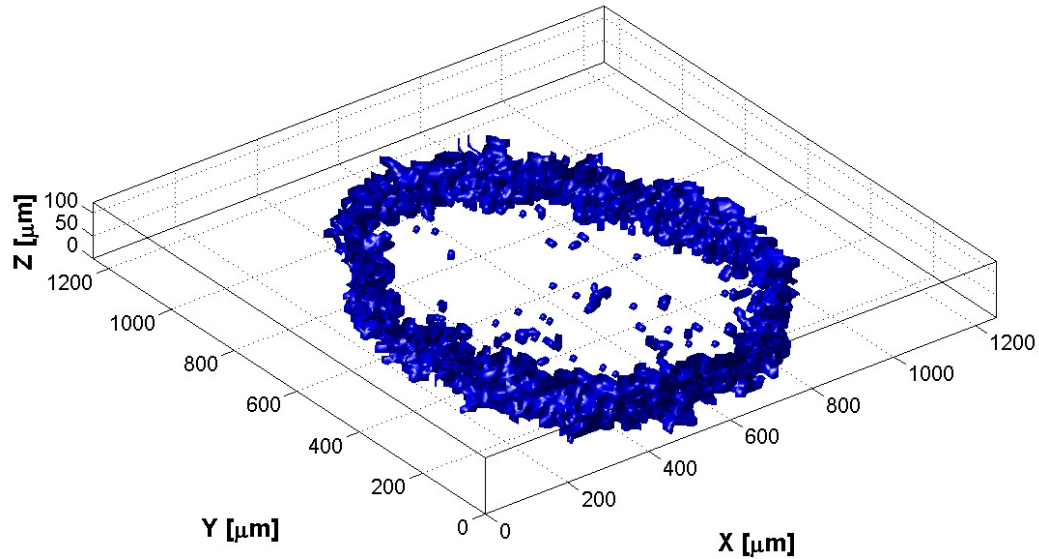


Figure 5.5. Water distribution after reaching one of the edges for the numerical simulation corresponding to $C_a = 6.0 \times 10^{-5}$, pore size distribution having $\psi = 5.25$ and $\kappa = 3$ Weibull parameters, and contact angle of 135° . The location of the water-air interface is denoted in blue.

curve of the experimental results in Figure 5.4. To make the comparison as close as possible, the wetted areas, A , for each numerical simulation were calculated from a top view as in the experiments. The percolation pressures, P , were calculated as the pressure gradient between the central nodes (where the water source terms are placed) and the lateral sides of the PTL. Figure 5.5 shows that Water distribution after reaching one of the edges for the numerical simulation corresponding to a pore size distribution having $\psi = 5.25$ and $\kappa = 3$ Weibull parameters.

From Figure 5.4, the pore size distribution can have a coupled effect of change on the slope and offset of the energy ratio curve. A change in slope is observed when comparing the curves corresponding to different pore size distribution, i.e. $\psi = 5.25$, $\kappa = 3$ and $\psi = 3$, $k = 1.5$. The three numerical simulations were obtained using a contact angle of 110 degrees and fixed flow rate representing a reference

capillary number of 6.0×10^{-7} . To obtain the same energy ratio between the numerical simulations and experiments for a PTL corresponding to Toray T060, the network model generated using $\psi = 5.25$ and $\kappa = 3$ was rerun with a contact angle of 135 degrees. The 135 degree contact angle induces a satisfactory offset to make the numerical and experimental results comparable.

Once the proper offset and slope were obtained, two additional numerical simulations were performed at different reference capillary numbers to verify the validity of the scaling at extreme values. Capillary numbers of 6.0×10^{-9} and 6.0×10^{-5} were used for the capillary fingering (dashed blue curve) and stable displacement (dashed red curve) simulations, respectively. The resulting energy ratio data, also plotted in Figure 5.4, are in good agreement with the experimental results in these ranges of capillary number.

5.4 Conclusions

The Weibull scale and shape parameters used in this work to compare the numerical and experimental results were obtained from the mercury intrusion porosimetry technique. However if this information would not be available, they can be found iterating on the Weibull parameter until match the experimental energy ratio. This fact leads to two conclusions on network model, first it captures the nature of the problem and it is able to accurately predict drainage and second it permits to find the parameters required for a particular PTL to be later used on a modeling of a fuel cell. The comparison presented here between numerical simulations and experiments used in PTL of PEM fuel cell can be used in other fields involving porous media.

This new scaling of drainage in porous media has the advantage of identifying the transition between stable displacement and capillary fingering. Another advantage is that PTLs made by different manufacturers will have energy ratio versus the non-dimensional curves with different offset and slope. The concept that every PTL with different morphology/wetting properties will have different energy ratio versus the non-dimensional can potentially be used as a characterization method.

The morphology and wettability of the PTL are tuned in the numerical simulations to modify the energy ratio slope in order to match the energy ratio obtained experimentally. After the morphology and wettability are tuned, the resulting PTL structure can be used in different types of numerical simulations representing the fuel cell operating condition simply by changing the boundary and initial conditions. These numerical simulations enable the study of the effect of the water percolation on that particular PTL when coupled with other fuel cell components.

6. SUMMARY AND RECOMMENDATIONS

The contributions presented in this project will lead to a better understanding of the mechanisms controlling the water percolation through the PTL. This will enable more efficient water management strategies in low temperature fuel cells, especially at high current density. An example of this is the reduction in the water content in the PTL as result of the inclusion of the MPL and its defects. Additionally, the study of the PTL wettability property leads to a better understanding of the coating effect on the water percolation can also be used to characterize degradation of PTL.

Based on the numerical simulations presented in this project, it was demonstrated that the network model is a simple, reliable computational tool able to capture the nature of the water transport in the PEM fuel cell. The use of this numerical model reduces the computational requirements when compared with other methods, which reduces the research and developing costs by reducing the cost of the equipments and research time.

6.1 Summary

The water transport analysis in PTL was carried on experimentally and numerically (ex-situ). A series of numerical simulations using a 2D and 3D network model

were conducted in order to explore the water percolation in the PTL.

The experimental setup was designed to accomplish the following objectives:

- Have visual access to the in-plane water percolation in the PTL in order to identify the different drainage water flow regimes and demonstrate that the PTL can sustain a non-uniform liquid distribution. Images were recorded at regular time intervals which were different depending on the duration of the experiment. From an image post processing, the temporal evolution of the wetted area, area covered by the water from a top view, was obtained.
- Measure the percolation pressure drop associated to every particular drainage flow regime in parallel to the imaging.
- The percolation pressure and the wetted area were combined into a single variable using a new scaling for water percolation in porous media. The newly defined scaling, called C_e , is proportional to the ratio between input and dissipated energy. A linear relationship was obtained when plotted against the non-dimensional time. This new scaling allows to substitute the drainage phase diagram by a curve and identify the transition between capillary fingering and stable displacement.
- Develop criteria to characterize PTL's based on their susceptibility to fingering instability. A significant offset (in the logarithmic scale) or slope (in the linear scale) in the C_e curve was obtained among PTL made by different manufactures. This offset/slope could be potentially used to characterize not only PTL but porous media in general.
- Corroborate the results obtained from the numerical simulations, showing that

the network model is able to capture the nature of the water transport in the PTL by comparing against the experimental data using the new scaling of drainage in porous media.

The numerical simulations were carried out to accomplish the following objectives:

- Study the effects morphological and wetting properties on the water percolation in PEM fuel cells. The effect of different pore size distributions and contact angles were studied.
- The MPL was study as PTL with a bimodal pore size distribution. It was found that the MPL reduces the water content in the PTL by facilitating the formation of water conduits. Because the MPL acts as barrier for the water percolation, the amount of water in the PEM must be increased.
- Defects or cracks in the MPL were also studied. It was found that the presence of small defects can keep the water content in the PTL as low as in the case of the undamaged MPL while reducing the percolation pressure. However, for large defects the effect of the MPL on he water percolation start to vanish.
- A three-dimensional version of the network model was developed to simulate the percolation in similar conditions existing in the pseudo Hele-Shaw experimental setup. The simulation were corroborated against experimental data using the newly defined scaling for drainage in porous media.

6.2 Recommendations

The material and concepts presented in this dissertation are still in developing stages. The following ideas can be used to improve the actual characterization and simulation methods as well as extended beyond fuel cell research. The PTL characterization method and the validation of the numerical simulation using the C_e plot can be applied to other research areas such as oil recovery, drug delivery, drainage in soil, foams characterization, among other application involving porous materials. The following are tasks that can be further developed:

- Perform drainage experiments on PTLs in viscous fingering regime. A possible recommendation for this kind of experiments, in order to obtain the percolation pressure and the wetted area in parallel (issue described in Chapter 1), is the use of fluorescent dye to identify the interface between the displaced and injected fluids.
- Present the data from viscous fingering experiments on PTL in the form of C_e plots and derived proper conclusions.
- Create a C_e database of different PTL for characterization and optimization purposes.
- Perform the pseudo Hele-Shaw tests on different porous materials than PTL and present the corresponding data in the form of C_e plots.
- Investigate the effects of different fluid properties on the C_e plot.
- Verify the C_e plot by comparing against analytical solution for idealized situation.

- Extend the network model formulation to include temperature gradient, evaporation and condensation. Even though these are very important parameters in the fuel cell research area, by including these in the formulation, the network can be used to model other systems.
- Integrate the network model into a larger and more complex fuel cell model.
- Optimize the PTL morphological and wettability properties using the network model for a particular fuel cell operating condition.
- Develop a network model able to simulate imbibition including corner flow effect.
- Study the effects of degradation, temperature gradient, and compression of the PTL on the C_e plot and validate the numerical simulations for these conditions to explore their effects on the fuel cell performance.

REFERENCES

- [1] P. M. Adler and H. Brenner. Multiphase flow in porous media. *Annual Reviews in Fluid Mechanics*, 20(1):35–59, 1988.
- [2] A. Bazylak. Liquid water visualization in PEM fuel cells: A review. *International Journal of Hydrogen Energy*, 34(9):3845–3857, 2009.
- [3] A. Bazylak, D. Sinton, and N. Djilali. Dynamic water transport and droplet emergence in PEMFC gas diffusion layers. *Journal of Power Sources*, 176(1):240–246, 2008.
- [4] J. Benziger, J. Nehlsen, D. Blackwell, T. Brennan, and J. Itescu. Water flow in the gas diffusion layer of PEM fuel cells. *Journal of Membrane Science*, 261(1-2):98–106, 2005.
- [5] O. Chapuis, M. Prat, M. Quintard, E. Chane-Kane, O. Guillot, and N. Mayer. Two-phase flow and evaporation in model fibrous media: Application to the gas diffusion layer of PEM fuel cells. *Journal of Power Sources*, 178(1):258–268, 2008.
- [6] P. Cheung, J. D. Fairweather, and D. T. Schwartz. Characterization of internal

- wetting in polymer electrolyte membrane gas diffusion layers. *Journal of Power Sources*, 187(2):487–492, 2009.
- [7] J. D. Fairweather, P. Cheung, and D. T. Schwartz. The effects of wetproofing on the capillary properties of proton exchange membrane fuel cell gas diffusion layers. *Journal of Power Sources*, 195(3):787–793, 2010.
- [8] J. D. Fairweather, P. Cheung, J. St-Pierre, and D. T. Schwartz. A microfluidic approach for measuring capillary pressure in PEMFC gas diffusion layers. *Electrochemistry Communications*, 9(9):2340–2345, 2007.
- [9] J. H. Ferziger and M. Perić. *Computational methods for fluid dynamics*. Springer Berlin, 1999.
- [10] T. J. P. Freire and E. R. Gonzalez. Effect of membrane characteristics and humidification conditions on the impedance response of polymer electrolyte fuel cells. *Journal of Electroanalytical Chemistry*, 503(1-2):57–68, 2001.
- [11] D. Gerteisen, T. Heilmann, and C. Ziegler. Enhancing liquid water transport by laser perforation of a GDL in a PEM fuel cell. *Journal of Power Sources*, 177(2):348–354, 2008.
- [12] L. Giorgi, E. Antolini, A. Pozio, and E. Passalacqua. Influence of the PTFE content in the diffusion layer of low-Pt loading electrodes for polymer electrolyte fuel cells. *Electrochimica Acta*, 43(24):3675–3680, 1998.
- [13] J. T. Gostick, M. W. Fowler, M. A. Ioannidis, M. D. Pritzker, Y. M. Volfkovich, and A. Sakars. Capillary pressure and hydrophilic porosity in gas diffusion layers

- for polymer electrolyte fuel cells. *Journal of Power Sources*, 156(2):375–387, 2006.
- [14] J. T. Gostick, M. A. Ioannidis, M. W. Fowler, and M. D. Pritzker. Pore network modeling of fibrous gas diffusion layers for polymer electrolyte membrane fuel cells. *Journal of Power Sources*, 173(1):277–290, 2007.
- [15] J. T. Gostick, M. A. Ioannidis, M. W. Fowler, and M. D. Pritzker. On the role of the microporous layer in PEMFC operation. *Electrochemistry Communications*, 11(3):576–579, 2009.
- [16] J. T. Gostick, M. A. Ioannidis, M. W. Fowler, and M. D. Pritzker. On the role of the microporous layer in PEMFC operation. *Electrochemistry Communications*, 11(3):576–579, 2009.
- [17] J. T. Gostick, M. A. Ioannidis, Michael W. Fowler, and M. D. Pritzker. Direct measurement of the capillary pressure characteristics of water-air-gas diffusion layer systems for PEM fuel cells. *Electrochemistry Communications*, 10(10):1520–1523, 2008.
- [18] J. T. Gostick, M. A. Ioannidis, Michael W. Fowler, and M. D. Pritzker. Wettability and capillary behavior of fibrous gas diffusion media for polymer electrolyte membrane fuel cells. *Journal of Power Sources*, 194(1):433–444, 2009.
- [19] V. Gurau, M. J. Bluemle, E. S. De Castro, Y. M. Tsou, J. A. Mann., and T. A. Zawodzinski. Characterization of transport properties in gas diffusion layers for proton exchange membrane fuel cells 1. Wettability (internal contact angle to water and surface energy of GDL fibers). *Journal of Power Sources*, 160(2):1156–1162, 2006.

- [20] C. Hartnig, I. Manke, R. Kuhn, S. Kleinau, J. Goebbels, and J. Banhart. High-resolution in-plane investigation of the water evolution and transport in pem fuel cells. *Journal of Power Sources*, 188(2):468–474, 2009.
- [21] G. M. Homsy. Viscous fingering in porous media. *Annual Reviews in Fluid Mechanics*, 19(1):271–311, 1987.
- [22] L. James and D. Andrew. *Fuel Cell Systems Explained*. Chichester, West Sussex, New York: Wiley, 2000.
- [23] E. Kimball, T. Whitaker, Y. G. Kevrekidis, and J. B. Benzinger. Drops, slugs, and flooding in polymer electrolyte membrane fuel cells. *AIChE Journal*, 54(5):1313–1332, 2008.
- [24] P. R. King. The fractal nature of viscous fingering in porous media. *J. Phys. A*, 20:529–534, 1987.
- [25] C. S. Kong, D. Y. Kim, H. K. Lee, Y. G. Shul, and T. H. Lee. Influence of pore-size distribution of diffusion layer on mass-transport problems of proton exchange membrane fuel cells. *Journal of Power Sources*, 108(1-2):185–191, 2002.
- [26] E. C. Kumbur, K. V. Sharp, and M. M. Mench. On the effectiveness of leverett approach for describing the water transport in fuel cell diffusion media. *Journal of Power Sources*, 168(2):356–368, 2007.
- [27] E. C. Kumbur, K. V. Sharp, and M. M. Mench. Validated leverett approach for multiphase flow in pefc diffusion media i. hydrophobicity effect. *Journal of The Electrochemical Society*, 154(12):B1295–B1304, 2007.

-
- [28] E. C. Kumbur, K. V. Sharp, and M. M. Mench. Validated leverett approach for multiphase flow in pefc diffusion media. ii. compression effect. *Journal of The Electrochemical Society*, 154(12):B1305–B1314, 2007.
- [29] E. C. Kumbur, K. V. Sharp, and M. M. Mench. Validated leverett approach for multiphase flow in pefc diffusion media. iii. temperature effect and unified approach. *Journal of The Electrochemical Society*, 154(12):B1315–B1324, 2007.
- [30] S. Kundu, K. Karan, M. Fowler, L. C. Simon, B. Peppley, and E. Halliop. Influence of micro-porous layer and operating conditions on the fluoride release rate and degradation of PEMFC membrane electrode assemblies. *Journal of Power Sources*, 179(2):693–699, 2008.
- [31] Y. H. Lai, Y. Li, and J. A. Rock. A novel full-field experimental method to measure the local compressibility of gas diffusion media. *Journal of Power Sources*, 195(10):3215–3223, 2010.
- [32] L.W. Lake. *Enhanced Oil Recovery*. Old Tappan, NJ; Prentice Hall Inc., 1989.
- [33] K. J. Lee, J. H. Nam, and C. J. Kim. Pore-network analysis of two-phase water transport in gas diffusion layers of polymer electrolyte membrane fuel cells. *Electrochimica Acta*, 54(4):1166–1176, 2009.
- [34] R. Lenormand. Liquids in porous media. *J. Phys. Condens. Matter*, 2:SA79–SA88, 1990.
- [35] R. Lenormand, E. Touboul, and C. Zarccone. Numerical models and experiments on immiscible displacements in porous media. *Journal of Fluid Mechanics*, 189:165–187, 1988.

- [36] M. C. Leverett. Capillary behavior in porous solids. *AIME Trans.*, 142:152–169, 1941.
- [37] H. Li, Y. Tang, Z. Wang, Z. Shi, S. Wu, D. Song, J. Zhang, K. Fatih, J. Zhang, H. Wang, Z. Liu, R. Abouatallah, and A. Mazza. A review of water flooding issues in the proton exchange membrane fuel cell. *Journal of Power Sources*, 178(1):103–117, 2008.
- [38] X. Li and I. Sabir. Review of bipolar plates in PEM fuel cells: Flow-field designs. *International Journal of Hydrogen Energy*, 30(4):359–371, 2005.
- [39] S. Litster, D. Sinton, and N. Djilali. Ex situ visualization of liquid water transport in PEM fuel cell gas diffusion layers. *Journal of Power Sources*, 154(1):95–105, 2006.
- [40] C. H. Liu, T. H. Ko, J. W. Shen, S. Chang, S. Chang, and Y. K. Liao. Effect of hydrophobic gas diffusion layers on the performance of the polymer exchange membrane fuel cell. *Journal of Power Sources*, 191(2):489–494, 2009.
- [41] B. Markicevic, A. Bazylak, and N. Djilali. Determination of transport parameters for multiphase flow in porous gas diffusion electrodes using a capillary network model. *Journal of Power Sources*, 171(2):706–717, 2007.
- [42] E. Medici and J. Allen. The effects of morphological and wetting properties of porous transport layers on water movement in PEM fuel cells. *Journal of The Electrochemical Society*, 157(10):Corrected Proof, 2010.
- [43] E. F. Medici and J. S. Allen. Existence of the phase drainage diagram in proton

-
- exchange membrane fuel cell fibrous diffusion media. *Journal of Power Sources*, 191(2):417–427, 2009.
- [44] EF Medici and JS Allen. Scaling the Water Percolation in PEM Fuel Cell Porous Transport Layers. In *AIP Conference Proceedings*, volume 1254, page 236, 2010.
- [45] S. Middleman. *Modeling axisymmetric flows: dynamics of films, jets, and drops*. Academic Pr, 1995.
- [46] J. H. Nam and M. Kaviany. Effective diffusivity and water-saturation distribution in single- and two-layer PEMFC diffusion medium. *International Journal of Heat and Mass Transfer*, 46(24):4595–4611, 2003.
- [47] T. V. Nguyen. A Gas Distributor Design for Proton-Exchange-Membrane Fuel Cells, journal = *Journal of The Electrochemical Society*. 143(5):L103–L105, 1996.
- [48] J. L. Nieber, T. W. J. Bauters, T. S. Steenhuis, and J. Y. Parlange. Numerical simulation of experimental gravity-driven unstable flow in water repellent sand. *Journal of Hydrology*, 231:295–307, 2000.
- [49] J. P. Owejan, J. E. Owejan, T. W. Tighe, W. Gu, and M. Mathias. Investigation of fundamental transport mechanism of product water from cathode catalyst layer in pemfcs. 2007.
- [50] U. Pasaogullari and C. Y. Wang. Two-phase transport and the role of microporous layer in polymer electrolyte fuel cells. *Electrochimica Acta*, 49(25):4359–4369, 2004.
- [51] S. V. Patankar. *Numerical heat transfer and fluid flow*. Hemisphere Pub, 1980.

- [52] Z. Qi and A. Kaufman. Improvement of water management by a microporous sublayer for PEM fuel cells. *Journal of Power Sources*, 109(1):38–46, 2002.
- [53] R. P. Ramasamy, E. C. Kumbur, M. M. Mench, W. Liu, D. Moore, and M. Murthy. Investigation of macro- and micro-porous layer interaction in polymer electrolyte fuel cells. *International Journal of Hydrogen Energy*, 33(13):3351–3367, 2008.
- [54] R. Satija, D. L. Jacobson, M. Arif, and S. A. Werner. In situ neutron imaging technique for evaluation of water management systems in operating PEM fuel cells. *Journal of Power Sources*, 129(2):238–245, 2004.
- [55] P. K. Sinha, P. P. Mukherjee, and C. Y. Wang. Impact of GDL structure and wettability on water management in polymer electrolyte fuel cells. *Journal of Materials Chemistry*, 17(30):3089–3103, 2007.
- [56] P. K. Sinha and C. Y. Wang. Pore-network modeling of liquid water transport in gas diffusion layer of a polymer electrolyte fuel cell. *Electrochimica Acta*, 52(28):7936–7945, 2007.
- [57] A. Stephanou, S. R. McDougall, A. R. A. Anderson, M. A. J. Chaplain, and J. A. Sherratt. Mathematical modelling of flow in 2D and 3D vascular networks: Applications to anti-angiogenic and chemotherapeutic drug strategies. *Mathematical and Computer Modelling*, 41(10):1137–1156, 2005.
- [58] Y. Tabe, Y. Lee, T. Chikahisa, and M. Kozakai. Numerical simulation of liquid water and gas flow in a channel and a simplified gas diffusion layer model of polymer electrolyte membrane fuel cells using the lattice Boltzmann method. *Journal of Power Sources*, 193(1):24–31, 2009.

- [59] R. Thiedmann, C. Hartnig, I. Manke, V. Schmidt, and W. Lehnert. Local Structural Characteristics of Pore Space in GDLs of PEM Fuel Cells Based on Geometric 3D Graphs. *Journal of The Electrochemical Society*, 156(11):B1339–B1347, 2009.
- [60] S. Tsushima, K. Teranishi, K. Nishida, and S. Hirai. Water content distribution in a polymer electrolyte membrane for advanced fuel cell system with liquid water supply. *Magnetic Resonance Imaging*, 23(2):255–258, 2005.
- [61] H. J. Vogel, J. Tolke, V. P. Schulz, M. Krafczyk, and K. Roth. Comparison of a Lattice-Boltzmann model, a full-morphology model, and a pore network model for determining capillary pressure-saturation relationships. *Vadose Zone Journal*, 4(2):380–388, 2005.
- [62] A. Z. Weber, R. Balliet, H. P. Gunterman, and J. Newman. *Modeling Water Management in Polymer-Electrolyte Fuel Cells*. Number 43. 2009.
- [63] A. Z. Weber and J. Newman. Effects of Microporous Layers in Polymer Electrolyte Fuel Cells. *Journal of The Electrochemical Society*, 152(4):A677–A688, 2005.
- [64] M. V. Williams, E. Begg, L. Bonville, H. R. Kunz, and J. M. Fenton. Characterization of Gas Diffusion Layers for PEMFC. *Journal of The Electrochemical Society*, 151(8):A1173–A1180, 2004.
- [65] M. S. Yazici. Mass transfer layer for liquid fuel cells. *Journal of Power Sources*, 166(2):424–429, 2007.

APPENDICES

A. NUMERICAL MODEL

1.1 Discretization

The equation (4.1) presented in chapter IV has to be solved at each node. The pore structure is modeled as regular grid where four pores concur at each node and the length of the pore is fixed. The pressure at each node will depend of on the pressure action on the neighbor nodes. Therefore, the pressure at each node has to be solved simultaneously.

The using the Kirchoff analogy the system of equations at every pore can be written in term of the pressure gradient as described in Chapter IV:

$$\frac{\pi}{8l} \sum_{j=1}^4 \frac{r_{ij}^4}{\mu_{ij}^e} (\Delta p_{ij} - p_{ij}^c) = 0 \quad (1.1)$$

enclosing the properties at a pore level into one variable $g_{ij} = \pi r_{ij}^4 / 8l \mu_{ij}^e$

$$\sum_{j=1}^4 g_{ij} (\Delta p_{ij} - p_{ij}^c) = 0 \quad (1.2)$$

which can be rewriting as:

$$\sum_{j=1}^4 g_{ij} \Delta p_{ij} = \sum_{j=1}^4 g_{ij} p_{ij}^c \quad (1.3)$$

which can also be written in a matrix manner as:

$$AX = B \tag{1.4}$$

where $A_{ij} = g_{ij}$, $X_j = \Delta p_{ij}$, and $B_j = g_{ij} p_{ij}^c$

The resulting linear system of equations was solved numerically using the conjugated gradient method taking advantage of the symmetry of the problem (A is five diagonal matrix) as described by [9]. In order to obtain the numerical solution a Fortran code was developed. Every diagonal in the matrix A correspond to: the central diagonal corresponds to the properties of particular node ‘i’, while the other four diagonals correspond to the properties of the four node surrounding node ‘i’. The nodes surrounding node ‘i’ where identifies by following the nomenclature use by [51] as east, west, north and south.

1.2 Source Term

The network model has been originally developed to study unsaturated flow in porous media [35]. In many applications, the flow in porous media is treated like a constant pressure flow rate. Therefore, the source term in the network model which is in the form of flow rate has to be modified in order to include the pressure gradient. However, in the case of water percolating through a PTL in a PEM fuel cell, the water is generated continuously and it can be assumed as a constant flow rate behavior. This assumption simplifies the modeling. First, the flow is assigned at the injection nodes

in the form of:

$$\sum_{j=1}^4 q_j = q_s \quad (1.5)$$

where q_s is the source flow rate at the node given node. Then, the pressure gradient is calculated as it was explained in Chapter 4. To calculate the fluid position inside each the pore at the injected-displaced fluid interface, the total injected volume of fluid $Q\Delta t$ is distributed along the pore at the interface proportional to the pressure gradient where the condition $\Delta P > P_c$ is satisfied:

$$v_{ij}^{\text{pore}} = \frac{\Delta P_{ij}}{\sum_{k=1}^n \Delta P_{ij}^k} Q\Delta t \quad (1.6)$$

where v_{ij}^{pore} is the volume of a given pore between the nodes 'i' and 'j', ΔP_{ij} is the pressure drop at a given pore between the nodes 'i' and 'j', and $\sum_{k=1}^n \Delta P_{ij}^k$ is the integrated pressure drop at the interface where the condition $\Delta P_{ij} > P_c$ is satisfied. Then, the new fluid position, x_{ij} at a given pore, is calculated by dividing by the pore cross sectional area, A_{ij}^{pore} :

$$x_{ij} = \frac{v_{ij}^{\text{pore}}}{A_{ij}^{\text{pore}}} + x_0 \quad (1.7)$$

where x_0 is the previous fluid position inside the pore. This approach is valid for small time steps where the volume of injected fluid is smaller than the volume to full fill the pore in only one time step. Normally, it will take few time steps to full fill a pore. The time step is determined based on the injection flow rate. A fixed small time will consume unnecessary computing resources in cases of high flow rates. Eventually,

when he calculated x_i is larger than the pore length ' l ', the surplus volume of injected fluid after filling the pore is evenly divided among the available surrounding pores. At the most common scenario, the number of available surrounding pores are three. However, it can be cases where only one or two pores are available for fluid percolation due to previous pore full filling.

B. COPYRIGHT AGREEMENTS

2.1 Copyright agreements with Elsevier

Terms and conditions from Elsevier to reprint on Chapter II the full content of the article: E. F. Médiçi and J. S. Allen, Existence of the phase drainage diagram in proton exchange membrane fuel cell fibrous diffusion media, 191/2, 417-427, 2009.

Rightslink Printable License

<https://s100.copyright.com/App/PrintableLicenseFrame.jsp?publisherID...>

ELSEVIER LICENSE TERMS AND CONDITIONS

Jul 20, 2010

This is a License Agreement between Ezequiel F Medici ("You") and Elsevier ("Elsevier") provided by Copyright Clearance Center ("CCC"). The license consists of your order details, the terms and conditions provided by Elsevier, and the payment terms and conditions.

All payments must be made in full to CCC. For payment instructions, please see information listed at the bottom of this form.

Supplier	Elsevier Limited The Boulevard, Langford Lane Kidlington, Oxford, OX5 1GB, UK
Registered Company Number	1982084
Customer name	Ezequiel F Medici
Customer address	408D R. L. Smith Building Houghton, MI 49931
License number	2473121155120
License date	Jul 20, 2010
Licensed content publisher	Elsevier
Licensed content publication	Journal of Power Sources
Licensed content title	Existence of the phase drainage diagram in proton exchange membrane fuel cell fibrous diffusion media
Licensed content author	E.F. Medici, J.S. Allen
Licensed content date	15 June 2009
Licensed content volume number	191
Licensed content issue number	2
Number of pages	11
Type of Use	reuse in a thesis/dissertation
Requestor type	Not specified
Intended publisher of new work	other
Portion	full article
Format	both print and electronic
Yes	
No	
Order reference number	
Title of your thesis/dissertation	Water Transport in Complex, Non-Wetting Porous Layers with Applications to Water Management in Low Temperature Fuel cells
Expected completion date	Aug 2010
Estimated size (number of pages)	200
Elsevier VAT number	GB 494 6272 12
Terms and Conditions	

INTRODUCTION

1. The publisher for this copyrighted material is Elsevier. By clicking "accept" in connection with completing this licensing transaction, you agree that the following terms and conditions apply to this transaction (along with the Billing and Payment terms and conditions established by Copyright Clearance Center, Inc. ("CCC"), at the time that you opened your Rightslink account and that are available at any time at <http://myaccount.copyright.com>).

GENERAL TERMS

2. Elsevier hereby grants you permission to reproduce the aforementioned material subject to the terms and conditions indicated.

3. Acknowledgement: If any part of the material to be used (for example, figures) has appeared in our publication with credit or acknowledgement to another source, permission must also be sought from that source. If such permission is not obtained then that material may not be included in your publication/copies. Suitable acknowledgement to the source must be made, either as a footnote or in a reference list at the end of your publication, as follows:

“Reprinted from Publication title, Vol /edition number, Author(s), Title of article / title of chapter, Pages No., Copyright (Year), with permission from Elsevier [OR APPLICABLE SOCIETY COPYRIGHT OWNER].” Also Lancet special credit - “Reprinted from The Lancet, Vol. number, Author(s), Title of article, Pages No., Copyright (Year), with permission from Elsevier.”

4. Reproduction of this material is confined to the purpose and/or media for which permission is hereby given.

5. Altering/Modifying Material: Not Permitted. However figures and illustrations may be altered/adapted minimally to serve your work. Any other abbreviations, additions, deletions and/or any other alterations shall be made only with prior written authorization of Elsevier Ltd. (Please contact Elsevier at permissions@elsevier.com)

6. If the permission fee for the requested use of our material is waived in this instance, please be advised that your future requests for Elsevier materials may attract a fee.

7. Reservation of Rights: Publisher reserves all rights not specifically granted in the combination of (i) the license details provided by you and accepted in the course of this licensing transaction, (ii) these terms and conditions and (iii) CCC's Billing and Payment terms and conditions.

8. License Contingent Upon Payment: While you may exercise the rights licensed immediately upon issuance of the license at the end of the licensing process for the transaction, provided that you have disclosed complete and accurate details of your proposed use, no license is finally effective unless and until full payment is received from you (either by publisher or by CCC) as provided in CCC's Billing and Payment terms and conditions. If full payment is not received on a timely basis, then any license preliminarily granted shall be deemed automatically revoked and shall be void as if never granted. Further, in the event that you breach any of these terms and conditions or any of CCC's Billing and Payment terms and conditions, the license is automatically revoked and shall be void as if never granted. Use of materials as described in a revoked license, as well as any use of the materials beyond the scope of an unrevoked license, may constitute copyright infringement and publisher reserves the right to take any and all action to protect its copyright in the materials.

9. Warranties: Publisher makes no representations or warranties with respect to the licensed material.

10. Indemnity: You hereby indemnify and agree to hold harmless publisher and CCC, and their respective officers, directors, employees and agents, from and against any and all claims arising out of your use of the licensed material other than as specifically authorized pursuant to this license.

11. No Transfer of License: This license is personal to you and may not be sublicensed, assigned, or transferred by you to any other person without publisher's written permission.

12. No Amendment Except in Writing: This license may not be amended except in a writing signed by both parties (or, in the case of publisher, by CCC on publisher's behalf).

13. Objection to Contrary Terms: Publisher hereby objects to any terms contained in any purchase order, acknowledgment, check endorsement or other writing prepared by you,

which terms are inconsistent with these terms and conditions or CCC's Billing and Payment terms and conditions. These terms and conditions, together with CCC's Billing and Payment terms and conditions (which are incorporated herein), comprise the entire agreement between you and publisher (and CCC) concerning this licensing transaction. In the event of any conflict between your obligations established by these terms and conditions and those established by CCC's Billing and Payment terms and conditions, these terms and conditions shall control.

14. **Revocation:** Elsevier or Copyright Clearance Center may deny the permissions described in this License at their sole discretion, for any reason or no reason, with a full refund payable to you. Notice of such denial will be made using the contact information provided by you. Failure to receive such notice will not alter or invalidate the denial. In no event will Elsevier or Copyright Clearance Center be responsible or liable for any costs, expenses or damage incurred by you as a result of a denial of your permission request, other than a refund of the amount(s) paid by you to Elsevier and/or Copyright Clearance Center for denied permissions.

LIMITED LICENSE

The following terms and conditions apply only to specific license types:

15. **Translation:** This permission is granted for non-exclusive world **English** rights only unless your license was granted for translation rights. If you licensed translation rights you may only translate this content into the languages you requested. A professional translator must perform all translations and reproduce the content word for word preserving the integrity of the article. If this license is to re-use 1 or 2 figures then permission is granted for non-exclusive world rights in all languages.

16. **Website:** The following terms and conditions apply to electronic reserve and author websites:

Electronic reserve: If licensed material is to be posted to website, the web site is to be password-protected and made available only to bona fide students registered on a relevant course if:

This license was made in connection with a course,

This permission is granted for 1 year only. You may obtain a license for future website posting.

All content posted to the web site must maintain the copyright information line on the bottom of each image,

A hyper-text must be included to the Homepage of the journal from which you are licensing at <http://www.sciencedirect.com/science/journal/xxxxx> or the Elsevier homepage for books at <http://www.elsevier.com> , and

Central Storage: This license does not include permission for a scanned version of the material to be stored in a central repository such as that provided by Heron/XanEdu.

17. **Author website** for journals with the following additional clauses:

All content posted to the web site must maintain the copyright information line on the bottom of each image, and

the permission granted is limited to the personal version of your paper. You are not allowed to download and post the published electronic version of your article (whether PDF or HTML, proof or final version), nor may you scan the printed edition to create an electronic version,

A hyper-text must be included to the Homepage of the journal from which you are licensing at <http://www.sciencedirect.com/science/journal/xxxxx> , As part of our normal production process, you will receive an e-mail notice when your article appears on Elsevier's online service ScienceDirect (www.sciencedirect.com). That e-mail will include the article's Digital Object Identifier (DOI). This number provides the electronic link to the published article and should be included in the posting of your personal version. We ask that you wait until you receive this e-mail and have the DOI to do any posting.

Central Storage: This license does not include permission for a scanned version of the material to be stored in a central repository such as that provided by Heron/XanEdu.

18. **Author website** for books with the following additional clauses:

Authors are permitted to place a brief summary of their work online only.

A hyper-text must be included to the Elsevier homepage at <http://www.elsevier.com>

All content posted to the web site must maintain the copyright information line on the bottom of each image

You are not allowed to download and post the published electronic version of your chapter, nor may you scan the printed edition to create an electronic version.

Central Storage: This license does not include permission for a scanned version of the material to be stored in a central repository such as that provided by Heron/XanEdu.

19. **Website** (regular and for author): A hyper-text must be included to the Homepage of the journal from which you are licensing at <http://www.sciencedirect.com/science/journal/xxxxx>, or for books to the Elsevier homepage at <http://www.elsevier.com>

20. **Thesis/Dissertation**: If your license is for use in a thesis/dissertation your thesis may be submitted to your institution in either print or electronic form. Should your thesis be published commercially, please reapply for permission. These requirements include permission for the Library and Archives of Canada to supply single copies, on demand, of the complete thesis and include permission for UMI to supply single copies, on demand, of the complete thesis. Should your thesis be published commercially, please reapply for permission.

21. **Other Conditions**:

v1.6

Gratis licenses (referencing \$0 in the Total field) are free. Please retain this printable license for your reference. No payment is required.

If you would like to pay for this license now, please remit this license along with your payment made payable to "COPYRIGHT CLEARANCE CENTER" otherwise you will be invoiced within 48 hours of the license date. Payment should be in the form of a check or money order referencing your account number and this invoice number RLNK10818031.

Once you receive your invoice for this order, you may pay your invoice by credit card. Please follow instructions provided at that time.

**Make Payment To:
Copyright Clearance Center
Dept 001
P.O. Box 843006
Boston, MA 02284-3006**

If you find copyrighted material related to this license will not be used and wish to cancel, please contact us referencing this license number 2473121155120 and noting the reason for cancellation.

Questions? customer@copyright.com or +1-877-622-5543 (toll free in the US) or +1-978-646-2777.

2.2 Copyright agreements with the American Institute of Physics

Terms and conditions from American Institute of Physics to reprint on Chapter III the abstract of the article: E. Médici and J. S. Allen, Scaling the Water Percolation in PEM Fuel Cell Porous Transport Layers, Proceedings of the Third International Conference on Porous Media and its Applications in Science, Engineering and Industry, June 2010, Montecatini, Italy.

Rightslink Printable License

<https://s100.copyright.com/App/PrintableLicenseFrame.jsp?publisherID...>

AMERICAN INSTITUTE OF PHYSICS LICENSE TERMS AND CONDITIONS

Jul 20, 2010

This is a License Agreement between Ezequiel F Medici ("You") and American Institute of Physics ("AIP") provided by Copyright Clearance Center ("CCC"). The license consists of your order details, the terms and conditions provided by American Institute of Physics, and the payment terms and conditions.

All payments must be made in full to CCC. For payment instructions, please see information listed at the bottom of this form.

License Number	2473130017136
License date	Jul 20, 2010
Licensed content publisher	American Institute of Physics
Licensed content publication	AIP Conference Proceedings
Licensed content title	Scaling the Water Percolation in PEM Fuel Cell Porous Transport Layers
Licensed content author	E. F. Medici, J. S. Allen
Licensed content date	May 30, 2010
Volume number	1254
Issue number	1
Type of Use	Thesis/Dissertation
Requestor type	Author (original article)
Format	Print and electronic
Portion	Abstract
Will you be translating?	No
Title of your thesis / dissertation	Water Transport in Complex, Non-Wetting Porous Layers with Applications to Water Management in Low Temperature Fuel cells
Expected completion date	Aug 2010
Estimated size (number of pages)	200
Total	0.00 USD

Terms and Conditions

American Institute of Physics -- Terms and Conditions: Permissions Uses

American Institute of Physics ("AIP") hereby grants to you the non-exclusive right and license to use and/or distribute the Material according to the use specified in your order, on a one-time basis, for the specified term, with a maximum distribution equal to the number that you have ordered. Any links or other content accompanying the Material are not the subject of this license.

1. You agree to include the following copyright and permission notice with the reproduction of the Material: "Reprinted with permission from [FULL CITATION]. Copyright [PUBLICATION YEAR], American Institute of Physics." For an article, the copyright and permission notice must be printed on the first page of the article or book chapter. For photographs, covers, or tables, the copyright and permission notice may appear with the Material, in a footnote, or in the reference list.
2. If you have licensed reuse of a figure, photograph, cover, or table, it is your responsibility to ensure that the material is original to AIP and does not contain the copyright of another entity, and that the copyright notice of the figure, photograph, cover, or table does not indicate that it was reprinted by AIP, with permission, from another source. Under no circumstances does AIP, purport or intend to grant permission to reuse material to which it does not hold copyright.
3. You may not alter or modify the Material in any manner. You may translate the Material into another language only if you have licensed translation rights. You may not use the Material for promotional purposes. AIP reserves all rights not specifically granted herein.
4. The foregoing license shall not take effect unless and until AIP or its agent, Copyright Clearance Center, receives the Payment in accordance with Copyright Clearance Center Billing and Payment Terms and Conditions, which are incorporated herein by

reference.

5. AIP or the Copyright Clearance Center may, within two business days of granting this license, revoke the license for any reason whatsoever, with a full refund payable to you. Should you violate the terms of this license at any time, AIP, American Institute of Physics, or Copyright Clearance Center may revoke the license with no refund to you. Notice of such revocation will be made using the contact information provided by you. Failure to receive such notice will not nullify the revocation.
6. AIP makes no representations or warranties with respect to the Material. You agree to indemnify and hold harmless AIP, American Institute of Physics, and their officers, directors, employees or agents from and against any and all claims arising out of your use of the Material other than as specifically authorized herein.
7. The permission granted herein is personal to you and is not transferable or assignable without the prior written permission of AIP. This license may not be amended except in a writing signed by the party to be charged.
8. If purchase orders, acknowledgments or check endorsements are issued on any forms containing terms and conditions which are inconsistent with these provisions, such inconsistent terms and conditions shall be of no force and effect. This document, including the CCC Billing and Payment Terms and Conditions, shall be the entire agreement between the parties relating to the subject matter hereof.

This Agreement shall be governed by and construed in accordance with the laws of the State of New York. Both parties hereby submit to the jurisdiction of the courts of New York County for purposes of resolving any disputes that may arise hereunder.

Gratis licenses (referencing \$0 in the Total field) are free. Please retain this printable license for your reference. No payment is required.

If you would like to pay for this license now, please remit this license along with your payment made payable to "COPYRIGHT CLEARANCE CENTER" otherwise you will be invoiced within 48 hours of the license date. Payment should be in the form of a check or money order referencing your account number and this invoice number RLNK10818045.

Once you receive your invoice for this order, you may pay your invoice by credit card. Please follow instructions provided at that time.

**Make Payment To:
Copyright Clearance Center
Dept 001
P.O. Box 843006
Boston, MA 02284-3006**

If you find copyrighted material related to this license will not be used and wish to cancel, please contact us referencing this license number 2473130017136 and noting the reason for cancellation.

Questions? customer@copyright.com or +1-877-622-5543 (toll free in the US) or +1-978-646-2777.

Terms and conditions from American Institute of Physics to reprint on Chapter III the text content of the article: E. Médici and J. S. Allen, Scaling the Water Percolation in PEM Fuel Cell Porous Transport Layers, Proceedings of the Third International Conference on Porous Media and its Applications in Science, Engineering and Industry, June 2010, Montecatini, Italy.

Rightslink Printable License

<https://s100.copyright.com/App/PrintableLicenseFrame.jsp?publisherID...>

**AMERICAN INSTITUTE OF PHYSICS LICENSE
TERMS AND CONDITIONS**

Jul 20, 2010

This is a License Agreement between Ezequiel F Medici ("You") and American Institute of Physics ("AIP") provided by Copyright Clearance Center ("CCC"). The license consists of your order details, the terms and conditions provided by American Institute of Physics, and the payment terms and conditions.

All payments must be made in full to CCC. For payment instructions, please see information listed at the bottom of this form.

License Number	2473120957542
License date	Jul 20, 2010
Licensed content publisher	American Institute of Physics
Licensed content publication	AIP Conference Proceedings
Licensed content title	Scaling the Water Percolation in PEM Fuel Cell Porous Transport Layers
Licensed content author	E. F. Medici, J. S. Allen
Licensed content date	May 30, 2010
Volume number	1254
Issue number	1
Type of Use	Thesis/Dissertation
Requestor type	Author (original article)
Format	Print and electronic
Portion	Excerpt (> 800 words)
Will you be translating?	No
Title of your thesis / dissertation	Water Transport in Complex, Non-Wetting Porous Layers with Applications to Water Management in Low Temperature Fuel cells
Expected completion date	Aug 2010
Estimated size (number of pages)	200
Total	0.00 USD
Terms and Conditions	

American Institute of Physics -- Terms and Conditions: Permissions Uses

American Institute of Physics ("AIP") hereby grants to you the non-exclusive right and license to use and/or distribute the Material according to the use specified in your order, on a one-time basis, for the specified term, with a maximum distribution equal to the number that you have ordered. Any links or other content accompanying the Material are not the subject of this license.

1. You agree to include the following copyright and permission notice with the reproduction of the Material: "Reprinted with permission from [FULL CITATION]. Copyright [PUBLICATION YEAR], American Institute of Physics." For an article, the copyright and permission notice must be printed on the first page of the article or book chapter. For photographs, covers, or tables, the copyright and permission notice may appear with the Material, in a footnote, or in the reference list.
2. If you have licensed reuse of a figure, photograph, cover, or table, it is your responsibility to ensure that the material is original to AIP and does not contain the copyright of another entity, and that the copyright notice of the figure, photograph, cover, or table does not indicate that it was reprinted by AIP, with permission, from another source. Under no circumstances does AIP purport or intend to grant permission to reuse material to which it does not hold copyright.
3. You may not alter or modify the Material in any manner. You may translate the Material into another language only if you have licensed translation rights. You may not use the Material for promotional purposes. AIP reserves all rights not specifically granted herein.
4. The foregoing license shall not take effect unless and until AIP or its agent, Copyright Clearance Center, receives the Payment in accordance with Copyright Clearance Center Billing and Payment Terms and Conditions, which are incorporated herein by

reference.

5. AIP or the Copyright Clearance Center may, within two business days of granting this license, revoke the license for any reason whatsoever, with a full refund payable to you. Should you violate the terms of this license at any time, AIP, American Institute of Physics, or Copyright Clearance Center may revoke the license with no refund to you. Notice of such revocation will be made using the contact information provided by you. Failure to receive such notice will not nullify the revocation.
6. AIP makes no representations or warranties with respect to the Material. You agree to indemnify and hold harmless AIP, American Institute of Physics, and their officers, directors, employees or agents from and against any and all claims arising out of your use of the Material other than as specifically authorized herein.
7. The permission granted herein is personal to you and is not transferable or assignable without the prior written permission of AIP. This license may not be amended except in a writing signed by the party to be charged.
8. If purchase orders, acknowledgments or check endorsements are issued on any forms containing terms and conditions which are inconsistent with these provisions, such inconsistent terms and conditions shall be of no force and effect. This document, including the CCC Billing and Payment Terms and Conditions, shall be the entire agreement between the parties relating to the subject matter hereof.

This Agreement shall be governed by and construed in accordance with the laws of the State of New York. Both parties hereby submit to the jurisdiction of the courts of New York County for purposes of resolving any disputes that may arise hereunder.

Gratis licenses (referencing \$0 in the Total field) are free. Please retain this printable license for your reference. No payment is required.

If you would like to pay for this license now, please remit this license along with your payment made payable to "COPYRIGHT CLEARANCE CENTER" otherwise you will be invoiced within 48 hours of the license date. Payment should be in the form of a check or money order referencing your account number and this invoice number RLNK10818019.

Once you receive your invoice for this order, you may pay your invoice by credit card. Please follow instructions provided at that time.

**Make Payment To:
Copyright Clearance Center
Dept 001
P.O. Box 843006
Boston, MA 02284-3006**

If you find copyrighted material related to this license will not be used and wish to cancel, please contact us referencing this license number 2473120957542 and noting the reason for cancellation.

Questions? customer@copyright.com or +1-877-622-5543 (toll free in the US) or +1-978-646-2777.

Terms and conditions from American Institute of Physics to reprint on Chapter III the figures and tables of the article: E. Médici and J. S. Allen, Scaling the Water Percolation in PEM Fuel Cell Porous Transport Layers, Proceedings of the Third International Conference on Porous Media and its Applications in Science, Engineering and Industry, June 2010, Montecatini, Italy.

Rightslink Printable License

<https://s100.copyright.com/App/PrintableLicenseFrame.jsp?publisherID...>

**AMERICAN INSTITUTE OF PHYSICS LICENSE
TERMS AND CONDITIONS**

Jul 20, 2010

This is a License Agreement between Ezequiel F Medici ("You") and American Institute of Physics ("AIP") provided by Copyright Clearance Center ("CCC"). The license consists of your order details, the terms and conditions provided by American Institute of Physics, and the payment terms and conditions.

All payments must be made in full to CCC. For payment instructions, please see information listed at the bottom of this form.

License Number	2473121420557
License date	Jul 20, 2010
Licensed content publisher	American Institute of Physics
Licensed content publication	AIP Conference Proceedings
Licensed content title	Scaling the Water Percolation in PEM Fuel Cell Porous Transport Layers
Licensed content author	E. F. Medici, J. S. Allen
Licensed content date	May 30, 2010
Volume number	1254
Issue number	1
Type of Use	Thesis/Dissertation
Requestor type	Author (original article)
Format	Print and electronic
Portion	Figure/Table
Number of figures/tables	8
Title of your thesis / dissertation	Water Transport in Complex, Non-Wetting Porous Layers with Applications to Water Management in Low Temperature Fuel cells
Expected completion date	Aug 2010
Estimated size (number of pages)	200
Total	0.00 USD

[Terms and Conditions](#)

American Institute of Physics -- Terms and Conditions: Permissions Uses

American Institute of Physics ("AIP") hereby grants to you the non-exclusive right and license to use and/or distribute the Material according to the use specified in your order, on a one-time basis, for the specified term, with a maximum distribution equal to the number that you have ordered. Any links or other content accompanying the Material are not the subject of this license.

1. You agree to include the following copyright and permission notice with the reproduction of the Material: "Reprinted with permission from [FULL CITATION]. Copyright [PUBLICATION YEAR], American Institute of Physics." For an article, the copyright and permission notice must be printed on the first page of the article or book chapter. For photographs, covers, or tables, the copyright and permission notice may appear with the Material, in a footnote, or in the reference list.
2. If you have licensed reuse of a figure, photograph, cover, or table, it is your responsibility to ensure that the material is original to AIP and does not contain the copyright of another entity, and that the copyright notice of the figure, photograph, cover, or table does not indicate that it was reprinted by AIP, with permission, from another source. Under no circumstances does AIP purport or intend to grant permission to reuse material to which it does not hold copyright.
3. You may not alter or modify the Material in any manner. You may translate the Material into another language only if you have licensed translation rights. You may not use the Material for promotional purposes. AIP reserves all rights not specifically granted herein.
4. The foregoing license shall not take effect unless and until AIP or its agent, Copyright Clearance Center, receives the Payment in accordance with Copyright Clearance Center Billing and Payment Terms and Conditions, which are incorporated herein by

reference.

5. AIP or the Copyright Clearance Center may, within two business days of granting this license, revoke the license for any reason whatsoever, with a full refund payable to you. Should you violate the terms of this license at any time, AIP, American Institute of Physics, or Copyright Clearance Center may revoke the license with no refund to you. Notice of such revocation will be made using the contact information provided by you. Failure to receive such notice will not nullify the revocation.
6. AIP makes no representations or warranties with respect to the Material. You agree to indemnify and hold harmless AIP, American Institute of Physics, and their officers, directors, employees or agents from and against any and all claims arising out of your use of the Material other than as specifically authorized herein.
7. The permission granted herein is personal to you and is not transferable or assignable without the prior written permission of AIP. This license may not be amended except in a writing signed by the party to be charged.
8. If purchase orders, acknowledgments or check endorsements are issued on any forms containing terms and conditions which are inconsistent with these provisions, such inconsistent terms and conditions shall be of no force and effect. This document, including the CCC Billing and Payment Terms and Conditions, shall be the entire agreement between the parties relating to the subject matter hereof.

This Agreement shall be governed by and construed in accordance with the laws of the State of New York. Both parties hereby submit to the jurisdiction of the courts of New York County for purposes of resolving any disputes that may arise hereunder.

Gratis licenses (referencing \$0 in the Total field) are free. Please retain this printable license for your reference. No payment is required.

If you would like to pay for this license now, please remit this license along with your payment made payable to "COPYRIGHT CLEARANCE CENTER" otherwise you will be invoiced within 48 hours of the license date. Payment should be in the form of a check or money order referencing your account number and this invoice number RLNK10818039.

Once you receive your invoice for this order, you may pay your invoice by credit card. Please follow instructions provided at that time.

**Make Payment To:
Copyright Clearance Center
Dept 001
P.O. Box 843006
Boston, MA 02284-3006**

If you find copyrighted material related to this license will not be used and wish to cancel, please contact us referencing this license number 2473121420557 and noting the reason for cancellation.

Questions? customer@copyright.com or +1-877-622-5543 (toll free in the US) or +1-978-646-2777.

2.3 Copyright agreements with the Electrochemical Society

Terms and conditions from Electrochemical Society to reprint on Chapter IV the full content of the article: E. Medici and J. S. Allen, The effects of morphological and wetting properties of porous transport layers on water movement in PEM fuel cells, Journal of Electrochemical Society, 157/10, 2010.

Request for Permission to Reproduce or Re-Publish ECS Material

Please fax this form to: The Electrochemical Society (ECS), Attn: Permissions Requests, 1.609.737.2743. You may also e-mail your request to: copyright@electrochem.org. Include all the information as required on this form. Please allow 3-7 days for your request to be processed.

I am preparing a (choose one): paper chapter book thesis
Water Transport in Complex, Non-Wetting Porous Layers with
entitled: Applications to Water Management in Low Temperature Fuel cells
to be published by: Michigan Technological University

in an upcoming publication entitled: _____

I request permission to use the following material in the publication noted above, and request nonexclusive rights for all subsequent editions and in all foreign language translations for distribution throughout the world.

Description of material to be used—Indicate what material you wish to use (figures, tables, text, etc.) and give the full bibliographic reference for the source publication. You may attach a separate list, organized by ECS title.

E. Medici and J. S. Allen, Study of Wettability and Morphological
Properties Effects on Water Percolation in Gas Diffusion Layers of
PEMFC, accepted for publication at the J. of The Electrochemical
Society, manuscript JES-10-0639R (059010JES) expected to be
published in the Volume 157, Number 10.

Signature:  Date: 07/26/2010

Name: Ezequiel Medici

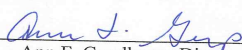
Address: Michigan Technological University, Dept. of Mechanical Engineering
and Engineering Mechanics, 408D R. L. Smith Building,
1400 Townsend Drive, Houghton, Michigan 49931

Telephone: 906-487-4332 Fax: 906-487-2822

E-mail: efmedici@mtu.edu

Permission is granted to include the above-referenced paper in your thesis, provided that you obtain permission of the other individual authors. In the thesis, please acknowledge the authors and the citation given above, and include the words: "Reproduced by permission of ECS — The Electrochemical Society."

July 29, 2010
Date


Ann F. Goedkoop, Director of Publications